Proceedings of

International Conference of Young Scientists

Problems of Physics and Astronomy

25 May 2018,

Baku, Azerbaijan

Baku State University

Organizers:

- The Ministry of Education of the Azerbaijan Republic
- Baku State University
- STAR-NET Regional Network for Education and Training in Nuclear Technology (Austria)•

Sponsor:

- Baku State University

Conference Site: http://physics.bsu.edu.az/az/content/fzka_v__astronomya__problemlr_

Publisher: © Baku University Publishing House, Baku, 2017

Contacts: Z.Khalilov str. 23, Az1148, Baku, Azerbaijan

Web: http://publish.bsu.edu.az/en

Tel: +994 12 539 05 35

TABLE OF CONTENTS

PARAMETRIC INTERACTION OF COUNTER WAVES AT HIGH AND LOW-FREQUENCY PUMPING

[1]SH.A. SHAMILOVA,[1] R. J. KASUMOVA
[1]*Baku State University, Baku,Azerbaijan*
Shahla_shamilova@mail.ru

Abstract. In this paper, taking into account the phase effects, the parametric interaction of waves with low-frequency and high-frequency pumping in a quadratic medium, which is the "left-handed" for the signal wave, is compared. The parameters of the efficiency of the frequency conversion of a signal wave in a nonlinear medium and the amplification factor of a signal wave are considered.

Key words: *Negative refractive index, parametric interaction, constant-intensity approximation*

1. Introduction

The growth interest to the processes of parametric interaction of optical waves is due to the successes achieved in recent years in the development and creation of media with a negative refractive index (NIM-negative index metamaterials) in the microwave and optical frequency bands [1,2] of electromagnetic radiation. The creation of a resonator-free parametric light generator, amplifiers and generators of the optical and microwave ranges of electromagnetic radiation, gives the perspective, in a practical way, to use the phenomenon of parametric interaction. The next stage was the use of the latest advances in nanoplasmonics, namely the results of an investigation of the electromagnetic field around localized plasmons. The injection of plasmon metals, near the resonances of which the nonlinearity increases sharply, into the dielectric structure, leads to a significant concentration of the electromagnetic field around the plasmon nanoparticles. The ability of plasmon nanoparticles to accumulate large electric fields around them allowed the authors [3] to report on overcoming large losses in corresponding structures.

One of the attractive characteristic of these materials is the possibility of providing both a positive and negative value of the real part of the refractive index of a nonlinear medium (i.e. simultaneously negative values of the dielectric permittivity and magnetic of permeability) but for different frequency ranges within the same structure. Due to the frequency dispersion in the left nonlinear medium, a backward wave arises. This creates conditions for the interaction of counter waves. In this sense, the metamaterial provides distributed feedback. Hence it can be said that the metamaterial provides a positive feedback, which is distributed throughout the length of the metamaterial and is manifested through the parametric interaction of waves.

The study of phase effects in three-wave parametric interaction in metamaterials is the goal of this paper. Namely, in the work with allowance for the phase effects, the parametric interaction of the waves is compared for low-frequency (LF) [4] and high-frequency pumping (HF) [5] in a quadratic medium. The parameters of the efficiency of the frequency conversion of a signal wave in a nonlinear medium and the amplification factor of a signal wave are considered. The values of the total length of the metamaterial are calculated at which a significant amplification of the signal wave, leading to the parametric generation of the signal wave, is possible.

2. Theory and methods

2.1 Methods

At present, a theoretical study of nonlinear optical interaction in such artificial structures is at the stage of studying both experimental and theoretical in the constant-field approximation [6, 7]. But in our work to investigate the parametric interaction we use the method, constant-intensity approximation. We assume that the energy flux of the idler wave and the pump waves $S_{2,3}$ fall normally on the left side surface of the metamaterial and propagate along the positive direction of the axis. Hence the transfer of energy of the signal wave, for which the medium is "left-handed ", occurs in the opposite direction.

2.2 Theory

We assume that the medium is “left-handed” at the frequency ω_1 of signal wave only and positive for ω_2 and ω_3. In the case of negative values of dielectric permittivity and magnetic permeability at fundamental frequency ω_1 (signal wave) as well as positive values at frequencies ω_2 (idler wave), ω_3 (pump wave) the system of equations describing three wave interactions is given by [8] for high frequency pump, i.e, $\omega_3 = \omega_1 + \omega_2$

$$\begin{aligned}
&\frac{dA_1}{dz} - \delta_1 A_1 = -i\gamma_1 A_3 A_2^* e^{i\Delta z},\\
&\frac{dA_2}{dz} + \delta_2 A_2 = i\gamma_2 A_3 A_1^* e^{i\Delta z},\\
&\frac{dA_3}{dz} + \delta_3 A_3 = -i\gamma_3 A_1 A_2 e^{-i\Delta z}
\end{aligned} \qquad (1)$$

and for low frequency pump, i.e. $\omega_1 = \omega_3 + \omega_2$

$$\begin{aligned}
&\frac{dA_1}{dz} - \delta_1 A_1 = i\gamma_1 A_2 A_3 e^{-i\Delta z},\\
&\frac{dA_2}{dz} + \delta_2 A_2 = -i\gamma_2 A_1 A_3^* e^{i\Delta z},\\
&\frac{dA_3}{dz} + \delta_3 A_3 = -i\gamma_3 A_1 A_2^* e^{i\Delta z}.
\end{aligned} \qquad (2)$$

Here $A_{1,2,3}$ are the complex amplitudes of interacting waves, δ_j are the coefficients of linear absorption for corresponding frequencies ω_j (j=1-3), γ_1, γ_2 , γ_3 indicate nonlinear coupling coefficients, $\chi_{eff}^{(2)}$ is the effective quadratic susceptibility of medium and $\Delta=k_3-k_2-k_1$ (HF) , $\Delta=k_1-k_2-k_3$ (LF) are the phase mismatches between interacting waves at which take place effective pumping of energy from fundamental and idler waves to signal wave.

Using boundary conditions $A_{2,3}(z=0) = A_{20,30}\exp(i\varphi_{20,30})$, $A_1(z=\ell) = A_{1\ell}\exp(i\varphi_{1\ell})$ where $z=0$ corresponds to the input of metamaterial from the left, $A_{20,30}$, $\varphi_{20,30}$ are initial amplitudes and phases of idler and pump waves at the input of nonlinear medium from the left, $A_{1\ell}$, $\varphi_{1\ell}$ are the initial amplitude and phase of signal wave at the input into nonlinear medium from the right ($z=\ell$) we get following expression for the complex amplitude $A_1(z)$ of backward wave when it propagates from the right to the left in nonlinear medium $(\delta_j = 0)$ for LF and HF pumping correspondently:

$$A_1(z) = e^{-\frac{i\Delta z}{2}}\left\{C\cdot\cos\lambda z + \left[\frac{i\gamma_1 A_{20}A_{30}}{\lambda}e^{i(\varphi_{20}+\varphi_{30})} - iC\cdot\frac{\Delta}{2\lambda}\right]\sin\lambda z\right\}, \qquad (3)$$

$$A_1(z) = e^{\frac{i\Delta z}{2}}\left[\frac{a\cos\lambda\ell + A_{1\ell}e^{-i\frac{\Delta L}{2}+i\varphi_{1\ell}}}{\sin\lambda\ell + ib\cos\lambda\ell}\left(\sin\lambda z + ib\cos\lambda z\right) - a\cos\lambda z\right] \qquad (4)$$

Here *C*, *a* and *b*- are coefficients which were introduced to simplify the derivation of expressions. The obtained analytical expression (3) makes it possible to analyze the process of nonlinear interaction in a metamaterial in the general case when all three waves are present at the input, from the right and left side of the medium.

2.3 Optimal phase mismatches

In the equations (3) and (4) there is a parameter λ which is determined for HF and LF correspondently in the following way:

$$\lambda_{high\ freq.\ pump}^{CIA} = \sqrt{\frac{\Delta^2}{4} + \Gamma_3^2 - \Gamma_2^2} \quad ; \qquad \lambda_{low\ freq.\ pump}^{CIA} = \sqrt{\frac{\Delta^2}{4} - \Gamma_3^2 - \Gamma_2^2}\,.$$

And because of $\Gamma_3 > \Gamma_2$ from these equations follow the minimum allowable value of phase mismatches between interacting waves, when the radical expression is positive and, as a consequence, the parameter takes real values

$$\Delta^{CIA} \geq 2\sqrt{\Gamma_3^2 + \Gamma_2^2},$$

in the case of law frequency pumping. Considering HF pumping there is no such restriction, since by definition $\Gamma_3 > \Gamma_2$. As a consequence, under high-frequency pumping, the radicand remains positive for any values of the phase mismatching up to zero.

2.4 The efficiency of frequency conversion of the signal wave

In order to describe the dynamic of the process of conversion efficiency in NIM for LF and HF pumping it is necessary to introduce parameter such as the efficiency of frequency conversion of the signal wave in the medium of length *z*, as $\eta_1 = \frac{I_1(z)}{I_{20}}$. After mathematical transformations for the efficiency of frequency conversion of the signal wave, we obtain the following expressions for LF

.

$$\eta_1(z=0) = \frac{\Gamma_3^2 \sin^2 \lambda\ell}{\lambda^2 \cos^2 \lambda\ell + \frac{\Delta^2}{4}\sin^2 \lambda\ell};$$

and for HF pumping (5)

$$\eta_1 = \frac{\Gamma_3^2 \sin^2 \lambda\ell}{\left(\frac{\Delta}{2}\right)^2 \sin^2 \lambda\ell + \lambda^2 \cos^2 \lambda\ell}$$

The obtained expressions are similar to each other. The difference is only in the value of the parameter λ, which significantly distinguishes the dynamics of processes with low-frequency and high-frequency pumping.

2.5 The amplification coefficient of signal wave

Another important parameter describing the process of amplification in a metamaterial is the amplification coefficient of signal wave at the output of the metamaterial, which has the meaning of the transmittance. This factor is determined by the following expression:

$$\eta_{ampl} = \frac{I_1^{output}(z=0)}{I_1^{input}(z=\ell)} = \frac{I_1(z=0)}{I_{1\ell}}$$

And we obtained the next expressions for LF and HF pumping, correspondently

$$\eta_{ampl} = \frac{1}{\cos^2 \lambda\ell + \left(\frac{\Delta}{2\lambda}\right)^2 \sin^2 \lambda\ell} \quad ; \qquad \eta_{ampl} = \left|\frac{\sin \lambda z + ib\cos \lambda z}{\sin \lambda\ell + ib\cos \lambda\ell}\right|^2$$

3. Results and discussion

Below we present the results of a numerical analysis of the obtained analytical expressions. First, let us analyse, according to (5), the efficiency of the energy conversion of two direct waves –the pump and idler waves–into the energy of the backward signal wave.

Figure 1 shows the behavior of η_1 as a function of the total length of the metamaterial for different phase detunings and intensities of the idler wave at the input to the metamaterial in the constant-intensity approximation. Here, the dotted curves illustrate the results of the calculation in the constant-field approximation. For each phase detuning value, there is an optimal value of the total length of the metamaterial, at which the conversion efficiency is maximal. As the phase detuning increases, the amplitude of the oscillations decreases, and their frequency increases [curves (1) and

(2)].With an increase in the input intensity of the idler wave, one can observe an increase in the conversion efficiency [curves (1) and (4)] and a shift of the maxima and minima of the oscillations for solid curves obtained in the constant-intensity approximation. When the input intensity of the idler wave is increased by three times, the conversion efficiency also increases almost threefold, from 4.4 % to 13 %.

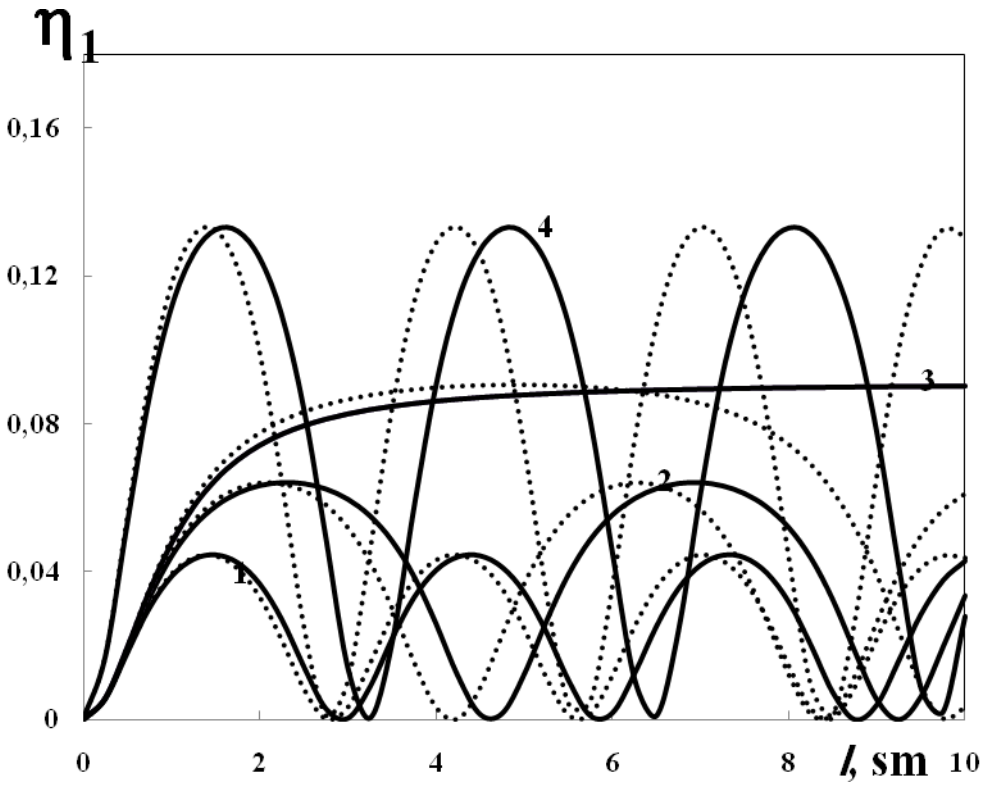

Fig. 1. Dependences of the conversion efficiency into the signal wave on the total length of the metamaterial, obtained in the constant-intensity approximation for $I_{1l} = 0$, $\Gamma_3 = 1$ sm^{-1} at Δ = (1,4) 3, (2) 2.5 and (3) 2.097688 sm^{-1}, and I_{20}/I_{30} = (1–3) 0.1 and (4) 0.3.

Figure 2 shows the dependence of the amplification factor of the signal wave at the output of the metamaterial, on the total length of the metamaterial *l*, in the absence of the idler wave at the input. There are two groups of dependences. When the phase detuning between the interacting waves is greater than the minimum allowable value, the curves oscillate [curves (3–5)]. Otherwise, the dependences are determined by the behavior of the hyperbolic sine and cosine functions, and there are no oscillations [curves (1) and (2)]. With increasing phase detuning, the frequency of oscillations increases, and the depth of modulation decrease.

On the figure 3 are shown the dependence of the amplification factor for the input signal-wave intensities I20 /I30 = 0.1 and 0.2 [curves (1–4)].

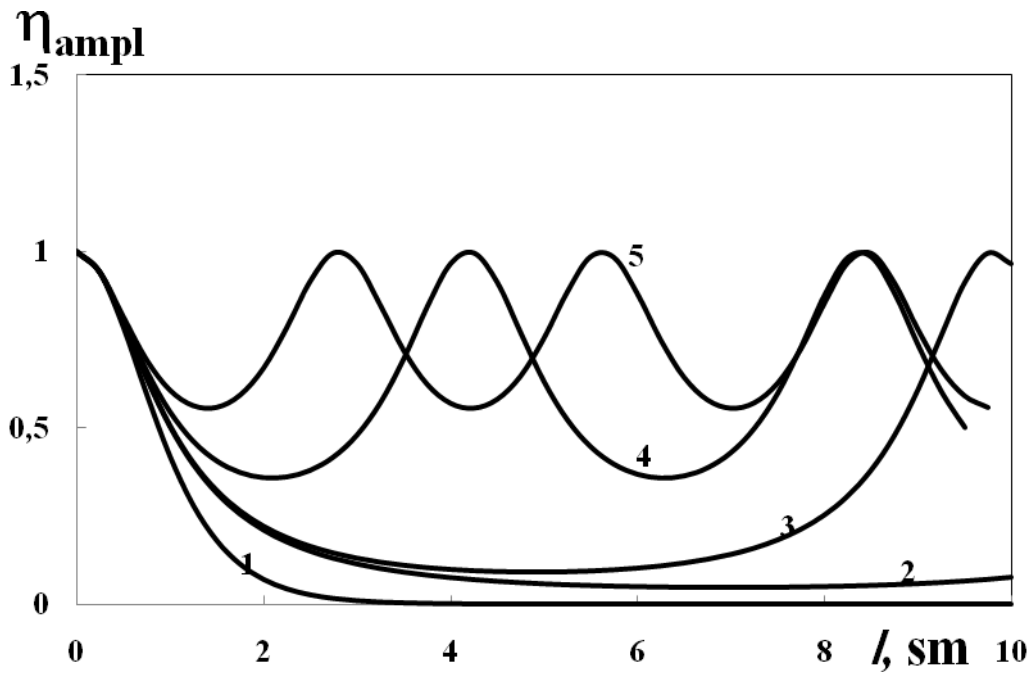

Fig. 2. Dependences of the amplification factor on the total length l of the metamaterial for I_{20} = 0 and Γ_3 = 1 cm^{-1} at Δ = (1) 0, (2) 2.05, (3) 2.1, (4) 2.5 and (5) 3 sm^{-1}.

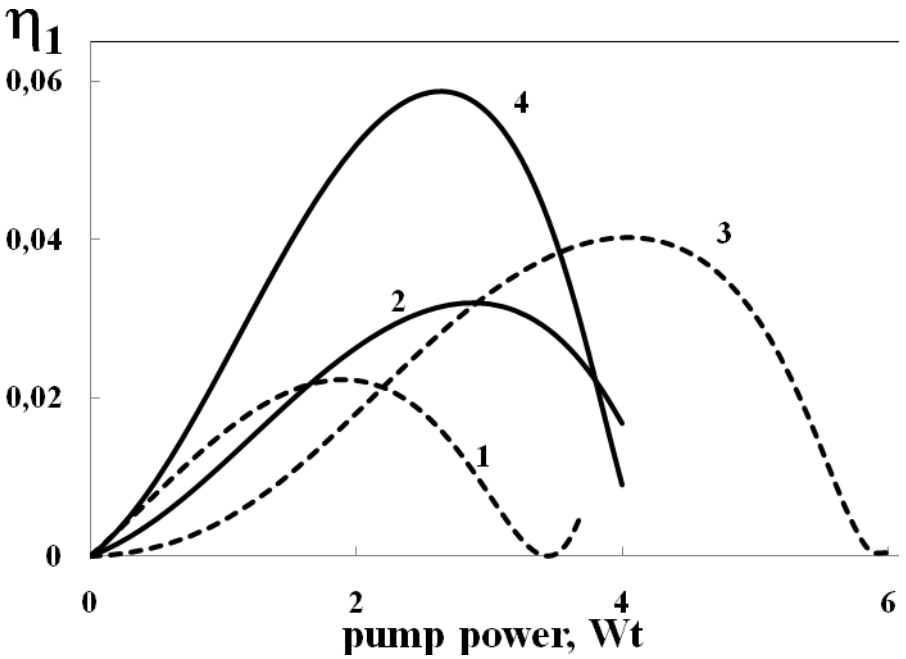

Fig. 3. Dependence of the conversion efficiency into the signal waveon the pump power for I_{1l} = 0 at I_{20}/I_{30} = (1–3) 0.1 and (4) 0.2 for Δ = (3) 5, (2,4) 5.5 and (3) 6 sm^{-1}.

As follows from the behavior of the dependences, the amplification factor at the output on the left of the metamaterial I_1(z = 0) doubles [curves (2), (4)] with increasing signal-wave intensity I_{1l} at the input (on the right) by two times at an optimum pump power of 2.85 W. Hence, by choosing a higher intensity of the backward wave at the input of the metamaterial, it is possible to realize a more intense signal wave at the output from it. Hence, by choosing a higher intensity of the backward wave at the input of the metamaterial, it is possible to realize a more intense signal wave at the output from it.

Results of calculation of $I_1(z=0)/I_{20}$) for three different levels of input intensity of a signal wave $I_{1\ell}/I_{20}=0.1;0.3;0.5$ are presented in Fig.4 (curves 1-3). As it follows from behavior of dependences, with increase in input (from the right side of metamaterial) intensity as five times, the output amplification factor in the left side, $I_1(z=0)$, of metamaterial increases nearly as twice (wherein optimum value of pump power equals 4 W). Hence, one can achieve more intense signal of reverse wave at the exit of metamaterial by choosing larger input value for reverse (signal) wave.

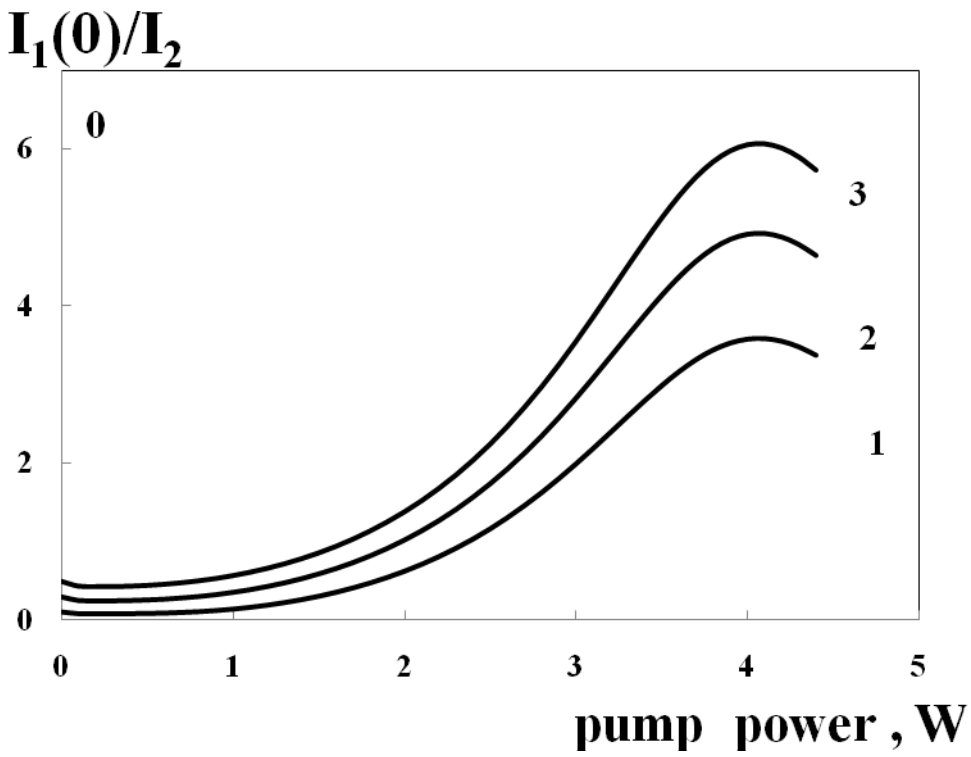

Fig. 4. Dependence of conversion efficiency in the signal wave, on the power of the pump wave for total length of metamaterial ℓ *=2 cm,* $\Delta\ell/2$ *=2.6 at* $I_{1\ell}/I_{20}=$ *0.1 (curve 1), 0.3 (curve 2), and 0.5 (curve 3).*

4. Conclusion

With allowance for the phase effects, we have considered parametric interaction of waves under low-frequency high-frequency pumping in a quadratic medium, which is 'left-handed' for the signal wave. After a single pass of the metamaterial as a result of parametric interaction of waves, it is possible to achieve the constancy of the amplitude of the signal wave by traveling waves when a certain threshold condition for the parameters of the problem. The optimal values of the pump intensity, the total length of the metamaterial and the phase detuning have been determined, which make it possible to obtain a maximum of the conversion at the required frequency. The possibility of compensation of losses of the reverse signal wave, due to the loss of direct waves. In addition, it is possible to realize smooth frequency tuning of the parametric converter at considerable pump- and idler-wave intensities. It is obtained that the efficiency of the process of amplification of the signal wave is higher, the bigger the ratio of the intensity levels of the idler and signal waves at the entrance to the metamaterial.

Reference

[1] Drachev V.P., Cai W., et al. Laser Phys. Lett., **3**, 49 (2006).
[2] Smalley JST, Vallini F, Montoya S.A., Ferrari L, Shahin S, Riley C.T, Kanté B. Nature Communications, **8**, 13793 (2017).
[3] Shumin Xiao, V.P. Drachev, A.V. Kildishev, Xingjie Ni, U.K. Chettiar, Hsiao-Kuan Yuan, V.M. Shalaev. *Nature*, **466**, 735 (2010).
[4] R.J. Kasumova, Sh.Sh. Amirov, Sh.A. Shamilova, / Quantum Electronics **47** (7) 655 – 660 (2017)

[5] R. J. Kasumova, Z. H. Tagiyev, Sh. Sh. Amirov, Sh. A. Shamilova, G. A. Safarova / Journal of Russian Laser Research, Volume **38**, Number 4, July, 2017
[6] A.K. Popov, V.M. Shalaev, *Appl. Phys. B*, **84**, 131 (2006).
[7] M. W. Klein, C. Enkrich, M. Wegener, S. Linden. Science, 28 July 2006, v. **313**, p. 502-504.
[8] J.F. Reinjes, Academic, Orlando, (1984), p. 510

INFLUENCE OF COLD-ROLLED PLASTIC DEFORMATION ON THE DEFECTIVE STRUCTURE OF TITANIUM TI-6AL-4V ALLOY

M.N. BABIKHINA[1], V.N. KUDIIAROV[1], R.S. LAPTEV[1], N.S. PUSHILINA[1], M.S. SYRTANOV[1], E.B. KASHKAROV[1], A.M. LIDER[1]

[1]National Research Tomsk Polytechnic University, 30, Lenin Avenue, Tomsk Polytechnic University, Tomsk, Russia, 634050
mnb2@tpu.ru, kudiyarov@tpu.ru, laptevrs@tpu.ru, pushilina@tpu.ru, mss12@tpu.ru, ebk@tpu.ru, lider@tpu.ru

Introduction

The presence of defects in metals and alloys has a strong negative impact on their physicochemical and mechanical properties. Theoretical calculations are mainly used at studying various types of defects, which are limited only to studying the energy of their formation and do not consider such processes as kinetics, mechanisms of formation and evolution. At the same time, a limited number of methods exist for studying these phenomena and processes in defect formation. However, the most effective and sensitive methods for identifying various kinds of defects are the methods of positron spectroscopy. These methods allow us to determine not only the type and concentration of defects, but in additional their chemical environment [1].

However, in order to obtain a quantitative and qualitative estimation of the number of defects by positron spectroscopy, additional information is needed on the base defects and their effect on the characteristics of positron annihilation. In this work, a titanium TI-6AL-4V alloy was chosen as the material for the study, since this material has found its wide application in the aircraft industry, and the study of the process of formation of various imperfections of the crystal structure in this alloy is still relevant.

In this work, the method of cold-rolled plastic deformation was used to create predominantly dislocation defects. Analysis of the time distribution of positron annihilation and coincidences of the Doppler broadening of the annihilation line was used to analyze the defects, which will allow us to establish the regularities of the change in the annihilation characteristics from the dislocation density, as well as the effect of impurities and alloying elements [1].

Taking into account all aforesaid, the aim of this work is the investigation of the effect of plastic deformation on the defect structure of titanium TI-6AL-4V alloy.

To achieve this goal, the following tasks were formulated:

1. Study of the structure and properties of titanium TI-6AL-4V alloy in various states (initial, after vacuum annealing, with different degrees of deformation during rolling);
2. Attestation of the structure and properties of samples after deformation by optical microscopy, X-ray diffraction analysis, electron-positron annihilation;
3. Establishment of correlation dependencies between the types of defects and their concentration and annihilation characteristics for titanium TI-6AL-4V alloy;
4. Determination of the minimum temperature of the start of thermal annealing of defects formed in the course of rolling in titanium TI-6AL-4V alloy.

1. Materials and methods of research

The material used was a titanium alloy (Ti-6Al-4V) of round shape, 10 mm in diameter and 4 mm in height. All surface defects (dents, coarse scratches, etc.) were removed as a result of mechanical surface treatment using sandpaper with ISO-6344 600, 1500, 2000 and 2500 markings and polishing using diamond paste. To remove rolling defects and remove internal microstresses, high-temperature vacuum annealing was performed at a temperature of 850 °C for 10 hours [2]. To obtain a different degree of deformation in the samples studied, mechanical rolling was carried out using a mechanical mill. To reveal the structure of the material, etching was carried out in acid solutions: 92 ml of H_2O, 6 ml of HNO_3, 2 ml of HF [3] and 15 ml of HF, 85 ml of H_2O [4]. The surface is one of the fundamental details in the study of the material and the metallographic analysis, and the roughness control was carried out on the Hommel Tester T1000. The roughness of the initial samples was Ra = 0.03 μm. Using a metallographic inverted microscope METAM LB, a surface survey was performed. X-ray diffraction analysis was performed using a Shimadzu XRD-7000S diffractometer. Analysis of electron-positron annihilation (EPA) was carried out on a spectrometer developed at the Tomsk Polytechnic University.

Discussion

Figure 1 shows the microstructure of a titanium alloy after high-temperature vacuum annealing.

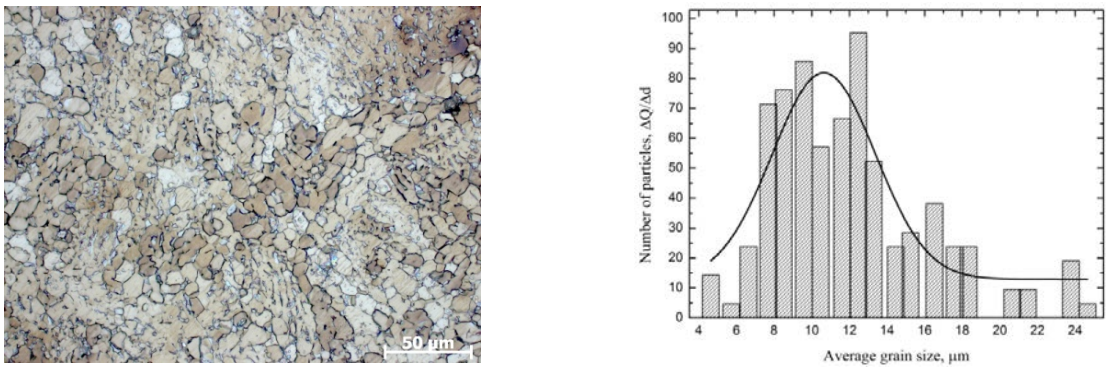

A b

Figure 1 – Microstructure (a) and histogram of grain size distribution (b) of titanium TI-6AL-4V alloy after high-temperature vacuum annealing

The microstructure of the samples after annealing (Fig. 1a) is represented by nonuniform globular grains. The average size is from 7 to 14 microns (Figure 1b).

To obtain a dislocation type of defects, cold-rolled plastic deformation was performed to various degrees of deformation. Before the plastic deformation, the alloy was subjected to high-temperature vacuum annealing before removal of internal microstresses and removal of defects.

Below are the photographs of the microstructure of the titanium alloy after rolling and the histogram of the grain size distribution.

Figures 2a and 3a show microstructures of a titanium alloy after cold-rolled plastic deformation of a minimum (0.8%) and a maximum (11.9%) degree of deformation, respectively.

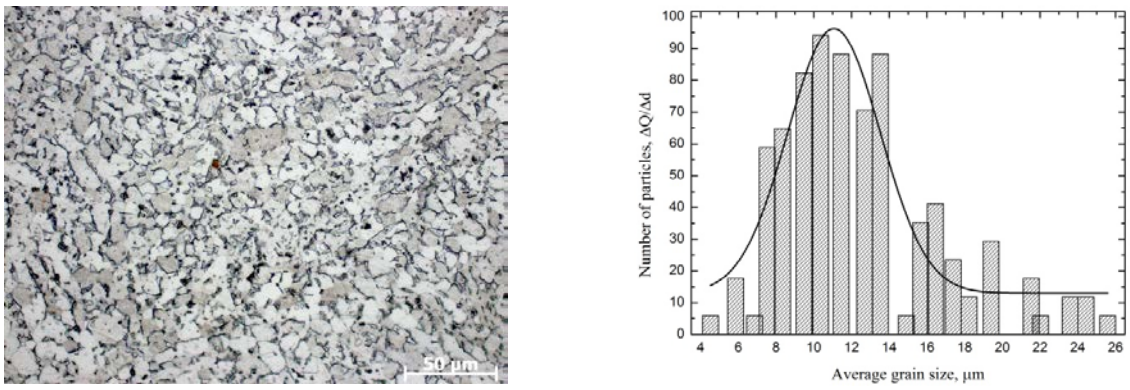

A b

Figure 2 – Microstructure (a) and histogram of grain size distribution (b) of titanium TI-6AL-4V alloy after cold-rolled plastic deformation to 0.8%

Plastic deformation up to 0.8% does not lead to significant changes in the microstructure (Fig. 2a). There is no visible stretching of grains along the rolling line. There is an insignificant decrease in grain size. The average grain size of the titanium alloy after cold-rolled plastic deformation to 0.8% is 8 to 13 µm (Fig. 2b).

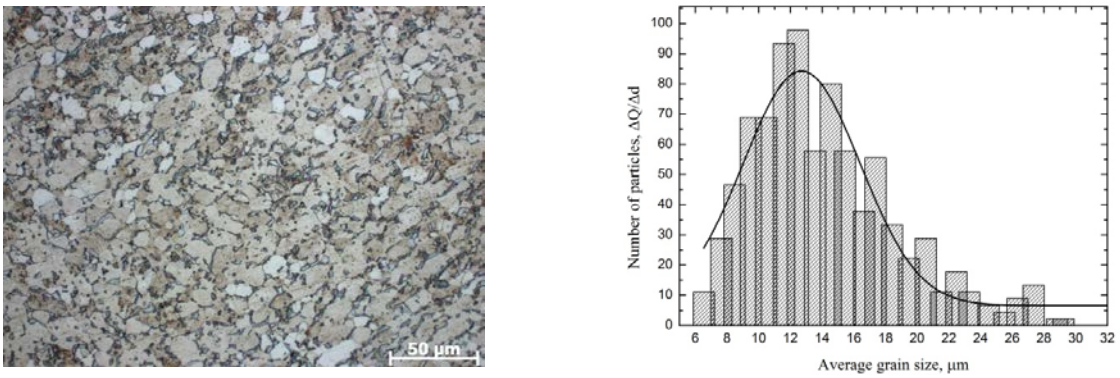

A b

Figure 3 – Microstructure (a) and histogram of grain size distribution (b) of titanium TI-6AL-4V alloy after cold-rolled plastic deformation to 11.9%

From the presented photograph of the microstructure of the titanium alloy after plastic deformation up to 11.9%, it can be seen that the shape of the grain changes. It becomes stretched along the rolling line (Fig. 3a). The average grain size varies from 8 to 15 μm (Fig. 3b).

X-ray diffraction analysis of titanium TI-6AL-4V alloy after cold-rolled plastic deformation was performed (Fig. 4).

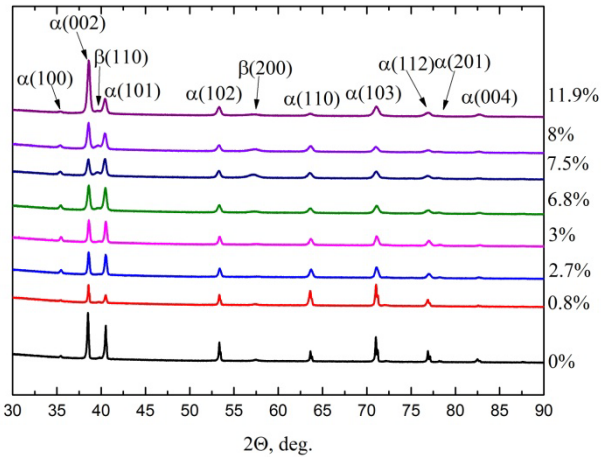

Figure 4 – Diffraction pattern of titanium TI-6AL-4V alloy after plastic deformation from 0.8 to 11.9%

From the data presented, it can be seen that there is a slight increase in the intensity of the reflections in the (002) direction with a deformation rate of 11.9%, in contrast to the initial material after high-temperature vacuum annealing. It should also be noted that there is a slight shift in the position of the reflexes relative to the original sample after high-temperature vacuum annealing.

The dislocation density was calculated by the method, which is described in detail in [5]. The results of the calculation are presented in Table 1.

Table 1. Results of calculation of the region of coherent scattering, internal elastic stresses of the second kind, and dislocation density

Degree of deformation, %	**Region of coherent scattering,**	**Internal elastic stresses of the**	**$\rho \cdot 10^{14}$, m^{-2}**
0	116	0.00161	0.34
0.8	145	0.00363	1.30
2.7	146	0.00573	2.54
3	454	0.00648	2.85
6.8	93	0.00688	3.84
11.9	58	0.0113	5.75

Figure 5 shows the dependence of the average lifetime on the degree of deformation of the titanium alloy. This dependence was obtained as a result of electron-positron annihilation analysis.

The nature of the presented dependence indicates the saturation of positrons by predominantly dislocation types of defects after a degree of deformation of 3%. It should be noted that from the results obtained, the average lifetime of a positron in dislocation types of defects corresponds to ≈175 ÷ 180 ps.

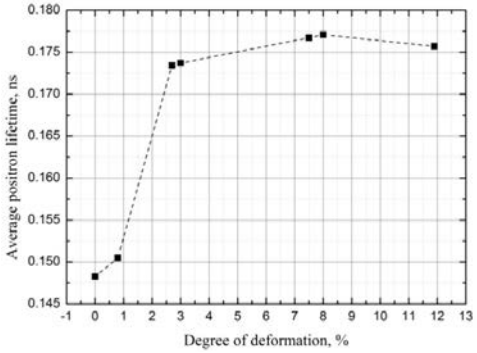

Figure 5 – Dependence of the average lifetime of positrons on the degree of deformation of a titanium TI-6AL-4V alloy. Standard deviation is 1,36×10^{-4}

Conclusion

In the present work, the effect of cold-rolled plastic deformation on the defect structure of titanium TI-6AL-4V alloy was investigated. It was found:

1. Cold-rolled plastic deformation in the range from 0.8 to 11.9% does not significantly affect the average grain size of titanium TI-6AL-4V alloy;
2. With an increase in the degree of deformation from 0.8 to 11.9%, the dislocation density increases by a factor of 17 as compared with the initial material;
3. With an increase in the degree of deformation from 0.8 to 11.9%, the electron density in the defect flow area decreases and the free volume increases.

References

[1] Lider A.M. Positron spectroscopy for controlling microstructural changes in metal-hydrogen systems: a thesis for the degree of Doctor of Engineering: special. 05.11. 13: dis. (2017).
[2] P. Hruska, J. Cı´zek, J. Knapp, F. Lukac, O. Melikhova, S. Maskova, L. Havela, J. Drahokoupil//International Journal of Hydrogen Energy. (2017).
[3] Pederson R. Microstructure and Phase transformation of Ti-6Al-4V: дис. – Luleå tekniska universitet (2002).
[4] Logacheva A.I. Логачёва А.И. Complex technology of manufacturing thin-walled elements by the method of powder metallurgy for the production of parts from structural and functional alloys based on titanium and nickel for products of rocket and space technology: dis. Dr. of Tech. Science. JSC "COMPOSITE", Korolev (2016).
[5] Savitskaya L.K. Methods of X-ray diffraction studies. Tutorial. (2003).

INFLUENCE OF LANTHANIDE ADDITIVES ON THE ELECTROLUMINESCENT CHARACTERISTICS OF InSe CRYSTALLS

A.SH.ABDINOV, R.F.BABAYEVA*, A.M.RZAZADE

Baku State University, Azerbaijan State University of Economics*
abdinov-axmed@yandex.ru, Rena_Babayeva @unec.edu.az**,** aytekinrzayeva93@gmail.com

Abstract. The effect of additives of some lanthanides - erbium and dysprosium in the structure of InSe single crystals on the dependence of the brightness of electroluminescent radiation on the temperature and electric field intensity was studied experimentally, based on statistical analysis, a qualitative scientific substantiation of the results obtained.

Key words: *Radiation, injection, brightness, spectrum, quenching of temperature, photoconductivity, recombination centers, capture centers.*

1. Introduction

Development of optoelectronics as one of the new and promising areas of modern electronics requires the creation of new semiconductor materials with high photosensitive, electroluminescent and, as well as an extensive research of their physical properties. In this aspect one of the attractive materials for researches are InSe single crystals [1]. As a result of experimental researches conducted to date, the existence of different types of local levels [2] of different origin and properties has been revealed in the band gap of these crystals [3]. In many cases precisely because of the existence in the band gap of local energy levels of a given type, InSe single crystals exhibit physical properties of scientific and practical interest [4, 5]. The phase inhomogeneity of InSe single crystals due to their layered crystal structure, as well as the weak coupling between the layers, adds to these properties additional interesting shades that are not inherent in quasi- ordered crystalline semiconductors [6-9].

Despite the researches of electroluminescent characteristics conducted in InSe single crystals so far, most of these researches were carried out either under conditions of complete elimination of the phase inhomogeneity of these crystals or under conditions of its complete presence, but its negative effect on electronic processes was replaced by the influence of various external factors. Intracrystalline factors, in particular, the phenomenon of electroluminescence in InSe single crystals under conditions of matching such a disorder by means of additives, have been explored insufficiently

On the other hand, it is known that, in terms of their physical mechanisms, the phenomena of electroluminescence and photoconductivity in semiconductors, although related to the electronic processes taking place in opposite directions, but in the same semiconductor material they both proceed depending on the various defects there.

Therefore, in the same crystal, on average, the presence of both phenomena is possible. For this reason, the determination of the phenomena of electroluminescence and photoconductivity in a semiconductor and a complex research of their characteristics in a single sample is of scientific and practical interest. Taking into account the foregoing, the present paper carried out a joint research of certain features of the phenomena of electroluminescence and photoconductivity in n-InSe single crystals doped with dysprosium and erbium.

2. Method and experiment

In the article, researches were made of dependence of the luminescent brightness (B_λ) on temperature (T) and voltage (U) (fig. 1), the dark current (i_q) of the Volt-Ampere characteristic (fig. 2), and also the exclusive dependence of the negative photoconductivity and infrared photoconductivity quenching [2] on the temperature in pure and weakly doped rare-earth elements (dysprosium - Dy and erbium - Er, $N \leq 10^{-1}$ at.%) n-InSe single crystals (fig. 3).

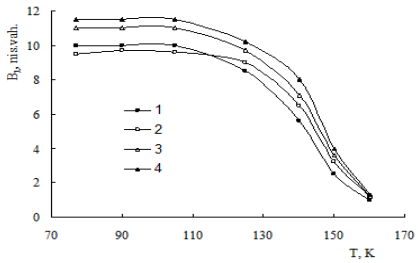

Figure 1. Dependence of brightness of electrolyuminescence radiation from temperature in pure (1) n-InSe single crystalls and doped by Er in a different range (2-4) N, at.%: 1 - 0; 2 - 10^{-5}; 3 - 10^{-3}; 4 - 10^{-1}.

The single crystal samples used in the experiments were obtained in vacuum-tempered quartz ampoules in a special temperature regime by the joint alloy method and the synthesis of constituent components taken in the stoichiometric proportion. And their doping was carried out by adding a certain amount of dysprosium to the single crystal immediately before the synthesis process. For this purpose, granular selenium, indium metal and crushed additives of Dy and Er elements of 99% purity were used InSe monocrystals were grown by the Bridgman method.

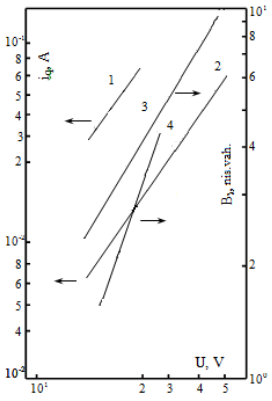

Figure 2. Volt-Amper (1, 2) and Volt-bright (3, 4) characteristics in n-InSe<Dy> single crystalls, doped by Er in a different range.N, at.%: 1, 3 - 10^{-3}; 2, 4 - 10^{-1};T=77K.

The n-InSe monocrystals, doped with rare-earth metals (irrespective of their quantitative ratio) obtained in this way in different amounts, like pure single crystals, consist of separate natural layers (several Å thick) along the length of the sample, which can be easily separated from each other. In large doped samples of single crystals, as in pure ones, the surface of the separating layers is mirror-smooth, has high resistance to the environment and chemical influence. Both in pure and in doped in different quantitative ratio rare-earth metals single crystals (10^{-5}; 10^{-4}; 10^{-3}; $5\cdot10^{-3}$; 10^{-2}; 10^{-1} at.%), the cut off samples have n-conductivity.

In n-InSe single crystals alloyed to various degrees by rare-earth metals, at 300 K, the specific dark resistance is $\rho_{to}\approx10^{2}\div10^{6}$ Ohm·cm, concentration of free charge particles and their mobility is $n_o\approx10^{14}\div10^{16}cm^{-3}$ və $\mu_o\approx50\div500cm^2/V\cdot s$ respectively. When the temperature is lowered to 77 K, the indicated parameters acquire the following values: $\rho_{to}\geq10^{4}\div10^{8}$Ohm·cm; $n_o\leq10^{13}\div10^{14}cm^{-3}$; $\mu_o\leq30\div40cm^2/V\cdot s$ respectively. Type conductivity of the tested samples in accordance with termoe.h.q., and the concentration of the main charge particles and their mobility (taking into account the experimental results obtained in research of currents bounded by the space charge) were determined on the basis of the Lambert theory [10, 11].

Various traditional methods (radiographic, photoelectric) were used to verify the composition of the samples obtained and their ability to have a uniform structure at the macroscale level. Analysis of the diffractograms of both types of InSe single crystals (pure and doped) showed that the diffraction lines (00l) of the obtained samples are induced, as in the case of single crystals at very low temperatures. In this case, there are no other types of lines, and the cell parameters calculated from the diffractograms correspond to the following values: a=4.04Å, c=16.900 Å [1].

Comparison of the obtained experimental graphs $i_q(U)$ və $B_\lambda(U)$, $B_\lambda(T)$ shows that in all the investigated samples electroluminescent radiation occurs at voltage values, at which a nonlinearity is observed on the Volt-Ampere characteristic. In this case, i_q and B_λ as a function of the voltage is same increased. A comparison of the curves for the dependence of the brightness of electroluminescent radiation (B_λ), exceptional photoconductivity (I_Φ), negative photoconductivity $\left(\Delta I_\Phi^-\right)$, and infrared photoconductivity quenching (ΔI_Φ) on temperature showed the correspondence of the temperature range on all figures, the shape of the curves and the upper temperature limit. It was found, that the maximum values for electroluminescent radiation, exclusive infrared photoconductivity extinction, negative photoconductivity, and thermal quenching of photoconductivity are achieved at the same temperature, when $T_{\lambda T}\approx T_{\Phi i}\approx T_{\lambda M}\approx T_{\Phi}$. On the other hand, all these dependences are of approximately exponential nature.

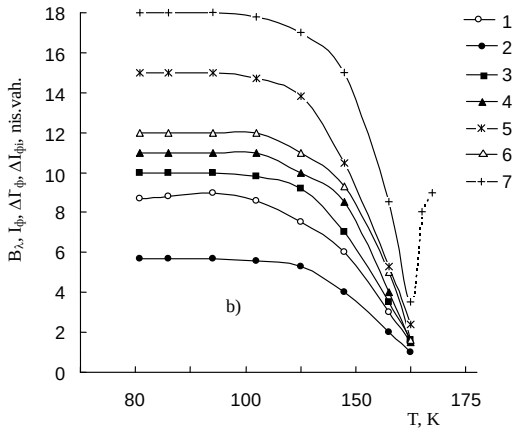

Figure 3. Dependence of electrolyuminescence (1-4), exclusive infrared photoconductivity extinction (5), negative photoconductivity, photoperiodivity in InSe single crystalls, doped by Er in a different range.
N, at.%: 1 -0; 2 - 10^{-5}; 3, 5÷7 - 10^{-3}; 4 - 10^{-1}.
$\lambda_s=\lambda_{cm}$; $\lambda_a=\lambda_{amax}$; $\Phi_s=\Phi_{smax}$; $\Phi_a=\Phi_{amax}$.

It was found that in the investigated doped samples with the considered concentrations of additives the electroluminescent and photoelectric properties and the character of the Volt-Ampere characteristic do not depend on the additive material. These characteristics and parameters depend only on the concentration of additives introduced into the structure.

Depending on the concentration of rare-earth metals introduced into the crystal, the brightness of the electroluminescent radiation either does not depend on the temperature in the case of relatively low temperatures (T≤100÷110 K), or growth with an increase in temperature by an average of 10-15% with respect to brightness at 77 K. And at temperatures above range T≥120÷130K, a decrease in the brightness of the electroluminescent radiation with increasing temperature is observed according to formula (1)

$$B_\lambda = B_\lambda(77)e^{-\frac{\Delta\varepsilon_\lambda}{kT}} \quad (1)$$

where B_λ - the brightness of the electroluminescent radiation at any considered temperature T, and $\Delta\varepsilon_\lambda$ - the activation energy of the radiation. In all tested samples at a temperature of 160 K there is a process of thermal quenching of electroluminescence.

It was found that in the investigated identical samples of n-InSe single crystals, when studying the infrared quenching spectra of the exceptional photoconductivity and negative photoconductivity responsible for recombination centers, the determined values of the penetration depth of energy - ε_r and the activation energy of electroluminescence - $\Delta\varepsilon_\lambda$ are approximately equal ($\varepsilon_r \approx \Delta\varepsilon_\lambda$). On the other hand, in different samples, a comparison of the results obtained under different conditions indicates that in the case of a change in the concentration of additives introduced into the sample, the parameters - ε_r and $\Delta\varepsilon_\lambda$ practically do not change and remain constant: $\varepsilon_r \approx \Delta\varepsilon_\lambda \approx \varepsilon_\upsilon + (0.44 \div 0.45)$ eV.

3. Discussion

A statistical analysis of the results shows that the electroluminescent radiation observed in pure and rare-earth-doped n-InSe single crystals under certain conditions occurs due to the recombination of the minority charge particles (holes) injected from the current contacts into the tested sample in r-recombination centers located at a forbidden level. For doped n-InSe single crystals, the deviation from traditional physical representations [6], which is characteristic of quasi-homogeneous crystalline semiconductor materials, is associated with their partial disorder, or rather the presence [12, 13] in their structure of macrodefects (large-size defects) [7], that have a random character. The greatest agreement between the experimental results obtained for doped ($N \approx 10^{-1}$ at.%) and pure single crystals with the lowest specific electrical resistance, and also the correspondence in these samples the electroluminescence and photoconductivity dependence to conventional physical representations characteristics of quasihomogeneous crystalline semiconductors is associated with quasi-homogeneity of these crystals.

4. Conclusion

As a result of the conducted researches it is possible to come to the following conclusion:
- the effect of additives of dysprosium and erbium introduced into the structure of n-InSe single crystals on the character of the dependence of the brightness of electroluminescent radiation on temperature is associated with the detection of a

change in the phase inhomogeneity of the crystal as a function of the concentration of additives introduced under the conditions of trapped and recombination centers of various origin and nature in the forbidden zone of the considered semiconductors;
- in doped with dysprosium and erbium n-InSe single crystals, as well as in pure crystals, electroluminescence occurs due to recombination of holes injected from current contacts into the conduction band of the crystal in recombination centers located at a level of 0.26 eV with respect to the depth of the conduction band of the crystal when applied to the voltage sample above a certain threshold value;
- in indium selenium n-InSe single crystals doped with a dysprosium and an embryum, the exponential decrease in the brightness of electroluminescent radiation with increasing temperature (at high temperatures) occurs due to the thermal quenching of electroluminescence and the thermal depopulation of recombination centers at the indicated temperatures

References

[1] Z.S. Medvedeva “Chalcogenides of elements III B of the subgroup of the periodic system” M.:, -214 P. (1968)
[2] G.A. Akhundov, A.Sh. Abdinov, N.M. Mekhtiev, A.G. Kyazym-Zade “Optics and spectroscopy” **38,** Issue 5, P. 952-954, (1975)
[3] L.E.Vorobyov, S.N. Danilov, G.G. Zegra, D.A. Firsov, V.A. Shaligin, I.N. Yassievich, E.V. Beregulin “Photovoltaic phenomena in semiconductors and quantum-size structures”. SP.. Nauka. – P. 248. (2001)
[4] F.N. Kaziev, M.K. Sheinkman, I.B. Ermolovich, G.A Akhundov. “Phys. Stat.” Sol. 31. №1. p. k59-k61,(1969).
[5] N.B. Brant, Z.D. Kovalyuk, V.A Kulbachinskiy. FTP, **22**. № 9, P.1657-1660, (1988).
[6] V.L. Bonch-Bruevich, S. G. Kalashnikov “Physics of semiconductors”. M.: Nauka, , -685 p., (1990)
[7] A.Sh. Abdinov, R.F. Babayeva Inorg. materials, **30**, №7, P. 883-886. (1994)
[8] A.Sh. Abdinov, A.G. Kazim-Zadeh “Phys. and techn. Semiconductors”, **9**, № 9, P. 1690-1693. (1975)
[9] A.Sh. Abdinov, R.F. Babayeva J. "Inorganic materials".V. **31.** № 7. P. 896-898, (1995).
[10] Abdinov A.Sh., Kazim-Zadeh A.G., Mekhtiev N.M. & others. **10,** № 1, P. 76-80. (1976)
[11] M. Lampert , P. Mark Injection currents in solids. M.: Mir, - 416 P., (1973)
[12] A.Ya. Shik “JETF”, **15**, P.408-410, (1972)
[13] A.Sh. Abdinov, R.F. Babayeva “Applied Physics”, № 5, p. 74-78, (2004)

EFFECT OF THE LOSSES ON THE EFFICIENCY OF THE CONSECUTIVE QUASI-PHASE-MATCHED GENERATION

A.R. AKHMADOVA, RENA J. KASUMOVA

Physics Department, Baku State University, 23, acad. Zahid Khalilov str.,AZ1148 Baku, Azerbaijan.
asmarahmadova@gmail.com

Abstract. A theoretical investigation has been made of simultaneous consecutive generation of optical harmonics realized within one periodically polarized crystal. The analysis is carried out in the approximation of a given intensity. It is found that when manufacturing a layered domain structure it is important to take into account the effect of the losses of interacting waves on the modulation period of the susceptibility lattice Λ.

Key words: *quasi-phase-matched; consecutive interaction; second harmonic generation; constant-intensity approximation.*

1. Introduction

One of the main problems of nonlinear optics is the conversion of coherent laser radiation at one frequency into radiation at a different frequency [1-3]. Quasi-phase-matched interactions are attractive by the ability to simultaneously realize at the output of the structure the optical coherent radiation transformed at high efficiency at several frequencies. In a quasi-phase-matched interaction, crystals with effective components of the nonlinear tensor can be used, which give a greater conversion efficiency, which was not feasible with the traditional synchronous interaction in a homogeneous medium [4-6].

Investigations carried out in a series of studies on consecutive interactions [7-9] have shown that by selecting the period of modulation of the nonlinear susceptibility and the quasi-phase-matched orders on which phase-mismatches for the corresponding harmonics are compensated, simultaneous generation of these harmonics can be achieved. This will make it possible to obtain a source of coherent radiation, simultaneously generating at several optical harmonics within one periodically polarized crystal. This was not feasible in the case of a homogeneous nonlinear medium.

In the constant intensity approximation [10-11], we performed an analysis of the quasi-phase-matched interaction at the generation of the second harmonic [12], third harmonic generation [13], total frequency generation [14-15], parametric interaction [16] and intracavity transformation [17-18] in RDS crystals. The present paper is a continuation of these studies, but for the case of consecutive interaction, which has great prospects for applications.

In the present paper, in the constant intensity approximation, the efficiency of a consecutive quasi-phase-matched interaction in a layered domain structure as a function of the losses of interacting waves is considered.

As is known, in a homogeneous medium, i.e. in a medium without modulation of the nonlinear susceptibility, an increase in conversion efficiency is observed only at odd coherent lengths, on the first, third, and so on. On the second, fourth, etc. coherent lengths, according to the definition of the coherent length, the energy of the harmonic is pumped back to the pump wave. In the case of quasi-phase-matched interaction, due to the compensation of the phase detuning on even coherent lengths, the efficiency of the transformation increases. As a result, at every subsequent coherent length (both on even and odd coherent lengths) a steady increase in conversion efficiency is observed. We note that analysis in the constant intensity approximation has shown that with increasing number of domains the coherent length increases [12-13].

For consecutive quasi-phase-matched generations, the quasi-phase-matching conditions for the second and third harmonics will be fulfilled at different orders of quasi-phase-matching, due to different phase velocities for pump waves, second and third harmonics within the modulation period of the nonlinear susceptibility Λ.

Before the present work, a theoretical analysis of the quasi-phase-matched interaction was carried out numerically [5, 8]. We used the analytical approach - the constant intensity approximation to the solution of the known system of truncated equations. This allows us to determine the optimum values of the parameters of the problem, to obtain a qualitative picture of the interaction.

2. Theory

The system of reduced equations in the case of coupled second and third harmonic generation processes is as follows [6]:

$$\frac{dA_1}{dz}+\delta_1 A_1=-i\beta_3 g(z)A_3A_2^*e^{-i\Delta_3 z}-i\beta_2 g(z)A_2A_1^*e^{-i\Delta_2 z},$$
$$\frac{dA_2}{dz}+\delta_2 A_2=-i2\beta_3 g(z)A_3A_1^*e^{-i\Delta_3 z}-i\beta_2 g(z)A_1^2e^{i\Delta_2 z}, \quad (1)$$
$$\frac{dA_3}{dz}+\delta_3 A_3=-i3\beta_3 g(z)A_1A_2e^{i\Delta_3 z}.$$

Here, A_j, $j=1\div 3$ are the complex amplitudes of the co-propagating waves for the three-frequency interaction, $\omega_j = j\omega$; δ_j is the absorption coefficients at the appropriate frequencies,

$$\beta_2=\frac{2\pi\omega_2}{cn_2}\left|\chi^{(2)}\right|, \qquad \beta_3=\frac{2\pi\omega_3}{cn_3}\left|\chi^{(2)}\right|$$

are the coefficients of nonlinear coupling of waves for generation of the second and third harmonics; $g(z)$ is a periodic function that ensures the modulation of the quadratic susceptibility over the length of the interaction z with the period $\Lambda=2l$, $g(z)$ takes successive values $+1,-1,+1,....$ on the boundary of the thickness layer l and $|g(z)|=1$.

A similar regular domain structures was considered by us in analyzing the traditional interaction of waves in the constant-intensity approximation [13-18].

We solve the system (1) with respect to the complex amplitude of the second harmonic in the constant intensity approximation, that is, under condition

$$I_{1,3}(z)=I_{1,3}(z=0)=I_{10,30}=const.$$

Using the boundary conditions, we obtain the expression for the complex amplitude of the second harmonic in the case of consecutive generation ($\delta_2=2\delta_1$)

$$A_2(z)=\exp(-\delta_2 z)\cdot\{(A_{20}\cos\varphi_{20}\cos\lambda z+A_{10}\cdot C\cdot\sin 2\varphi_{10}\cdot\sin\lambda z)+$$
$$i\cdot(A_{20}\sin\varphi_{20}\cos\lambda z-A_{10}\cdot C\cdot\cos 2\varphi_{10}\sin\lambda z)\}, \quad (2)$$

where

$$C=(2g_3^*\beta_3A_{30}+g_2\beta_2A_{10})/\lambda, \qquad \lambda=\sqrt{2\left[|g_3|^2\left(3\Gamma_{13}^2-\Gamma_3^2\right)+|g_2|^2\Gamma_{12}^2\right]}.$$
$$\Gamma_{12}=\beta_2\sqrt{I_{10}}, \quad \Gamma_{13}=\beta_3\sqrt{I_{10}}, \quad \Gamma_3=\beta_3\sqrt{I_{30}},$$
$$g_j=\frac{2}{\pi M_j}\sin(\frac{\pi M_j}{2}), \; M_j=2m_j+1, \; (m_j=0,\pm1,\pm2,..),$$

M_j - is the j-th order of quasi-phase-matched at the generation of the j-th harmonic in the case of the consecutive interaction.

In the constant-field approximation, considering $A_1(z)=A_{10}=const.$ and solving system (4) with respect to the complex amplitude of the second harmonic, we obtain

$$A_2(z)=-iA_{10}^2\beta_2g_2z\cdot\mathrm{sinc}\lambda^{CFA}z. \quad (3)$$

For the complex amplitude of the third harmonic we obtain

$$A_3(z)=-\frac{3\beta_2g_2\beta_3g_3}{(\lambda^{CFA})^2}A_{10}^3\left(1-\cos\lambda^{CFA}z\right), \quad (4)$$

where

$$\lambda^{CFA}=\sqrt{6}\beta_3g_3A_{10}.$$

3. Results and Discussion

Whence for the intensities of the harmonics we have

$$I_2(z)=\cdot A_{10}^4\cdot|g_2|^2\beta_2{}^2z^2\cdot\mathrm{sinc}^2\lambda^{CFA}z$$

and

$$I_3(z)=\frac{9}{4}\cdot I_{10}^3\cdot\left(\beta_2|g_2|\beta_3|g_3|\right)^2z^4\cdot I_{10}^3\ \mathrm{sinc}^4\frac{\lambda^{CFA}z}{2}$$

respectively. The figure shows how the conversion efficiency transforms into the second harmonic

$$\eta_2 = \frac{A_2(z) \cdot A_2^*(z)}{A_{10} \cdot A_{10}*},$$

depending on the magnitude of the losses for the second harmonic wav δ_2. As expected, there is a monotonic decrease in efficiency with increasing losses.

Further analysis showed that the magnitude of the losses affects the period of spatial beats of the second harmonic amplitude, and hence the modulation period of the susceptibility lattice.

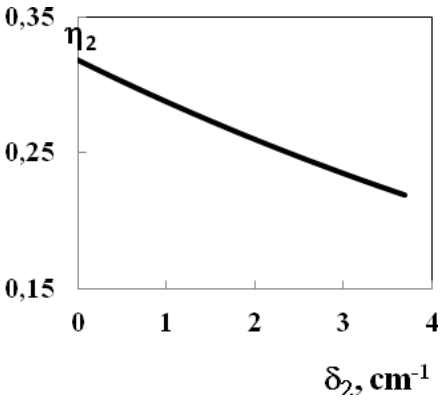

4. Conclusions

Thus, in this work, a theoretical investigation of simultaneous consecutive generation of optical harmonics realized within one periodically polarized crystal is carried out. The analysis is carried out in the constant-intensity approximation. A developed approach can be applied also in the case of parametric quasi-phase-matched interaction of optical waves.

References

[1] N. Blombergen, “Nonlinear Optics”, W.A. Benjamin, New York, 1965.
[2] R.J. Kasumova, The Basic of the Quantum Electronics. BSU, 112 p., 1991.
[3] Z.H. Tagiev, R.J. Kasumova, G.A. Safarova. Nonlinear Optics. BSU, Baku, 284 p., 2017
[4] M.M. Fejer, G.A. Magel, D.H. Jundt, R.L. Byer, IEEE J. Quant. Electron. **28,** 2631 (1992)
[5] A.S. Chirkin V.V. Volkov, Izv. Akad. Nauk SSSR (Moscow) **62** , 2354 (1998)
[6] O. Pfister, J.S. Wells, L. Hollberg, L. Zink, D.A. Van Baak, M.D. Levenson, W.R. Bozenberg, Opt. Lett., **22,** 1211 (1997)
[7] G. Z. Luo, S. N. Zhu, J. L. He, Y. Y. Zhu, H. T. Wang, Z. W. Liu, C. Zhang, N. B. Ming, Appl. Phys. Lett., **78** 3006 (2001)
[8] E.Yu. Morozov, G.D. Laptev, Izves AN, **66** (8), 1108 (2002)
[9] C. Zhang, Y. Zhu, S. Yang, Y. Qin, S. Zhu, Y. Chen, H. Liu, N. Ming, Optics Letters, **25** (7), 436 (2000)
[10] Z.H.Tagiev, and A.S.Chirkin, Zh. Eksp. Teor. Fiz., **73,** 1271 (1977) [Sov. Phys. JETP, **46,** 669 (1977)]
[11] Z.H. Tagiev, R.J. Kasumova, R.A. Salmanova, and N.V. Kerimova, J. Opt. B: Quantum Semiclas. Opt.**, 3,** 84 (2001)
[12] Z.H. Tagiev, R.J. Kasumova, Optics & Communications, **281,** 814 (2008)
[13] Z.H. Tagiev, R.J. Kasumova, G.A. Safarova, Journal of Russian Laser Research, **31** (4), 319 (2010).
[14] R.J. Kasumova, A.A. Karimi, J. of Appl. Spectr, **77** (1), 144 (2010)
[15] R.J. Kasumova, J. of Appl. Spectr, **78** (5), 659 (2011)
[16] R.J. Kasumova, A.A. Karimi, Optics and Spectroscopy, **108** (4), 624 (2010)
[17] R.J. Kasumova, Applied Optics, **51** (13), 2250 (2012)
[18] R.J. Kasumova, G.A. Safarova. J. of Appl. Spectr., **79** (6), 874 (2012)

CHALCOGENIDES FOR EFFICTIVE FREQUENCY CONVERSION

G.A. QULIEVA, RENA J. KASUMOVA, G.A. SAFAROVA

Physics Department, Baku State University, acad. Z. Khaliliv str.23,AZ1148, Baku, Azerbaijan
gulwen.2017@mail.ru, safarovagulnaraa@gmail.com

Abstract. The nonlinear parametric interactions of optical waves in a $LiGaS_2$ crystal in the case of eo-e scalar phase-matching and for a $BaGa_4S_7$ crystal in the case of oo-e scalar phase-matching are considered. As is known, both crystals are biaxial crystals. The refractive indices for the corresponding frequencies and types of scalar interaction are calculated. The obtained data will be used for further investigation of the parametric process and calculation of conversion efficiency in $LiGaS_2$ and $BaGa_4S_7$ crystals.

Key words: *ternary chalcogenide crystals, phase matching, Sellmeyer equation, constant-intensity approximation.*

1. Theory

For problems of nonlinear-optical frequency conversion in crystals, the nonlinear and phase parameters of the medium are significant. Effective frequency conversion assumes the phase-matching condition. Tunable parametric sources of coherent radiation in combination with the effects of frequency mixing make it possible to significantly expand the region of tunable wavelengths of laser radiation. To solve these problems, IR crystals are successfully used. In this range of the spectrum, there are two windows of atmospheric transparency [1-2].

As is known by the choice of crystals-converters of frequency-the main selection condition is, on the one hand, their transparency in the broad region of spectrum and on the other hand, their high nonlinear susceptibility in comparison with the existing crystals. The most suitable one as OPOs for the middle IR mcm are chalcogenide non-oxide nonlinear crystals. with a pumping near 1 mcm.

Last decades the search for nonlinear crystals continues, allowing to carry out frequency transformation in the middle IR region of the spectrum. In this regard used ternary chalcogenide crystals [3-6]. We selected $LiGaS_2$ and $BaGa_4S_7$ as the object of the study. These crystals are interesting in that they are transparent in the range from 5 to 12 μm, that is, in the middle IR range of the spectrum. They are wide-band: in $LiGaS_2$, the band gap is E_g~4.15 eV, and in $BaGa_4S_7$ it is 3.54 eV. In this case, they are characterized by low coefficients of nonlinear conversion, the nonlinear conversion coefficient d_{eff}=5.5 pm/V for the first crystal and d_{eff}=5.1 pm/V for the second crystal. However, these crystals have a high destruction threshold. On the basis of these crystals, it is possible to fabricate parametric transducers using as a pumping source the emission of a high-technology Nd:YAG laser.

As is known, the effective parametric interaction of three waves in a quadratic nonlinear medium requires the fulfillment of the frequency relationship, as well as the phase matching condition:

$$\omega_1 + \omega_2 = \omega_3$$

and

$$\vec{k}_1 + \vec{k}_2 = \vec{k}_3 .$$

The coefficients of the nonlinear coupling in the parametric transformation are determined by the following expressions:

$$\gamma_{s,i} = \frac{8\pi^2}{\lambda_{s,i} n_{s,i}} d_{eff}, \quad \gamma_p = \frac{4\pi^2}{\lambda_p n_p} d_{eff} .$$

In our study, we consider the nonlinear parametric interaction of optical waves in a $LiGaS_2$ crystal in the case of eo-e scalar phase-matching and for a $BaGa_4S_7$ crystal in the case of oo-e scalar phase-matching. The study of the parameter process will allow us to determine threshold value of pumping wave amplitude.

For nonlinear conversion, theoretical analysis of wave interaction is made by using the known system of the reduced equations

$$\begin{aligned}
&\frac{dA_s}{dz} + \delta_s A_s = -i\gamma_s A_p A_i^* \exp(i\Delta z), \\
&\frac{dA_i}{dz} + \delta_i A_i = -i\gamma_i A_p A_s^* \exp(i\Delta z), \\
&\frac{dA_p}{dz} + \delta_p A_p = -i\gamma_p A_s A_i \exp(-i\Delta z)
\end{aligned} \tag{1}$$

Here $A_{s,i,p}$ are the complex amplitudes of the signal, idler and pump waves at respective frequencies $\omega_{s,i,p}$ in direction of axis z. The nonlinear coefficients and loss parameters for j-th wave ($j = s, i, p$) are labeled as γ_j and δ_j, respectively. And phase mismatch between the interacting waves is given by $\Delta = k_p - k_s - k_i$.

We solved the reduced system of equations (1) in the constant-intensity approximation with corresponding boundary conditions while the conditions of experiments were taken into account.

The boundary conditions become as follows

$$A_{p,i,s}(z=0) = A_{po,io,so}\exp(i\varphi_{po.io,so}), \tag{2}$$

where $\varphi_{po,io,so}$ are an initial phases of pump, idler and signal waves at the entry of the medium and $z = 0$ corresponds to the entry of crystal.

2. Results and Discussion

The main requirement, as we know, for proceeding of nonlinear optical process is the necessity of optimum phase relationship between interacting waves. Breaking of these conditions will bring up the mismatch of the phases and as consequence the inefficiency of nonlinear process will decrease. One of the main reasons responsible for infringement of the condition of maximal phase correlation is the phase mismatch.

The choice of the type of interaction is determined by the experimental conditions [7]. To this end, we calculate the refractive indices for the corresponding frequencies and types of scalar interaction. First, we determine the refractive indices for the crystals under study at the wavelengths of the idler wave (μm), the pump wave (μm), and the signal wave. To this end, we calculate the refractive indices for the corresponding frequencies and types of scalar interaction. First, we determine the refractive indices for the crystals under study at the wavelengths of the idler wave ($\lambda_i = 5.457$ μm), the pump wave ($\lambda_p = 1.0642$ μm), and the signal wave.

First of all, we determine the length of the signal wave from the condition

$$\frac{1}{\lambda_p} = \frac{1}{\lambda_i} + \frac{1}{\lambda_s}.$$

In the case of $LiGaS_2$, we obtain for the wavelength of the signal wave $\lambda_s = 1.322013$ μm, and in the case of $BaGa_4S_7$ we obtain $\lambda_s = 1.28399$ μm

As is known, both crystals are biaxial crystals. The method for determining the angular widths of phase-matching, originally introduced and used for uniaxial crystals, can be used for biaxial crystals. For these crystals, the phase-matching directions are conical surfaces of the fourth order, whose axis is one of the crystal axes [8].

The Sellmeyer equation for $LiGaS_2$ has the form [9]

$$n^2(\lambda) = A_0 + \frac{A_1}{\lambda^2 - 2A_2} - A_3\lambda^2, \tag{3}$$

where A_0, A_1, A_2, A_3 taken from experimental work [3].

From (1) we calculate the refractive indices for all three waves

$$n_e^p = 2.124105,\ n_0^s = 2.134473,\ n_e^i = 2.076045,$$

at

$$\lambda_p = 1.0642 \text{ mcm};\quad \lambda_s = 1.322013 \text{ mcm},\ \lambda_i = 5.457 \text{ mcm}.$$

The Sellmeyer equation for $BaGa_4S_7$ has the form [3]

$$n^2 = A_1 + \frac{A_3}{(\lambda^2 - A_2)} + \frac{A_5}{(\lambda^2 - A_4)} \tag{4}$$

where A_1, A_2, A_3, A_4 taken from experimental work [3].

From (2) we calculate the refractive indices for all three waves

$$n_e^p = 2.319966 \qquad n_0^s = 2.289489 \qquad n_0^i = 2.242884$$

at

$$\lambda_p = 1.0642 \text{ mcm};\qquad \lambda_s = 1.28399 \text{ mcm},\qquad \lambda_i = 6.217 \text{ mcm}.$$

Thus, the obtained data will be used for further investigation of the parametric process, calculation of conversion efficiency in $LiGaS_2$ and $BaGa_4S_7$ crystals and for determining the threshold regime for parametric interaction.

3. Conclusion

Thus, the article investigates the parametric interactions of optical waves in a $LiGaS_2$ crystal in the case of eo-e scalar phase-matching and for a $BaGa_4S_7$ crystal in the case of oo-e scalar phase-matching. Calculated with high accuracy, the refractive indices of the two types of interaction at the appropriate frequencies will

allow us to determine the exact dynamics of the nonlinear efficiency transformation in $LiGaS_2$ and $BaGa_4S_7$ crystals. An absence of two-photon absorption makes this compound suitable for optical parametrical converters at 1.0642 nm. As a pump source, a technologically advanced Nd:YAG laser can be used. On the basis of these crystals, it is possible to develop effective frequency converters of the infrared range.

References

[1] R.J. Kasumova. The Basic of the "Quantum Electronics", BSU, 112p., (1991)
[2] Z.H. Tagiev, R.J. Kasumova, G.A. Safarova. "Nonlinear Optics", BSU, Baku, 284p., (2017)
[3] V. Badikov, D. Badikov, G. Shevyrdayeva, A. Tyazhev, G. Marchev, V. Panyutin, and V. Petrov, OSA/CLEO: Science and Innovations. Baltimore, maryland US, May 1-6, (2011).
[4] V. Petrov, Optical Materials, **34,** 536 (2012)
[5] R.J. Kasumova, G.A. Safarova, N.V. Kerimova, International Scientific and Practical Conference "WORLD SCIENCE", **1** (4), 67 (2015)
[6] R.J. Kasumova, G.A. Safarova, N.V. Kerimova, International Journal of Engineering and Computer Science ISSN:2319-7242, **3,** 7823 (2014)
[7] A.Tyazhev, D. Kolker, G. Marchev, V. Badikov, D. Badikov, G. Shevyrdayeva, V. Panyutin, and V. Petrov, Optics Letters, **37** (20), 2141(2012)
[8] S.G. Grechin,. Quantum Electronics, **40** (9), 822 (2010)
[9] L. Isaenko, A. Yelisseyev, S. Lobanov, P. Krinitsin, V. Petrov, J.-J. Zondy, J. of Noncrystalline Solids, **352,** 2439 (2006)

NON STATIONARY REJIM OF GENERATION IN METAMATERIALS

L.V. PRIYEVA, RENA J. KASUMOVA

Physics Department, Baku State University, 23, acad. Zahid Khalilov str.,AZ1148 Baku, Azerbaijan
prieva.l7@mail.ru, renajkasumova@gmail.com

Abstract. The nonstationary generation of pulses is investigated in the first approximation of dispersion theory in new materials engineered to have a property that is not found in nature in metamaterials. An analytical expression is obtained for the complex amplitude of the signal wave at the output of the metamaterial in the constant field approximation. A further analysis of the expression obtained will make it possible to study the dynamics of the behavior of the spectrum, determine the optimum values of the pump intensity, and determine how the shape of the signal wave spectrum changes.

Key words: *nonstationary generation, ultrafast pulse, group velocity detuning, metamaterial.*

1. Introduction

Femtosecond lasers generating pulses of duration of the order of 10 fs are widely used in solving a wide range of applied problems in the field of high-precision material processing technologies, biomedical technologies, etc. [1-2]. Such lasers are able to concentrate the light flux in an extremely short time interval. This makes it possible to achieve colossal peak power values in the pulse.

The peak power of the laser pulse~10^{14} W, generated by a modern multi-terawatt laser system, is tens of times higher than that of all energy sources on the planet [3-4]. Currently, the record intensities achieved in the focus of the laser beam are~$10^{21} \div 10^{22}$ W/cm^2. When the substance is heated by such pulses, temperatures of tens and hundreds of millions of degrees are reached, which corresponds to the initiation temperatures of nuclear reactions. Of great interest is the study of the conversion of the frequency of ultrashort pulses in metamaterials [5-7].

Metamaterials are composite materials whose properties are due not so much to the individual physical properties of their components as to the microstructure. These microstructures can be considered as atoms of extremely large sizes artificially introduced into the initial material. Usually, to obtain the required electromagnetic characteristics, researchers select the chemical composition of the material. But as an example of metamaterials shows, chemistry is not the only way to obtain interesting properties of matter. The electromagnetic response of the material can be "designed" by introducing tiny structures [8].

Investigation of materials exhibiting simultaneously negative electric and magnetic properties in the optical range of the spectrum stimulated intensive studies of nonlinear optics of metamaterials, including second-order nonlinear optical phenomena such as second harmonic generation, generation of sum and difference frequencies, and optical parametric amplification, as well as cubic nonlinear interactions of ultrashort elm pulses with a metamaterial.

In the present paper, nonstationary generation of pulses is investigated in the first approximation of dispersion theory [9-10] in new art material, in metamaterials.

1. Theory

In considering, we assume for definiteness that for a parametric three-wave interaction in a metamaterial, the medium is "left" only at the frequency of the signal wave. We assume that the pump wave is a long pump pulse at a frequency, in contrast to a short wave pulse at a difference frequency ω_1. We assume that the pump wave is a long pump pulse at a frequency ω_2, in contrast to a short wave pulse at a difference frequency $\omega_2 = \omega_3 - \omega_1$.

We assume that the energy fluxes of the pump wave and the waves at the difference frequency $S_{2,3}$ fall normally on the left side surface of the metamaterial of length ℓ and propagate along the positive direction of the axis z. Hence the transfer of energy of the signal wave, for which the medium is "left", occurs in the opposite direction. In the case under consideration, there is a counter interaction between the initial short pulse with the excited signal wave.

With the geometry of interacting waves in the metamaterial under consideration, the usual truncated equations for pump waves and waves on the total, difference frequency take the form:

$$\left(\frac{\partial}{\partial z}-\frac{1}{u_1}\frac{\partial}{\partial t}-i\frac{g_1}{2}\frac{\partial^2}{\partial t^2}-\delta_1\right)A_1=i\gamma_1 A_3 A_2^* e^{i\Delta z},$$
$$\left(\frac{\partial}{\partial z}+\frac{1}{u_2}\frac{\partial}{\partial t}-i\frac{g_2}{2}\frac{\partial^2}{\partial t^2}+\delta_2\right)A_2=-i\gamma_2 A_3 A_1^* e^{i\Delta z}, \quad (1)$$
$$\left(\frac{\partial}{\partial z}+\frac{1}{u_3}\frac{\partial}{\partial t}-i\frac{g_3}{2}\frac{\partial^2}{\partial t^2}+\delta_3\right)A_3=-i\gamma_3 A_1 A_2 e^{-i\Delta z}.$$

Here A_1, A_2 and A_3 are the complex amplitudes of the signal wave at the frequency ω_1, the pump waves at the frequency ω_2 and the waves at the sum frequency ω_3. u_1 u_2 and u_3 are group velocities of the corresponding waves, γ_1, γ_2 and γ_3 are coefficients of nonlinear coupling of waves at the corresponding frequencies,

$$\gamma_1=\frac{8\pi}{k_1c^2}\chi_{eff}^{(2)}\omega_1^2\varepsilon_1, \quad \gamma_2=\frac{8\pi}{k_2c^2}\chi_{eff}^{(2)}\omega_2^2\varepsilon_2, \quad \gamma_3=\frac{8\pi}{k_3c^2}\chi_{eff}^{(2)}\omega_3^2\varepsilon_3,$$

$g_{1,2,3}$ are the dispersion spreading coefficients,

$$g_{1,2,3}=\frac{\partial^2 k(\omega_{1,2,3})}{\partial\omega_{1,2,3}^2},$$

$\delta_{1,2,3}$ - are loss of interacting waves, $\Delta=k_3-k_2-k_1$ is the phase mismatching from the central frequency of the pump wave.

We will consider, in a first approximation, the theory of dispersion, that is, without taking into account the effect of dispersive spreading. In this case, the system of truncated equations (1) has the form ($\delta_j=0$)

$$\left(\frac{\partial}{\partial z}-\frac{1}{u_1}\frac{\partial}{\partial t}\right)A_1=i\gamma_1 A_3 A_2^* e^{i\Delta z},$$
$$\left(\frac{\partial}{\partial z}+\frac{1}{u_2}\frac{\partial}{\partial t}\right)A_2=-i\gamma_2 A_3 A_1^* e^{i\Delta z}, \quad (2)$$
$$\left(\frac{\partial}{\partial z}+\frac{1}{u_3}\frac{\partial}{\partial t}\right)A_3=-i\gamma_3 A_1 A_2 e^{-i\Delta z}.$$

The main requirement, as we know, for proceeding of nonlinear optical process is the necessity of optimum phase relationship between interacting waves. Breaking of these conditions will bring up the mismatch of the phases and as consequence the inefficiency of nonlinear process will decrease. One of the main reasons responsible for infringement of the condition of maximal phase correlation is the phase mismatch.

We solve the problem in the case when a pump wave and a wave at a frequency ω_3 are present at the entrance to a medium with negative refraction

$$A_1(z=l)=0;$$
$$A_2(z=0)=A_{20}; \quad (3)$$
$$A_3(z=0)=A_{30}$$

We solve the system (2) in the constant-field approximation, i.e.

$$A_2(z,t)=A_{20}=const.$$

3. Results and Discussion

As is well known in the study of the nonstationary wave interaction, it is more convenient to operate with the Fourier component of the ultrashort wave pulse. In the constant-field approximation, and in the first approximation of

dispersion theory with the use of the spectral approach (Fourier transforms), the solution of the system (2) is found in the following sequence.

First, we go from the field amplitudes to the amplitudes of the spectrum, i.e. to the Fourier components of the pulses. This approach, based on the study of frequency spectra, makes it possible to clearly visualize the interaction pattern.

Then, solving the obtained system of equations with respect to the complex amplitude of the Fourier spectrum of the signal wave.

As a result, for the complex amplitude of the signal wave at the output of the metamaterial, taking into account the boundary conditions (3) in the constant field approximation, we obtain

$$A_1(z=0,\omega) = -i\gamma_1 A_{30} A_{20}^* \exp\left(i\frac{\omega+\Delta}{2}z\right)\cdot\frac{\tan\lambda l}{\lambda - \frac{i}{2}(\Delta - \nu\omega)\tan\lambda l},$$

where $A_{1,2,3}$ are the complex amplitudes of the signal wave at the frequency ω_1, the waves at the difference frequency ω_2, and the pump waves at the frequency ω_3, $A_{20,30}$ are the input values of the corresponding waves,

$$\nu = \frac{1}{|u_1|} - \frac{1}{u_3}, \qquad \lambda = \sqrt{\frac{(\omega\nu+\Delta)^2}{4} - \Gamma_2^2},$$

$$\Gamma_2^2 = \gamma_1\gamma_3 I_{20}, \qquad I_{20} = A_{20}\cdot A_{20}^*.$$

Thus, the analytical expression obtained for the complex amplitude of the signal wave at the output of the structure will allow us to theoretically investigate the dynamics of the behavior of the spectrum for various parameters of the problem. Determine the optimum values of the pump intensity and find out how the shape of the signal wave spectrum changes.

4. Conclusion

Thus, the nonstationary generation of pulses is investigated in the constant-field approximation forfirst approximation of dispersion theory in metamaterials. This approximation of dispersion theory takes into account only the group velocity mismatching. The study of the nonstationary wave interaction was carried out by the method of Fourier transforms. A further analysis of the expression obtained will make it possible to study the dynamics of the behavior of the spectrum, determine the optimum values of the pump intensity, and determine how the shape of the signal wave spectrum changes.

References

[1] B. M. Wu, G. P. Williams, A. Tan, J. S. Mehta, J. Ophthalmol**.,** 616478 (2015)
[2] P. Kukura, D.W. McCamant, S. Yoon, D.B. Wandschneider, R.A. Mathies, Science, **310,** 1006 **(**2005)
[3] R.J. Kasumova, “The Basic of the Quantum Electronics”, BSU, 112p., 1991
[4] Z.H. Tagiev, R.J. Kasumova, G.A. Safarova., “Nonlinear Optics”, BSU, Baku, 284p., 2017
[5] V.G. Veselago, Sov. Phys. Usp., 10, **509**(1968)
[6] D.R. Smith, W.J. Padilla, D.C. Vier, S.C. Nemat Nasser, and S. Schultz, Phys. Rev. Lett., **84,** 4184 (2000)
[7] R.J. Kasumova, Sh.Sh. Amirov, Sh.A. Shamilova, Quantum Electronics, **47** (7), 655 (2017)
[8] W. Cai, V.M. Shalaev, Optical Metamaterials: Fundamentals and Applications, New York: Springer, 102p., 2010
[9] V. Roppo, M. Centini, C. Sibilia, M. Bertolotti, D. de Ceglia, M. Scalora, N. Akozbek, M.J. Bloemer, J.H. Haus, O.G. Kosareva, V.P. Kandidov, Phys. Rev. A, **76** (3), 033829 1-12 (2007)
[10] S. Wen, Y. Xiang, X. Dai, Z. Tang, W. Su, and D. Fan, Phys. Rev. A**, 75**, 033815 (2007)

Structure and optical properties of polymer nanocomposites based on PVC+ZnS

M.A.RAMAZANOV[a], F.V.HAJIYEVA[a], A.M.MAHARRAMOV[a], H.A.SHIRINOVA[a], Y.A.BABAYEV[b], G.V.VALADOVA[b].

[a]*BakuStateUniversity, Z. KhalilovStreet 23, Baku, AZ1148, Azerbaijan*
[b]*Baku Engineering University, Hirdalan city, HasanAliyevstr 120*
mamed_r50@mail.ru, fhajiyeva@bsu.edu.az

Abstract. In this paper, polymer nanocomposites based on polyvinyl chloride and zinc sulphide nanoparticles were obtained and investigated. SEM analysis showed that the average nanoparticle size for PVC+ZnS based nanocomposites is 3-5 nm. From UV spectra of nanocomposites by extrapolation method the width of the forbidden band for polymer nanocomposites was determined.It was found that the bandgap for thenanocomposites based on PVC+3% ZnS is 4.2eV; for PVC+5% ZnS-4.0 eV; for PVC+10% ZnS-3.95 eV. The photoluminescence properties of nanocomposites based on PVC+ZnS are studied. It has been found that thepeaks at 356 nm, 375 nm, 528 nm, 540 nm, 562 nm, 593 nm on the photoluminescence spectrum of thenanocomposites are luminescent peaks belonging to ZnS nanoparticles. The influence of thermal annealing on the photoluminescence properties of nanocomposites based on PVC+ ZnS has also been studied.It has been determined that with increasing thermal annealing temperatureup to 120^0Cintensity of photoluminescence also increases. The increase in the intensity of the photoluminescence with increasing thermal annealing temperature is explained by the complete removal of the solvent from the volume of the polymer and thereby improving the photoluminescence efficiency of the nanocomposites.

Key words: *nanocomposite, zinc sulphide, nanoparticles, polyvinyl chloride*

1. Introduction

Synthesis and study of the structure and properties of polymer nanocomposites are priority directions of modern science in connection with the unique properties of nanostructured materials. This complex of properties determined quantum-size and Coulombeffects in the nanoparticles and depends on the chemical nature of the particles, their size and shape, spacing, size distribution and regularity. Polymer nanocomposites attract attention due to the possibility of stabilization in polymeric matrices of various nanoparticles. The use of various polymers with dielectric and semiconducting properties as a matrix also makes it possible to purposefully vary the parameters of the composites. Polymer nanocomposites with semiconductor nanoparticles may exhibit unique physical properties, combining characteristics of semiconductors and polymeric films, and the presence of nanoparticles in the polymer matrix could lead to entirely new effects. Design and creation of fine luminescent polymer composite materials based on semiconductor quantum dots, including zinc sulphideZnS is an urgent and important task of both the scientific and practical points of view. In these materials the quantum size effect influences the width of the forbidden band, which makes them attractive for the manufacture of optoelectronic emitters (LEDs), single electron transistors, quantum dot displays, lasers, etc. [1].
This paper is devoted to the synthesis and stabilization of ZnS semiconductor nanoparticles, develop polymeric nanocomposites based on zinc sulphide nanoparticles and a thermoplastic polyvinyl chloride matrix and study of optical and photoluminescent properties of nanocomposites based on PVC+ZnS.

2. Experimental section

2.1. Materials

All chemicals were used as received: polyvinylchloride (PVC code CAS 9002-86-2) has a density 1.34 g/cm^3, melting temp -150-220°C, mol.wt Mw - 140000by GPC, spark temp - 625° C, ignition temp - 500° C, auto-ignition temp->1100°C), zinc chloride ($ZnCl_2$, PLC 141779), sodium sulfide (Na_2Sx9H_2O, PLC 141687), CTAB (cetyltrimethylammonium bromide, $C_{19}H_{42}BrN$, AB 117004, 98% chemically pure), tetrahydrofuran (PLC 143537).

2.2. Preparation of ZnS NPs and PVC-ZnS based nanocomposites.

ZnSNPs were prepared by chemical co-precipitation method. The ZnS nanoparticles were synthesized in the presence of the cationic surface active substance CTAB as follows: 50 ml 0,05 M $ZnCl_2$ solution wasmixedwith 10 ml 0,5% CTAB solution in a magnetic stirrerduring 10 minutes. Further solution of 50 ml 0,05 M sodium sulfide (Na_2S) was added to the primary solution and was intensely stirred at ambient temperature during two hours. In order to removenon-interacting ions Zn^{2+} and S^{2-} and get purified ZnS NPs, the mixture were distilled several times with deionized water and ultracentrifugedduring 10 ~~min~~.minutes.Purified ZnS NPs were transferred into the petri dish and let it dry during 24 hours[2,3].

For synthesize PVC-ZnSnanocomposites, 0.1 g PVC powder dissolved in 30 ml tetrahydrofuran (THF) solution. ZnS NPs in different weight contents(3%,5%,10%) were added into THF polyvinylchloride solution and mixed on a magnetic stirrer for 9 hours almost at 60^0C. Then the homogeneous mixture was transferred to the petri dish and put it to dry duringaday. For completely removal of THF from the volume of the polymer, nanocomposites were dried in vacuum oven during 1 hour.Thin nanocomposite samples were obtained by hot pressing at the melting temperature of PVC(150^0C) at a pressure of 10 MPa. The cooling of the nanocomposite films after hot pressing was carried out in water at a cooling rate of 200 deg/min.

2.3. Characterization

The images of the nanocomposite samples have been obtained by scanning electron microscope (SEM, Jeol JSM-7600 F). Scanning was performed in SEI mode at an accelerating voltage of 15 kV and a working distance of 4.5 mm. Energy dispersive micro-X-ray analysis was performed using the device X-Max 50 (Oxford Instruments). The UV-vis spectra have been recorded on Spectrophotometer Specord250 Plus at 200-700 nm and ambient temperature. Photoluminescent properties of nanocomposite films were examined using a spectrofluorometer Varian Cary Eclipse at wavelength range 200-900 nm.

3. Results and discussion

The morphology of nanocomposites and the distribution of ZnS nanoparticles in a polyvinyl chloride matrix were studied by SEM analysis. Figure 1 shows SEM images of nanocomposites based on PVC+ZnS as a function of the concentration of ZnS nanoparticles. As can be seen from Fig. 1, the average size of nanoparticles based on PVC+ZnS is 3-5 nm. Figure 2.shows the energy-dispersive spectrum (EDS) spectrum of the nanocompositePVC+ZnS. From the EDS spectrum it is seen that the nanocomposite consists of pure ZnS nanoparticles. The elements of Cu, Zn, Si on the EDS spectrum come from the substrate used to deposit the main ZnS nanoparticles.

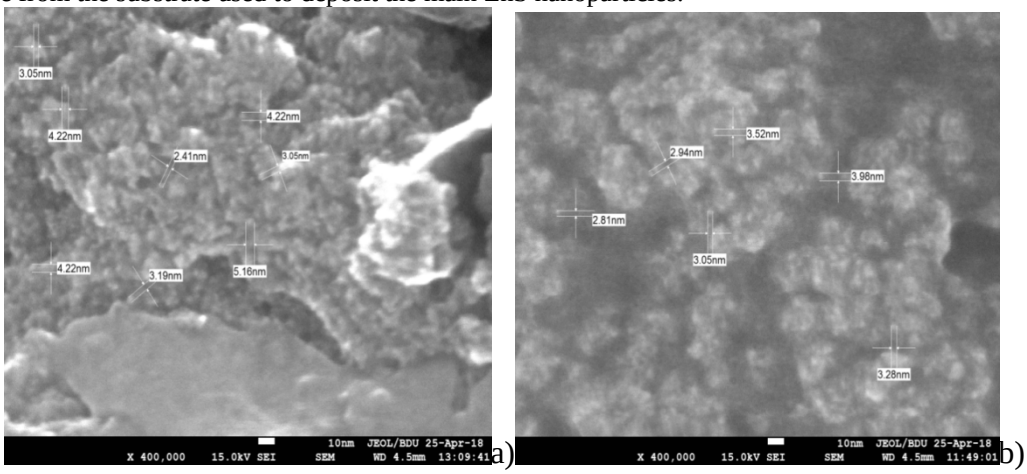

Fig.1. SEM images of nanocomposites based on PVC+ZnS: a) PVC+3% ZnS; b) PVC+10% ZnS.

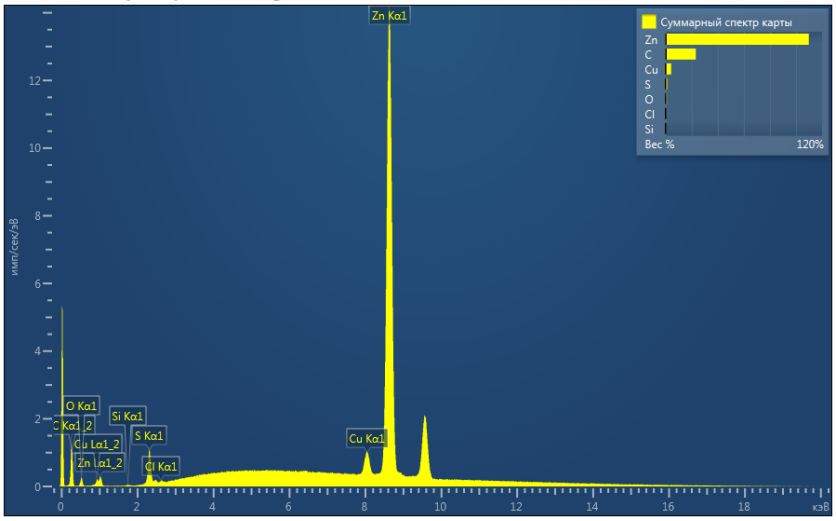

Fig. 2.EDSspectrum of nanocomposites based on PVC+ZnS.

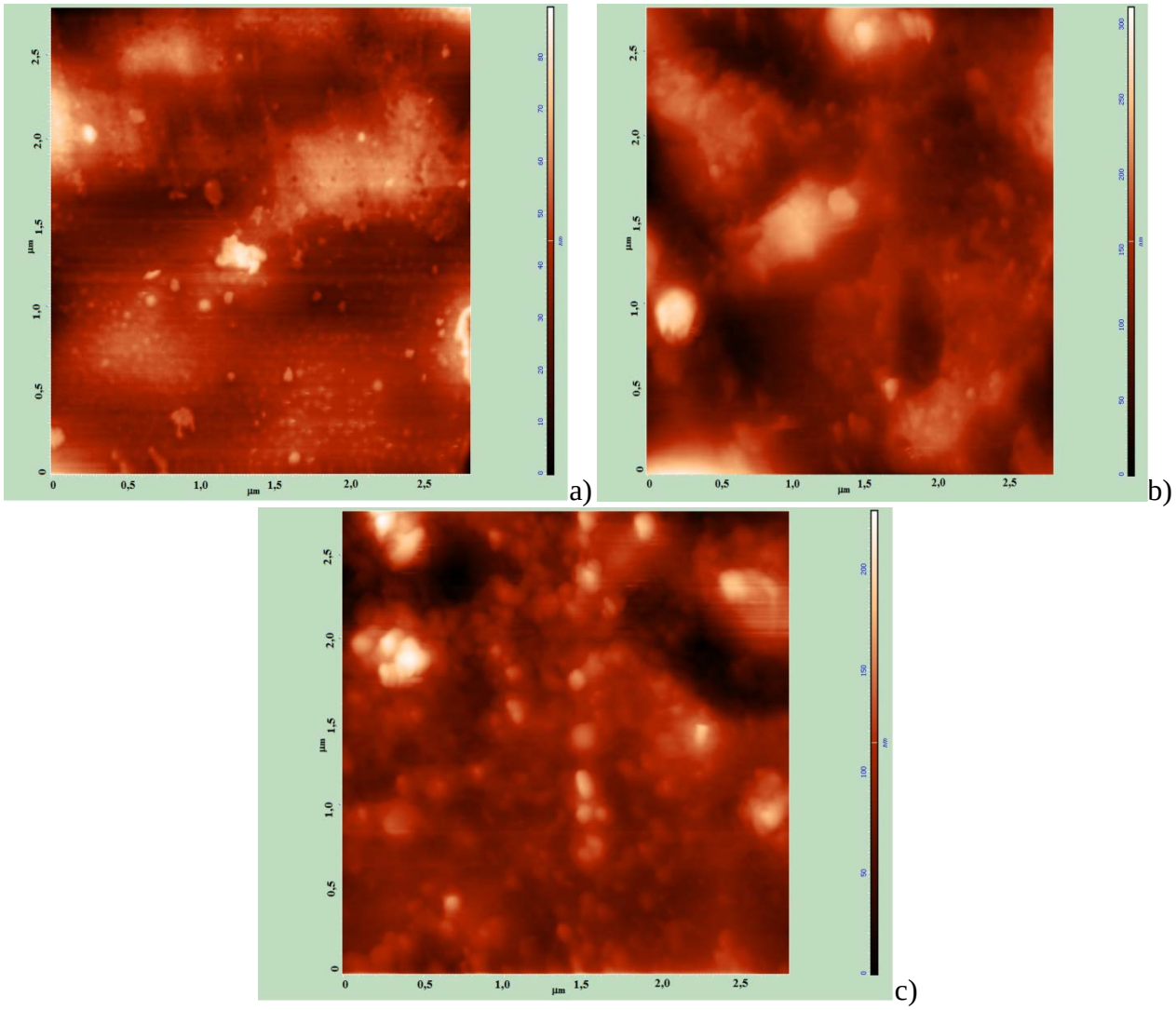

Fig.3.AFM 2D images of polymer nanocomposites based on PVC+ZnS: a) PVC+3% ZnS; b) PVC+5% ZnS; c) PVC+10% ZnS.

Figure 3 shows the AFM images of polymer nanocomposites based on PVC+ZnS as a function of the concentration of ZnS nanoparticles. As can be seen from the Figure 3 with the introduction of nanosizedZnS particles into the polymeric matrix of PVC, the supramolecular structure of the nanocomposites changes. As the content of nanoparticles increases, the supramolecular structure and structural elements of the nanocomposite surface change. So the average roughness for the PVC+3% ZnSnanocomposite is 5-15 nm, for PVC+5% ZnS- 20-60 nm, PVC+10% ZnS-20-100 nm (Fig. 4)[4-7].

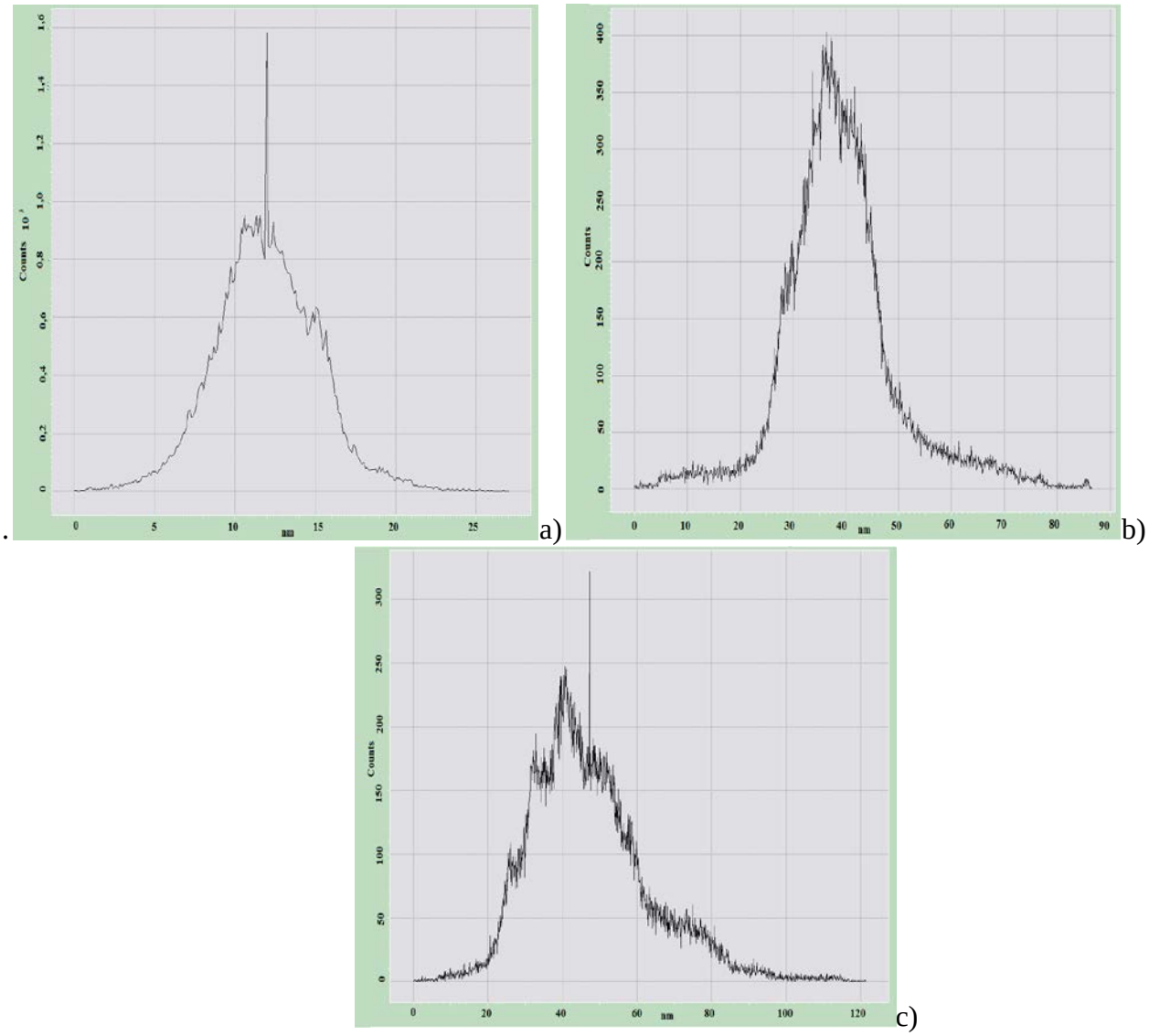

a) b) c)

Fig.4. Histogram of the roughness of polymer nanocomposites based on PVC+ZnS: a)PVC+3%ZnS; b) PVC+5%ZnS; c) PVC+10%ZnS.

In Fig. 5.the absorption spectra (a) and the graph of the calculation of the band gap (b) for a nanocomposite based on PVC+ZnS depending on the concentration of ZnS nanoparticles are shown. From the extrapolation of the absorption spectra, the width of the band gap of nanocomposites based on PVC+ZnS was calculated as a function of the concentration of ZnS nanoparticles (Table 1). The width of the band gap of nanocomposites was calculated by the following formula:

$$\alpha = A\left(h\nu - E_g\right)^n / h\nu \text{(e.g.)} \quad (1)$$

where, α is absorption coefficient, A-isconstant, hν-is photon energy, E_g is the width of the forbidden band.

As can be seen, from Table 1, as the concentration of ZnS nanoparticles increases, the width of the band gap of nanocomposites decreases. The decrease in the width of the forbidden band as a function of the concentration of ZnS nanoparticles is explained by the increase of concentration and agglomeration of nanoparticles in the polymer matrix of PVC, depending on the content of ZnS nanoparticles[8-9].

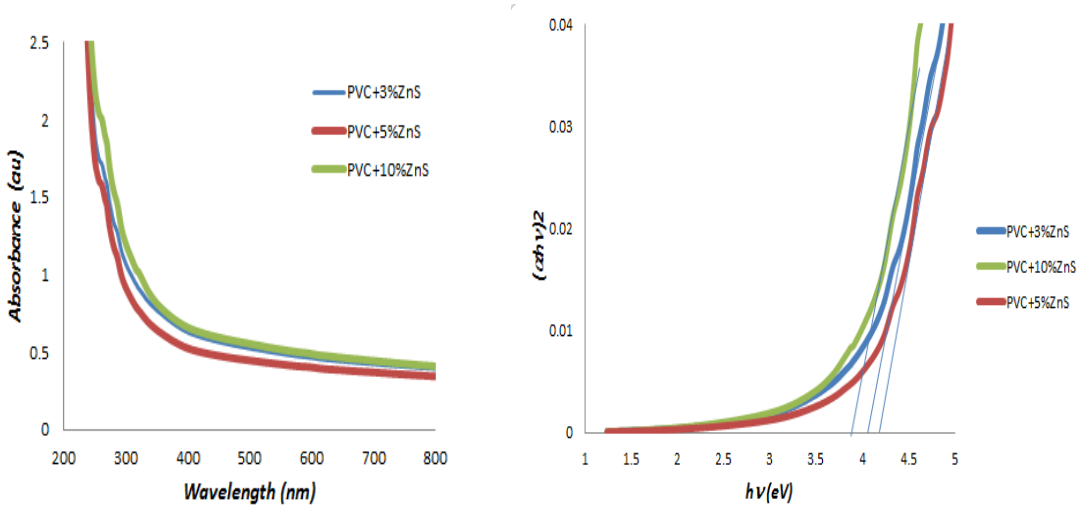

Fig.5.Absorption spectra and graph of the calculation of the band gap for PVC+ZnS as a function of the concentration of nanoparticles ZnS.

Table 1.

Sample	Width of the forbidden band (eV)
BulkZnS	3,6
PVC+3%ZnS	4,2
PVC+5%ZnS	4
PVC+10%ZnS	3,95

Figure 6 shows the photoluminescence spectra of nanocomposites based on PVC+ZnS as a function of the concentration of ZnS nanoparticles. Photoluminescence spectra were obtained by excitation of samples with a wavelength of 260 nm. It was established that the intensity of photoluminescence decreases with increasing concentration of nanoparticles. The decrease in the intensity of photoluminescence with an increase in the concentration of nanoparticles is explained by the decrease in the specific surface due to an increase in the size of the particles. Figure 7 shows excitation and emission spectra for a nanocomposite based on PVC+ZnS. It can be seen that the excitation and emission spectra are mirror images of each other, which is a proof that the peak at 356 nm, 375 nm, 528 nm, 540 nm, 562 nm, 593 nm are photoluminescent peaks belonging to ZnS nanoparticles[10-21].

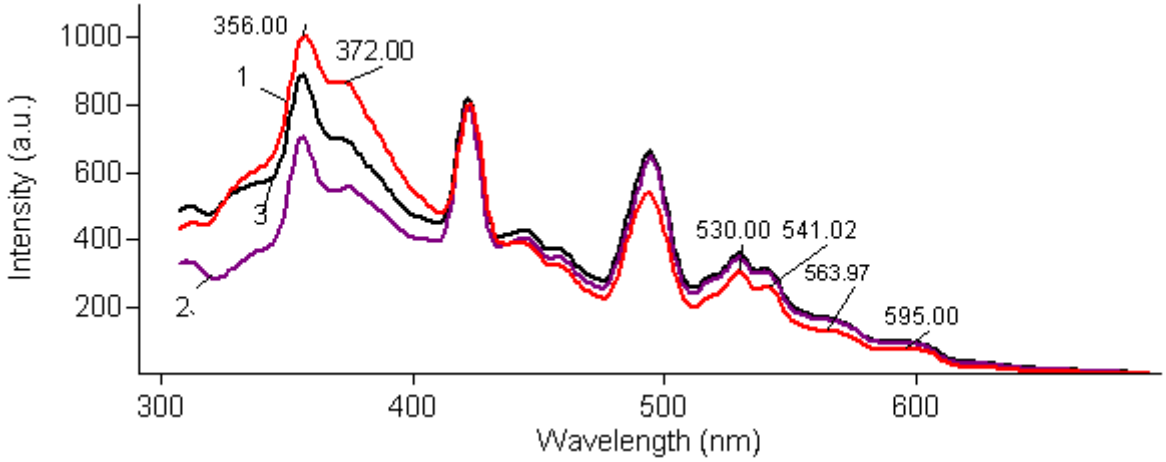

Fig.6.Luminescence spectra of PVC+ZnS based polymer nanocomposites: 1.PVC+3%ZnS; 2. PVC+5%ZnS; 3. PVC+10%ZnS.

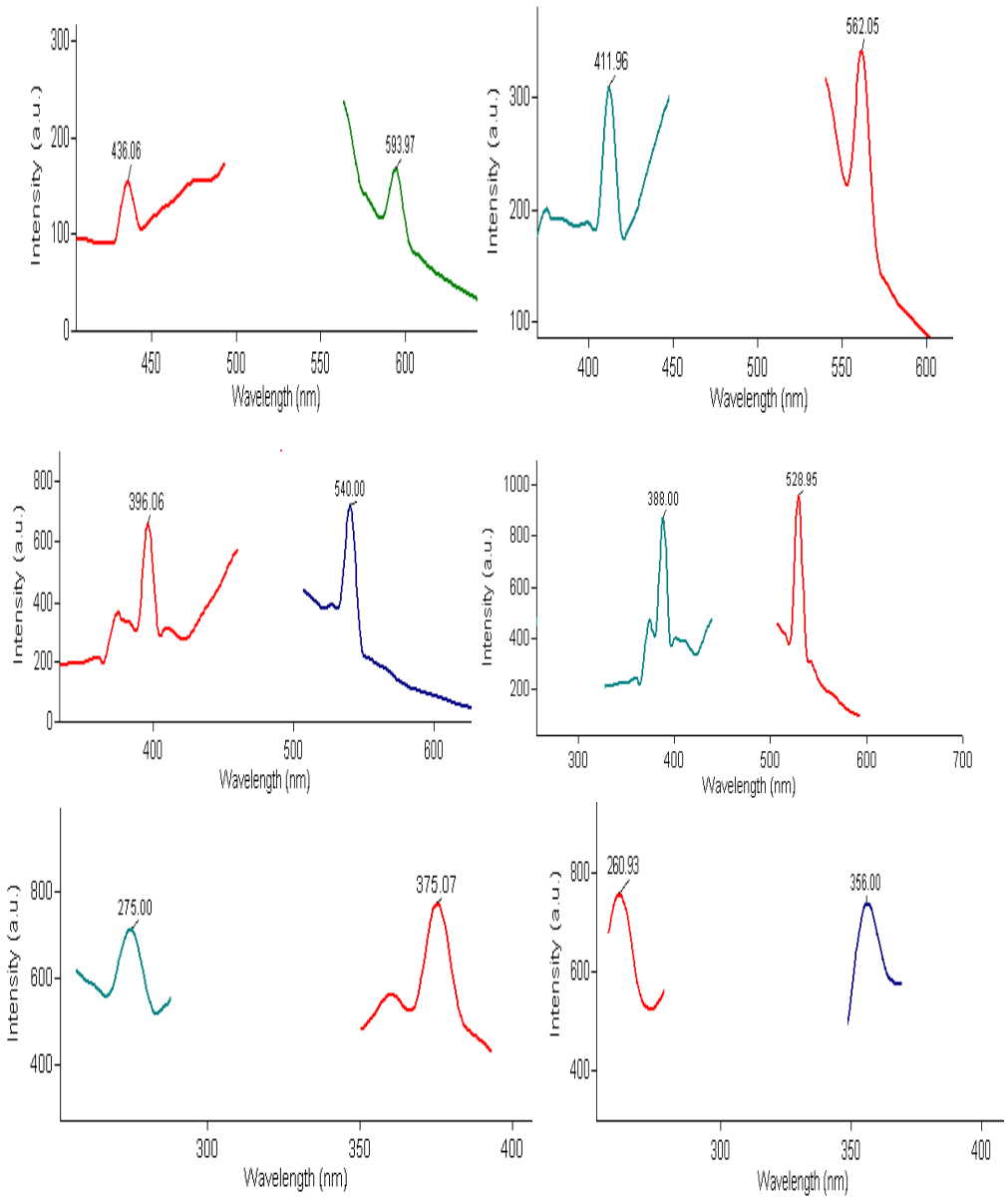

Fig.7.Excitation and emission spectra for PVC+ZnS based nanocomposites.

Photoluminescent properties of PVC+ZnS based polymer nanocomposites have been investigated depending on the thermal annealing process.Figure 8 shows photoluminescence spectra of PVC+ZnS based polymer nanocomposites depending on the thermal annealing process. It has been determined that as the temperature of thermal treatment of nanocomposites increases till 120^0C, the intensity of photoluminescent also increases.This is explained by the complete release of the THF solvent from the PVC matrix.

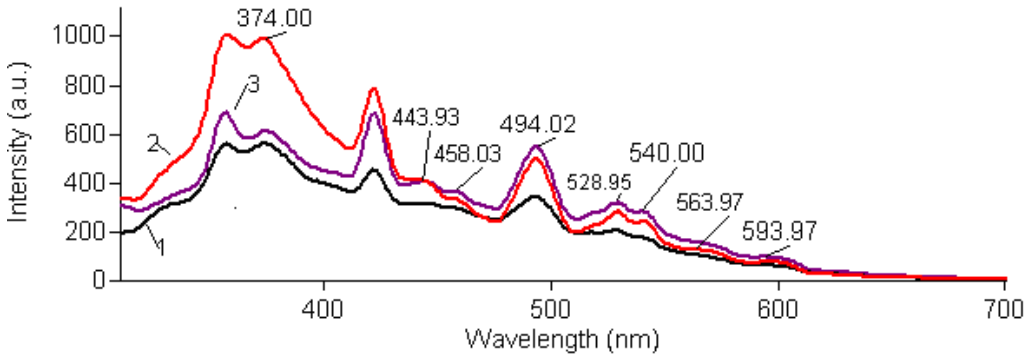

Fig.8.Photoluminescence spectra of PVC+ZnS based nanocomposites depending on the thermal annealing: 1. 80^0C;2.100^0C; 3.120^0C.

4. Conclusion

In this paper, polymeric nanocomposites based on polyvinyl chloride and nanoparticles of zinc sulphide were obtained and investigated. SEM analysis showed that the average size of nanoparticles based on PVC+ZnS is 3-5 nm.From UV spectra of nanocomposites by extrapolation method the width of the forbidden band for polymer nanocomposites was determined. It was determined that the bandgap for nanocomposites based on PVC+3% ZnS is 4.2 eV; for PVC+5% PbS-4.0 eV; for PVC+10% ZnS-3.95 eV. The photoluminescence properties of nanocomposites based on PVC+ZnS were studied. It has been found that peaks at 356 nm, 375 nm, 528 nm, 540 nm, 562 nm, 593 nm on the photoluminescence spectrum of nanocomposites are luminescent peaks belonging to ZnS nanoparticles. The influence of thermal annealing on the optical properties of nanocomposites based on PVC+ZnS were also studied and it was shown that with an increase in the processing temperature of nanocomposites up to 120^0C, the photoluminescence intensity increases. The increase in the intensity of the photoluminescence with increasing thermal annealing temperature is explained by the complete removal of the solvent from the volume of the polymer and thereby improving the photoluminescence efficiency of the nanocomposites.

References

[1] Pomogailo A.D., Rosenberg.A.,Uflyand I.E. Publisher Chemistry, 672 (200)
[2] A.M.Magerramov, M.A.Ramazanov, F.V.Hajiyeva J. Chalcogenide Letters 11(4), 175 (2014)
[3] A.M.Maharramov, M.A.Ramazanov, F.V.Hajiyeva Journal Chalcogenide Letters, 13(1), 35(2016)
[4] A.M.Maharramov, M.A.Ramazanov, J.R.Sultanova, F.V.Hajiyeva, U.A.Hasanova Journal of Ovonic Research 12(4), 193(2016)
[5] A.M.Maharramov, M.A.Ramazanov, S.Q.Nuriyeva, U.A.Hasanova, F.V.Hajiyeva Chalcogenide Letters 13(7), 317(2016)
[6] A.M.Maharramov, M.A.Ramazanov, A.B.Ahmadova, F.V.Hajiyeva, U.A.Hasanova Digest Journal of Nanomaterials and Biostructures 11(2), 365 (2016)
[7] Mahammadali Ahmad Ramazanov, Abel MammadaliMaharramov, Flora VidadiHajiyeva, Feyza Kıraç, Olgun Güven RevistaRomână de Materiale/Romanian Journal of Materials 46 (3), 375(2016)
[8] Novruzova A.A, Ramazanov M.A, Chianese A., Hajiyeva F.V, Maharramov A.M, Hasanova U.A J.Chemical Engineering Transactions 60, 61(2017)
[9] Ramazanov M.A, Maharramov A.M, Chianese A, Novruzova A.A, Maharramova G.Y Journal of Ovonic Research 14 (2), 113 (2018)
[10] Fang D.F., Zhang Z.M., Wang Z.P. and Ding Z.J. Physics Procedia 32 920 (2012)
[11] AnujaDatta, Subhendu K. Panda and Subhadra Chaudhuri J. Phys. Chem. C 111 (46), 17260 (2007)
[12] Hitanshu Kumar, Manoj Kumar, P. B. Barman, Ragini Raj Singh J.Appl. Phys. A, 117(3), 1249 (2014) Published on-line.
[13] Limin Qi, Jiming Ma, Humin Cheng, Zhenguo Zhao J. Colloids and Surfaces A Physicochemical and Engineering Aspects, 111 (3), 195 (1996)
[14] Nida Qutub, Bilal Masood Pirzada, Khalid Umar, OwaisMehraj, M. Muneer, Suhail Sabir Physica E: Low-dimensional Systems and Nanostructures 74, 74(2015)
[15] Le Wang, Hongwei Wei, Yingju Fan, Xinzheng Liu, Jinhua Zhan Nanoscale Res Lett, 4, 558(2009)
[16] Shih-Yuan Lu,Mei-Ling Wu and Hsin-Lung Chen J. Appl. Phys. 93(9), 5789(2003)
[17] Yinan Zhang J.High performance polymers 28(2), 198(2015)
[18] Raju Kumar Chandrakar , V.K.Chandra, B.P.Chandra Superlattices and Microstructures 84, 132 (2015),
[19] MagerramovA.M., M.A.Ramazanov, A.Kh.Mustafaeva J.Surface Engineering and Applied Electrochemistry 46 (3), 281 (2010)
[20] Hongan Xi, Xuefeng Qian, Jie Yin, Lijuan Bian, Rong He, Zikang Zhu J. Materials letter 57(18), 2657 (2003)
[21] Anil Kumar, Anshuman Jakhmola Journal of Colloid and Interface Science 297 (2), 607 (2006)

CHEMICAL AND PHYSICAL CONDITIONS OF CRYSTALLIZATION OF IRON-TITAN OXIDE MINERALS IN THE INSTANCE OF LOWER AND UPPER CRETACEOUS MAGMATIC COMPLEXES OF THE LESSER CAUCASUS

M.N.MAMMADOV[*], G.C.BABAYEVA[**], K.F.ABBASOV. [**], S.H.CAFAROV[**]

[*]*Baku State University, Geology and Historical Geology Chair*
[**]*Azerbaijan National Academy of Sciences,Institute of Geology and Geophysics, sector of Mineralogy and Crystallography*
ceferovsoltan@gmail.com

Abstract In the presented article, were studied a crystallization sequence and temperature as well lithostatic and fluidal pressures of iron-titan oxide minerals that have been crystallized in the natural conditions. The study resulted in that, the differentiates of a polyphasic Gadabay intrusion located in Azerbaijan have been crystallized in temperature 720 -820 ^{o}C and in the depth of 1.5–12 km. Calculated and experimental Curie points of these differentiates vary between 450–560 ^{o}C. However, mineral equilibriums magnetite-ulvospinel (Fe_3O_4 –Fe_2TiO_4)and ilmenite-hematite ($FeTiO_3$-Fe_2O_3) which are one of the porphyry parageneses of upper Cretaceous volcanic rocks which occur in the northern-east slopes of the Lesser Caucasus have been crystallizedin temperature 800 -1250 ^{o}C and in the depth of 6–21 km.The Curie point of lasts varies between 150– 560 ^{o}C.

Analysis of the results yields that ulvospinel and titan bearing magnetite crystallized in relatively reducing conditions has been crystallized in high temperature (1050–1100 ^{o}C) and in depth of 18-21 km. Lighter fractions of these rocks but have been crystallized in upper horizons (1.5-3.2 km).

1. Introduction

It's a known fact that, crystallic phase participated in the crystallization of the natural magmatic melts, keeps an information about thermobaric and geodynamic conditions that control the related process. In this respect, iron-titan oxide minerals are more sensitive. The change of ferrous oxide to ferric oxide in the oxidizing condition causes magnetite crystallizes before silicate minerals. Of course in crustal conditions happens early crystallization of it. However, in the conditions of loss of volatiles it crystallizes after silicate minerals. İn the lower lythostatic pressure means in the upper horizons of the crust, magnetite is poor in titan and becomes a maghemite, magnetite with cation deficiency. This diversity feels both in theoretical and in experimental Curie points. Pecherskiy (1975), Kawai (1956) used this feature of iron-titan oxide minerals to determine depth of crystallization.So, the analysis of these features of iron-titan oxide minerals can be used in the study of the crystallization of the silicate systems.

Aforementioned silicate system has been crystallized in the upper horizons of the crust. However, upper Cretaceous silicate systems of the Lesser Caucasus first have been crystallized in the intermediate magma chambers of various depths, depending on the magma bearing capacity of the crust, then they have been crystallized in the surface. İn the deep chambers ulvospinel bearing magnetite has been crystallized in the high temperature and pressure. In the surface conditions has been crystallized magnetite poor in titan and wit cation deficiency.

2. Methods

Iron-titan oxide minerals have been studied with the contribution of bulk chemical, X-ray spectral, X-ray diffractometric sand thermomagnetic analyses.

Calculation of the theoretical Curie points has been realized with availible methods (Nagata 1965, Pecherskiy (1975). Crystallization temperature and oxygen fugacity have been calculated with methods of Buddington&Lindsley (1964), Lindsley et.al (1983), Stormer J.C. (1983). And in the determination of crystallization depth the methods of Pecherskiy (1975), Kawai (1956) and Zubkov et.al. (2015) have been used.

3. Results and discussion

Iron-titan oxide minerals are widely spread in nature and they have crystallized in different conditions. Hence, the investigation of their crystallization conditions whether synthetic or natural silicate systems, is very important in the solving of several geological and paleomagnetic problems.

Appropriate areas regarding to this purpose can be upper Jurassic –lower Cretaceous complexes located in the Shamkir horst – uplift and upper Cretaceous complexes located in the Qazakh, Agdjakand, Agdara, Azykh and etc. troughs of the Lesser Caucasus.

An object for study among upper Jurassic – lower Cretaceous complex can be Gadabay intrusion which located in the Shamkir horst – uplift. Iron-titan oxide minerals occur widely inmultiphase Gadabayintrusion, which is located in Gadabay administrative region. These minerals have crystallized in the different depths in the distinguished thermobaric conditions. Whereby, magnetite-hematite buffer has controlled the crystallization process. During the stages of crystallization of the intrusion, typified differentiates of the intrusion have formed by the fractionation. Sometimes the main differentiates have been cut by the rocks which are formed from the residual magmatic melts. They consist of sills of little thickness, dykes and rarely stocks in a small diameter[6].

Gadabay intrusion begins in 1.5 km away to thesouth-east, of the conjunction of the Gadabay and the Shamkir rivers. It then goes along for 12 km in the north-western direction until the Arikhdam village. The width of intrusion changes irregularly along the stretching (1.5-6 km)[6]. The central part of the intrusion includes absolute crystalline rocks in dark-grey and dark black colors. The color of the rocks change from dark black to dark grey and to grey toward lateral parts of the intrusion? The amount of clino- and orto-pyroxenes decreases, however the amount of amphiboles with metallic blink and plagioclases in light grey color increases gradually in the same direction as well[2].The temperature, the litho baric and fugacity of oxygen controlling the crystalliztion were calculated by the methods presenting in the literature[1] (Buddington, Lindsley 1964, Lindlsey, Spenser 1982, Gendshaft et al. 1999, Zubov et al. 2015). The XRD analyses have been done in the laboratory of the Institute of Geology and Geophysics of ANAS. Thermomagnetic (Curie point, magnetic susceptibility and microprobe) analyses have been done in the Geology Institute of Ministry of Geology of Russia situated in Saint-Petersburg.

The differentiations of a gabbroid phase (first phase) of Gadabay intrusion have been crystallized in the depth of 2.3-3 km below surface in the intrusive chamber. The concentration of ulvospinel molecule in the moderately titanic magnetite changes between 6.5-11.4 %. The calculated and experimental values of Curie temperature are 510-533 C^o. Hence, it can be considered that, the higher content of titan oxide in norite and gabbro-norite crystallized by gravitation than in other differentiations of the intrusion due to their crystallization in the higher thermobaric conditions[2]. Accordingly the oxygen fugacity of the crystallization is lower (lgf_{O_2}=12-14). Beside, ilmenite and moderately titanic magnetite have crystallized in eutectic with clino- and orto-pyroxen. In this phase of the intrusion sulfides of Co (cobaltite) and Ni (millerite) have been crystallized.

In quarts diorites-the second phase of the intrusion and in its differentiations due to increase of silica and decrease of magnesia and iron oxides, the amount of titanoxide was decreased and the amount of ferric iron oxide was increased in iron-titan oxide minerals. In the turn it has caused to crystallize characterized titanic magnetite[3]. This crystallization process had relatively more oxidizing environment. The controlling oxygen fugacity of the system have been increased sufficiently ($lgf_{O_2}=10^6$-10^8). As a result part of the ferrous iron oxide have been replaced by the ferric iron in the titanic magnetites. Consequently,maghemite poor in titan content and with cation deficiency has crystallized.

$$(Fe_8^{+3}[Fe_{13.33}^{+3}\square_{2.67}]O_{32})$$

As is explicit from the formula above the 2.67 is vacation of deficient cation.

The experimental and the calculated values of Curie points of this phase are in the range of 570-590 C^o. Crystallization have gone under pressure of 1.5-3 kbar. The depth of crystallization was 3-6 km.

In the course of an evolution on one hand by the influence of the hybridism, on the other hand by the influence of the LIL elements (K, Rb, Ba, Sr and etc.) two distinguished differentiates have crystallized from the magma of the quartz diorites. The first one of them is diorites with biotite $(K(MgFeAl)_3(SiAl)_4O_{10}(OH)_2$ and hornblende $(NaCa_3(MgFe)_4(FeAl)(OH)_2$, whereas the second one of them are monzodiorites, monzonites, syenites which are the alkali element carriers. The concentration of K and elements relative to it increases in the second group of rocks ($KAlSi_3O_8$, $K(Mg,Fe^{+2})_3[Si_3AlO_{10}](OHF)_2$) and The litho static pressure of crystallization relatively increases (5.2-5.6 km) causing the temperature also to increase , however the oxygen fugacity decreases ($lgf_{O_2}=10^6$-10^8).

The analysis of the achieved results shows that, weak oxidizing conditions have controlled the process while the differentiates of the gabbroid phase were forming. That is why a hydrogen sulfide solution have been oxidized partly and weakly[4]. Therefore, some Ni and Co sulfide mineralization occurs in connection with this phase. However, sulfide mineralization of Fe is related to quartz diorite phase.

Last differentiates of quartz diorite phase were a source of mineralization of chalcopyrite and pyrite containing gold. In later stages, sphalerite mineralization has joined the process.

Finally, with the increasing of the concentration of incoherent elements in the residual magma, a barite-polymetallic mineralization containing gold has begun ($BaSO_4$, $CuFeS_2$, ZnS, PbS).

Thus, the physicochemical behavior of the iron-titan oxide minerals in the discussed system can be used as an indicator in the interpretation of the crystallization conditions and can have a dramatic role in the determination of the direction of the gold mineralization in Gadabay ore region.

For upper Cretaceous complexes, on the base of calculated and experimental Curie points and physical-chemical parameters (t-temperature, f_{O_2}- oxygen fugacity, H-depth) and determined variation in the compositions as well, it's possible to say that the crystallization of the iron-titan oxide minerals went in the intermediate magma chambers of various depths.

Wherein, in upper Coniacian and lower Santonian ages the progressive flexure continued whereby, low-differentiated portions of olivine-basalt melt which from high titanic magnetite had been crystallized, has been located in deeper intermediate magma chambers.

In the boundary of upper Santonian and lower Campanian within the Gazakh trough the activity of the magma bearing channels significantly weakened. Whereby, within the trough have been formed subsurface intermediate chambers which the spatial connection of volcanic centers composed of rhyodacite, perlite, andesite and dacite can be the evidence.

Unlike the Gazakh trough, within the Agdjakand and Agdara troughs the compression process acted more intensive, that caused the thermal interaction between hot basaltic melt and upper layered arkosic sandstones. As a result, these sandstones melted and the palingenetic rhyodacite and dacite have been generated.

Within the Khojavend and Azykh troughs in the lower Santonian age in the flexure conditions has been formed low differentiated trachibasalt-trachidolerite complex. In the composition of differentiates of these complex occurs moderately titanic titanomagnetite. In the upper Santonian age has been crystallized differentiates of a tephrite-teshenite complex in the relatively more oxidizing condition. Hereby, due to the delay of plagioclase crystallization moderately titanic magnetite composed the tephrites has enriched in aluminum oxide. Inside the intrusive teshenites has been crystallized ulvospinel bearing titanomagnetite. In the Gochaz trough inside the basalts and andesibasalts moderately titanic magnetite has been crystallized before pyroxene phenocrysts. Inside the rocks of subalkali series relatively high titanic magnetite has been crystallized simultaneously with clinopyroxene.

Conclusion

As a result of interpretation of complex physical-chemical and mineralogical analyses, has been concluded that in the upper Jurassic-lower Cretaceous complex magnetite has been crystallized in the upper horizons before silicates in oxidizing conditions.

In the upper Cretaceous volcanik rocks the crystallization has run in two stages.In the first stage iron titan oxide minerals and silicate minerals which were in equilibrium with them have been crystallized in high thermobaric and reducing condition with accompaniment of volatiles in the depth of 16-21 km. Residual melt has been crystallized in the second stage, in surface or in oxidizing conditions

Reference

[1] Buddington, A F and Lindsley, D H,. Iron-titanium oxide minerals and synthetic equivalents. J. Petrol, **5**: 310-357 (1964)

[2] Lindsley, D.H., and Spencer, "K.J. Fe-Ti oxide geothermometry Reducing analyses of coexisting Ti-magnetite (Mt) and ilmenite" (Ilm). EOS. 63. 471 (1982)

[3] Efendiyev Q.X. "Hydrothermal ore complex of the northern-east part of the Lesser Caucasus", NA of Azerb. SSR,Baku:1957, 300 pp.

[4] AliyevV.I. "Pyriteoreformation of The Lesser Caucasus" Baku: 50pp, 1976

[5] Carmichael, I.S., NichollsJ.Iron-titanium oxides and oxygen fugacities in volcanic rocks. *Journal of Geophys. Res*., **72**, 4665-4687 (1967)

[6] Geology of Azerbaijan. "Minerals". T. VI, 631 pp.(2003)..

[7] ZubovA.Q., BazanovaL.I., AnanyevV.V., OvsyannikovA.A., JidkovQ.V. "Aboutapplicationof titanomagnetite method to determination of magmatic chamber depth in the instance of some camchatka volcanos", Materials of annual conference dedicated to volcanologist Day. 2015, pp 138-147

[8] GenshaftU.S., ChelmovichV.A., QapeyevA.K., SolodovnikovQ.M. "ImportanceFe-TioxidemineralsinthesciencesoftheEarth", NewsDGGGMRAS, 1999 №1(7), p.3-12.

Longitudinal Nernst-Ettingshauzen effect in superlattices for acoustic phonons scattering

S.R.FIGAROVA, S.K.ALIAHMEDLI

Baku State University, Department of Physics, Solid States Physics Chair, Azerbaijan, AZ1148, Baku, 23 Z.Khalilov st.
figarov@bsu.edu.az

Abstract: In this work the anisotropy of longitudinal Nernst-Ettingshausen coefficient in superlattices for electron-phonon scattering is considered. It is shown that the longitudinal Nernst-Ettingshausen coefficient changes its sign depending on the magnetic field direction.

Key words: *superlattice, Nernst-Ettingshauzen coefficient, electron-phonon scattering.*

1. Introduction

Magnetothermoelectric effects are particular sensitive to the anisotropy of conduction electron dispersion law, relaxation time and effective mass; therefore, it is very interesting to study these effects in conductors with the cosine dispersion law. Phonon scattering is the main scattering mechanism at temperature more than 70*K* in the superlattices such as *GaAs*/*AlGaAs* [1]. In superlattices, depending on the magnetic field orientation and temperature gradient, and also electron gas dimensionality, unique thermomagnetic effects (for instance, oscillations and dependence on the superlattice period of kinetic coefficients) [2-5]. In this paper, the longitudinal Nernst-Ettingshausen effect is studied in superlattices in the case of charge carrier scattering by acoustic phonons for magnetic field applied perpendicular and parallel to the plane of the layer. Expressions for longitudinal Nernst-Ettingshausen coefficient for quasi-two-dimensional and quasi-three-dimensional degenerated electron gas are obtained. It has been shown that the longitudinal Nernst-Ettingshausen coefficient changes its sign depending on the magnetic field direction.

2. Longitudinal Nernst-Ettingshausen coefficient in superlattices

Consider an electron gas with the cosine dispersion law:

$$\varepsilon(k)=\frac{\hbar^2 k_\perp^2}{2m_\perp}+\varepsilon_0\left[1-\cos(ak_z)\right], \tag{1}$$

here $k_\perp^2=k_x^2+k_y^2$, $k_\perp$ and k_z are longitudinal and transverse components of the wave vector, ε_0 is the half-width of miniband, a is the superlattice constant.

To calculate galvano- and thermomagnetic tensors, one uses an implicit relaxation time formula, that for acoustic phonons scattering is equal to [6]:

$$\frac{1}{\tau}=Ag(\varepsilon), \tag{2}$$

where

$$g(\varepsilon)=m_\perp Z(\varepsilon)/\pi^2\hbar^2 a$$

is the density of states, $A=\pi E_1^2 k_0 T/\hbar\rho\upsilon_0^2$. For degenerate electron gas, $Z(\varepsilon_F)=Z_0$, Z_0 is determined by the topology of the Fermi surface, where ε_F is the Fermi energy. Now using formulas (1) and (2) in the solution of the Boltzmann kinetic equation in the semiclassical approximation for superlattices [7], one can obtain analytical expressions for the Nernst-Ettingshausen coefficient in an arbitrary magnetic field.

Longitudinal Nernst-Ettingshausen coefficient in the perpendicular magnetic field is determined from conditions: $j_x=j_y=0$ and $\nabla T_y=0$ as follows:

$$\alpha(B)=-\frac{k_0}{e}\frac{\pi^2}{3}\frac{k_0 T}{\varepsilon_0}\frac{Z_0}{\sin Z_0-Z_0\cos Z_0}. \tag{3}$$

It is seen from formula (3) that longitudinal Nernst-Ettingshausen coefficient is determined by the degree of miniband filling Z_0 and is independent of the magnetic field strength in the perpendicular magnetic field. For quasi-two-dimensional electron gas $\varepsilon_F>2\varepsilon_0$, $Z_0=\pi$, we have:

$$\alpha(B) = -\frac{k_0}{e}\frac{\pi^2}{3}\frac{k_0 T}{\varepsilon_0}. \quad (4)$$

In the parallel magnetic field $\alpha(B)$ is given by:

$$\alpha(B) = \frac{k_0}{e}\frac{\pi^2}{3}\frac{k_0 T}{\varepsilon_0}\int_0^{Z_0}\frac{\sin^2 ZdZ}{Y}\int_0^{Z_0}\frac{dZ}{Y}\times$$

$$\times\left(\int_0^{Z_0}\frac{XdZ}{\cdot Y}\cdot\int_0^{Z_0}\frac{\sin^2 ZdZ}{Y}+\frac{(\Omega\tau_0)^2}{Z_0^2}\int_0^{Z_0}\frac{X\cos ZdZ}{Y}\int_0^{Z_0}\frac{\sin^2 ZdZ}{Y}\right)^{-1}, \quad (5)$$

where $\Omega = eB/(m_\perp m_{II0})^{1/2}$, $m_{II0} = \hbar^2/\varepsilon_0 a^2$.

It is seen from formula (5) that longitudinal Nernst-Ettingshausen coefficient is non-monotonic with the degree of miniband filling. Besides, it follows that longitudinal Nernst-Ettingshausen coefficient changes its sign in the parallel magnetic field and takes positive values.

In the weak magnetic field $\Omega\tau_0 << 1$, from (5) we get:

$$\alpha(B) = \frac{k_0}{e}\frac{\pi^2}{3}\frac{k_0 T}{\varepsilon_0}\frac{Z_0}{\sin Z_0 - Z_0\cos Z_0}\left[1-(\Omega\tau_0)^2\frac{\sin Z_0}{Z_0^3}\right]. \quad (6)$$

From formula (6), it is clear that in longitudinal magnetic field longitudinal Nernst-Ettingshausen coefficient changes its sign. In the strong magnetic field $\Omega\tau_0 >> 1$ longitudinal Nernst-Ettingshausen coefficient is:

$$\alpha(B) = \frac{k_0}{e}\frac{\pi^2}{3}\frac{k_0 T}{\varepsilon_0}\frac{Z_0^2}{B^2 u_{\perp 0} u_{II0}}\frac{\ln\left|tg(Z_0/2+\pi/4)\right|}{\sin Z_0 - Z_0\cos Z_0}, \quad (7)$$

where u is the charge carrier mobility.

3. Conclusion

Longitudinal Nernst-Ettingshausen coefficient equals zero in the case of the quasi-two-dimensional electron gas. To summarize, we consider anisotropy of longitudinal Nernst-Ettingshausen coefficient in superlattices in the case of scattering of conduction electrons by acoustic phonons depending on the magnetic field direction. In the longitudinal magnetic field, longitudinal Nernst-Ettingshausen coefficient changes its sign. Change in the Nernst-Ettingshausen coefficient sign depending on the magnetic field direction is attributed to the effective mass sign.

References

[1] Ando T., Fowler A., Stern F., Electronic properties of two-dimensional systems. Reviews of Modern Physics. 416 p. (1982).
[2] Thomas P., Zvyagin I.P., Superlattices and Microstructures **10**, p.119-120 (1991).
[3] Nguyen Ouock Khanh,Vo Van Tai., Superlattices and Microstructures **100**, p.792-798 (2016).
[4] Bian Z., Zebarjadi M., Singh R., Ezzahri Y., Shakouri A., Zeng G., Bahk J-H., Bowers J. E., Zide J.M.O., Gossard A., C. Physical Review B **76,** p.205311 (5pages) (2007).
[5] Figarova S.R., Huseynov H.I., Figarov V.R., Superlattices and Microstructures **117**, p.469-475 (2018).
[6] Askerov B.M., Kuliev B.I., Figarova S.R., Gadirova I.R., Journal of Physics: Condensed Matter **7**, p.843- 848 (1995).
[7] Figarova S.R., Figarov V.R., EPL (Europhysics Letters) **89**, p. 37004 (5pages) (2010).

Seebeck effect in quantum well of complex shape with phonon scattering

S.R.FIGAROVA, M.M.MAHMUDOV, G.A.BAKHSHIYEVA

Baku State University, Department of Physics, Solid States Physics Chair, Azerbaijan, AZ1148, Baku, 23 Z.Khalilov st.
mmm@bsu.edu.az

***Abstract**:* In this paper Seebeck effect in quantum well of complex shape for scattering by optical phonons is studied. The dependence of the degenerate electron gas thermopower on the parameters of the quantum well is obtained. It is shown that thermopower increases with decreasing of the thickness of the quantum well. The dependence of the thermopower on the well thickness is connected to the quantum effect - the restrict of the electron motion in a quantum well.

***Keywords**: thermopower, two-dimensional electron gas, the quantum well of complicated form, phonon scattering.*

1. Introduction

Thermoelectric phenomena provide valuable information on electron transport processes. Considerable interest in the investigate of the thermoelectric properties of two-dimensional systems increased after the appearance of works in which the possibility of an increase in the thermoelectric quality factor was theoretically and experimentally demonstrated, owing to an increase in the density of states in low-dimensional systems [1]. In recent years, thermoelectric phenomena have been intensively studied in quantum wells of various shapes [2, 3]. In this paper we study the thermoelectric power of a quantum well of a complex shape for scattering by optical phonons.

2. Thermopower of the degenerate two-dimensional electron gas in a quantum well

We consider the energy spectrum of a two-dimensional electron gas in a quantum well with $U = U_0 / \cos^2(z/a)$ potential profile, which has the form:

$$\varepsilon_n = \varepsilon_0 \left(1 + 2n + \sqrt{1 + \frac{U_0}{\varepsilon_0}} \right)^2 , \tag{1}$$

here $\varepsilon_0 = \hbar^2 \pi^2 / 8ma^2$, a is the quantum well width, U_0 - is the potential energy minimum, n - is the quantum number. For the energy spectrum (1), the density state of the two-dimensional electron gas has the form:

$$g(\varepsilon) = \frac{m}{\pi \hbar^2 a} \sum_n \Theta(\varepsilon - \varepsilon_n) , \tag{2}$$

where $\Theta(\varepsilon - \varepsilon_n)$ - is the Heaviside function.

In the stationary case, from the condition $j_{dif} + j_E = 0$ for the thermopower we have

$$\alpha = \frac{\beta}{\sigma} , \tag{3}$$

where for two-dimensional electron gas conductivity σ and thermoelectric coefficient β are equal:

$$\beta_{xx} = \frac{-2e}{T\hbar^2 a} \sum_n \int_{\varepsilon_n}^{\infty} \Theta(\varepsilon - \varepsilon_n)(\varepsilon - \varepsilon_n)(\varepsilon - \mu)\tau(\varepsilon) \left(-\frac{\partial f}{\partial \varepsilon} \right) d\varepsilon , \tag{4}$$

$$\sigma_{xx} = \frac{e^2}{\pi \hbar^2 a} \sum_n \int_{\varepsilon_n}^{\infty} \Theta(\varepsilon - \varepsilon_n)(\varepsilon - \varepsilon_n)\tau(\varepsilon) \left(-\frac{\partial f}{\partial \varepsilon} \right) d\varepsilon , \tag{5}$$

here μ is chemical potential, $\tau(\varepsilon)$ is the relaxation time, $f(\varepsilon)$ - the Fermi-Dirac distribution function, e is the electron charge, T is the absolute temperature.

Taking (4) and (5) into (3), we obtain for the thermopower:

$$\alpha = -\frac{2}{eT\pi}\frac{\sum_n \int_{\varepsilon_n}^{\infty} \Theta(\varepsilon-\varepsilon_n)(\varepsilon-\varepsilon_n)(\varepsilon-\mu)\tau(\varepsilon)\left(-\frac{\partial f}{\partial \varepsilon}\right)d\varepsilon}{\sum_n \int_{\varepsilon_n}^{\infty} \Theta(\varepsilon-\varepsilon_n)(\varepsilon-\varepsilon_n)\tau(\varepsilon)\left(-\frac{\partial f}{\partial \varepsilon}\right)d\varepsilon}. \quad (6)$$

As can be seen from (6), the expression for the thermoelectric power includes the relaxation time, which is anisotropic in the case when the charge carriers scattered by optical phonons, depends on the components of the wave vector and is given by the formula [4]

$$\tau_{2D} = a\frac{2\sqrt{2mk_0T}}{3\pi\hbar}\tau_0\left(\frac{\varepsilon_\perp}{k_0T}\right)\sum_n \Theta(\varepsilon-\varepsilon_n), \quad (7)$$

where τ_0 - constant, which is not depend on the energy:

$$\tau_0 = \frac{\hbar^2\varepsilon^*}{e^2\sqrt{2mk_0T}},$$

here $(\varepsilon^*)^{-1} = \varepsilon_\infty^{-1} - \varepsilon_0^{-1}$, $\varepsilon_\infty, \varepsilon_0$ - high-frequency and statistical dielectric permittivity.

In the case of degenerate electron gas, passing formula (7) into expression (6) and integration by $\varepsilon_\perp$, for α we find:

$$\alpha = \frac{2\pi^2}{3}\frac{k_0}{e}\frac{\sigma_0}{\sigma}\left[(1+\bar{n})(\varepsilon_F^* - U_0^*) + 4\varepsilon_0^*\left(\frac{2}{3}\bar{n}^3 + 2\bar{n}^2 + \frac{4}{3}\bar{n} + 1\right) + \frac{\bar{n}^2+\bar{n}+2}{2}\right], \quad (8)$$

here $U_0^* = \frac{U_0}{k_0T}$, $\sigma_0 = \frac{e^2n_0\tau_{0r}}{m}$, $\varepsilon_0^* = \frac{\varepsilon_0}{k_0T}$, $\varepsilon_F^* = \frac{\varepsilon_F}{k_0T}$, where the Fermi level is equal:

$$\varepsilon_F = \frac{n_{el}\pi\hbar^2}{m(\bar{n}+1)} + U_0 + 2\sqrt{\varepsilon_0^2 + \varepsilon_0U_0}\,(\bar{n}+1) + \frac{4\varepsilon_0\left(\bar{n}^3+3\bar{n}^2+2\bar{n}+1.5\right)}{3(\bar{n}+1)}.$$

The electrical conductivity σ is given in work [5] and has the form:

$$\frac{\sigma}{\sigma_0} = (1+\bar{n})(\varepsilon_F^* - U_0^*)^2 + 4\varepsilon_F^*\varepsilon_0^*\left(\frac{2}{3}\bar{n}^3 + 2\bar{n}^2 + \frac{4}{3}\bar{n} + 1\right) +$$

$$+ \varepsilon_0^{*2}(3\bar{n}^5 + 15\bar{n}^4 + 36\bar{n}^3 + 33\bar{n}^2 + 30\bar{n} + 7) + 8U_0^*\varepsilon_0^*\left(\bar{n}^3 + 3\bar{n}^2 + 3\bar{n} + \frac{3}{4}\right) + \cdot \quad (9)$$

$$+ 4\sqrt{\varepsilon_0^*(\varepsilon_0^* + U_0^*)}\left[2\varepsilon_0^*(\bar{n}^4 + 4\bar{n}^3 + 7\bar{n}^2 + 4\bar{n} + 1) + \frac{\varepsilon_F^*}{2}(\bar{n}^2 + \bar{n} + 2) + \frac{6}{5}U_0^*\right]$$

where $\bar{n}$ is the integer part of the number

$$n = \sqrt{2m\varepsilon_F}\,\frac{a}{\pi\hbar} - \frac{1}{2} - \frac{1}{2}\sqrt{1 + \frac{U_0}{\varepsilon_0}}$$

which is found from the condition $\varepsilon_F = \varepsilon_n$ (number of filled subbands).

3. Discussion and conclusion

A numerical calculation from Eq. (8) shows that when the main scattering mechanism is scattering by optical phonons, which can be considered elastic in low-dimensional systems at temperatures on the order of 100 K [6], the thermopower increases with a decrease in the thickness of the well. This is explained by following way: when the thickness of the well decrease at increasing the electron momentum, the probability of scattering of charge carriers by polar optical phonons decreases. This fact will contribute to an increase in the thermoelectric quality factor, which agrees with the results of the experimental work [6, 7]. The thermoelectric power of a two-dimensional electron gas is considerably larger than in a three-dimensional one.

The dependence of the thermoelectric power on the thickness of the well is connected to the quantum effect - the restrict of the motion of an electron in a quantum well and is determined by the parameters of the quantum well U_0 and a.

References

[1] Balandin A. Physics of Low- Dimensional Structures ½, **1**, p.1-43 (2000).
[2] Crispin H.W. Barnes., Quantum transport in low-dimensional systems. Cambridge University Press, p. 220 (2004).
[3] Sur I.V. Semiconductor **43**, p.651-655 (2009).
[4] Askerov B.M., Figarova S.R., Kuliev B.I., Gadirova I.R., Journal of Physics: Condensed Matter **7**, p.843-848 (1995).
[5] Figarova S.R., Hasiyeva G.N., Figarov V.R. Physica E: Low-dimensional Systems and Nanostructures **78**, p. 10-13 (2016).
[6] Hicks L.D., Harman T.C., Sun X., Dresselhaus M.S.Physical Review B **53**, p.10493-10496 (1996).
[7] Wang J. Modern Physics Letters B **20**, p.215-223 (2006).

THE THEORY AND SIMULATION OF NEUTRON MODERATION SPECTRUMS IN HOMOGENEOUS URANIUM-CARBON MEDIA

S.A.CHERNEZHENKO, A.A.KAKAEV, A.V.RYBAK, V.P.SMOLYAR, V.A.TARASOV, V.V.URBANEVICH

Odessa National Polytechnic University, Shevchenko av., 1, 65044, Odessa, Ukraine,
vtarasov@ukr.net

Abstract. In [1, 2] the analytic expression for the neutron slowing down spectrum for an isotropic neutron source in slowing down neutron-absorbing reactor media was obtained. The expressions obtained for the spectra of slowing down neutrons allow us to reinterpret the physical nature of the processes determining the form of the neutron spectrum in the low-energy region of neutrons. The effect of the behavior of the elastic and inelastic neutron scattering cross sections of a media nuclei and a logarithmic energy decrement on the formation of the maximum of the neutron slowing down spectrum in the low-energy part of the spectrum is revealed.

Graphs are presented for the energy spectra of slowing down neutrons in hydrogen and uranium-carbon homogeneous media. The graphs are obtained by computer calculation using the theoretical expression from [1, 2] and using the GEANT4 code [3]. A comparative analysis of the neutron spectra for uranium-carbon slowing down media presented in our work, demonstrates a good agreement between the spectra calculated according to the developed theory and the spectra calculated by the Monte Carlo method.

***Key words**: neutron moderation, neutron spectra*

1. The theory of a neutron moderation in neutron moderating and absorbing media, containing different kinds of nuclei

According to [1] an analytic solution for stationary balance equation for moderated neutrons may be found as neutron flux density. In the case, considered in [1] the expression for the elastically scattered moderating neutron flux density is:

$$\Phi_1(E)=\frac{\int_E^{\infty}\frac{\Sigma_{el}(E')}{\Sigma_t(E')}Q(E')\cdot\left\{\exp\left[\int_{E'}^{\infty}-\frac{\Sigma_a(E'')dE''}{\left|\overline{\xi}_{el}\right|\Sigma_t(E'')\left[E''+\frac{1}{A}\cdot\frac{3}{2}kT\right]}\right]\right\}dE'}{\left[E+\frac{1}{A}\cdot\frac{3}{2}kT\right]\Sigma_t(E)\left|\overline{\xi}_{el}\right|}+\frac{\frac{\Sigma_{el}(E)}{\Sigma_t(E)}Q(E)}{\Sigma_t(E)},\qquad(1)$$

where $Q(E)$ is the quantity of neutrons generated with energy E per unit volume per unit time, Σ_{el} - total macroscopic cross section of elastic scattering of the moderating medium ($\Sigma_{el}=\sum_i\Sigma_{el}^i$, where Σ_{el}^i macroscopic cross section of the i-th nuclide in the moderator medium compound), $\Sigma_t=\Sigma_s+\Sigma_a$ - total macroscopic cross section, Σ_s - total macroscopic scattering cross section, Σ_a - total neutron absorption macroscopic cross section, $\left|\overline{\xi}_{el}\right|$ - modulus of average-logarithmic energy decrement for elastic scattering ξ_{el}, which is determined by analogy to standard neutron moderation theory, but through a new neutron elastic scattering law in [1].

The expression (1) contains probability function of resonant neutron non-absorption, but now containing moderating medium temperature:

$$\varphi(E')=\exp\left[-\int_E^{\infty}\frac{\Sigma_a(E')dE'}{\left|\overline{\xi}_{el}\right|\Sigma_t(E')\left[E'+\frac{1}{A}\cdot\frac{3}{2}kT\right]}\right].\qquad(2)$$

Given the inelastic scattering law from [2] and performing calculations analogous to the one made for elastic scattering in [1], we obtain an expression for inelastically scattered moderating neutrons flux density in the following form:

$$\Phi_2(E)=\left\{\frac{\int_E^{E_f}\frac{\Sigma_{in}(E)}{\Sigma_t(E)}Q(E)\,dE}{\left[E+\frac{1}{A}\cdot\frac{3}{2}kT\right]\Sigma_t(E)\left|\overline{\xi}_{in}\right|}+\frac{\frac{\Sigma_{in}(E)}{\Sigma_t(E)}Q(E)}{\Sigma_t(E)}\right\}\cdot\exp\left[-\int_E^{E_f}\frac{\Sigma_a(E')\,dE'}{\left|\overline{\xi}_{in}\right|\Sigma_t(E')\left[E'+\frac{1}{A}\cdot\frac{3}{2}kT\right]}\right],\quad(3)$$

where the average-logarithmic energy decrement of inelastic scattering ξ_{in} is introduced by analogy to standard neutron moderation theory, but through inelastic neutron scattering law from [2].

Therefore, considering elastic and inelastic neutron scattering it is possible to obtain an expression for total moderating neutrons flux density:

$$\Phi(E)=\Phi_1(E)+\Phi_2(E).\quad(4)$$

And the neutron spectrum will be defined by a standard expression:

$$\rho(E)\,dE=\frac{n(E)\,dE}{\int_0^{\infty}n(E)\,dE}=\frac{\frac{1}{\sqrt{2E}}\Phi(E)\,dE}{\int_0^{\infty}\frac{1}{\sqrt{2E}}\Phi(E)\,dE}.\quad(5)$$

2. The simulation of neutron moderation spectrums in homogeneous uranium-carbon media

For fission reactor environments *Q(E)* is determined by _fission spectrum of the fission nuclide or fission nuclides combination, which may be given by the following expression:

$$Q(E)=\tilde{Q}\cdot c\exp(-aE)sh\sqrt{bE}\,,\quad(6)$$

where *a*, *b* and *q* - constants, given in table 1 below, *E* - neutron energy nondimensionalized by 1 MeV,

$\tilde{Q}=\int_0^{\infty}Q(E)\,dE$ - total neutrons quantity generated in a unit volume in a unit time.

Table 1: Constants determining the fission spectrum for main reactor fission nuclides.

Constant	U235	Pu239	U233	Pu241
a	1.036	1.00	1.05 ± 0.03	1.0 ± 0.05
b	2.29	2.00	2.30 ± 0.10	2.20 ± 0.05
q	0.4527	0.48394	0.46534	0.43892

Fig. 1 shows the energy spectra of neutrons moderating in homogeneous uranium-carbon medium (5% 238U + 95% C). The theoretical curves were calculated using Eq. (5), and the Monte-Carlo simulated ones were obtained using GEANT4 software [3]. The neutron source was determined by Eq. (6) for uranium-235 in all cases. The neutron reactions cross-sections for uranium-238 and carbon were taken from ENDF/B-VII.1 [4]. The same simulation also was done for homogeneous uranium-carbon medium with different carbon content (0% − 100%).

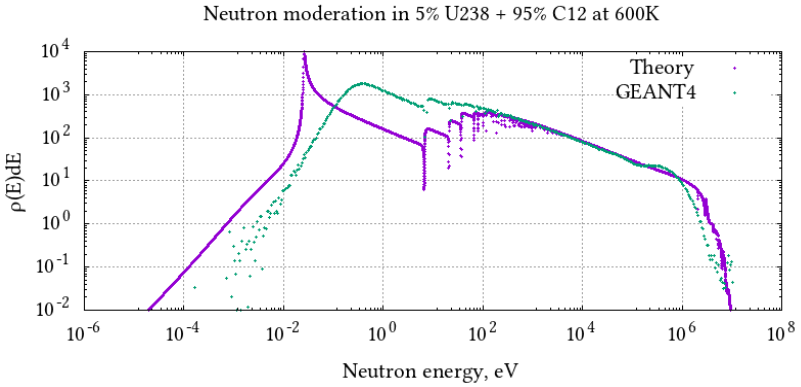

Figure 1: Energy spectrum of the moderating neutrons in uranium-carbon medium (5% 238U + 95% C) calculated using Eq. (5) (Theory) and using GEANT4 software. The initial spectrum was that of fission (6). The medium temperature is 600 K.

3. Conclusions

The energy spectra of neutrons moderating in homogeneous hydrogen and uranium-carbon media are presented. The graphs were obtained using the analytical expression (5) and the GEANT4 Monte-Carlo code [3]. The comparative analysis of the neutron spectra obtained using both methods reveals a good agreement.

REFERENCES

[1] V.D. Rusov, V.A. Tarasov, S.A. Chernezhenko, A.A. Kakaev, and V.P. Smolyar. European Physical Journal A - Hadrons and Nuclei, No.53:179. arXiv: 1612.06838v.1 [nucl-th]. (2017)

[2] V.D. Rusov, V.A. Tarasov, S.A. Chernezhenko, A.A. Kakaev, V.P. Smolyar, V.M. Vashchenko. arXiv: 1801.06142 v.1 [nucl-th]. P. 1-24. (2018)

[3] S. Agostinelli. Nuclear Instruments and Methods in Physics Research Section A: Accelerators, Spectrometers, Detectors and Associated Equipment. Vol. 506. − Issue 3. − P. 250-303. (2003)

[4] Chadwick M.B. ENDF/B-VII.1 Nuclear Data for Science and Technology: Cross Sections, Covariances, Fission Product Yields and Decay Data. / M.B. Chadwick, M. Herman, P. Obloinsk et al. // Nuclear Data Sheets. . - Vol. 112, Iss. 12. - P. 2887 - 2996. (2011)

THE POLARIZATION EFFECTS IN NEUTRON – NUCLEAR SCATTERING AT HIGH ENERGIES

S.G. ABDULVAHABOVA, G.V. GULIYEVA

Baku State University, Z. Khalilov st. 23, AZ-1148, Baku, Azerbaijan
sajida.gafar@gmail.com; qgunel150@gmail.com

Abstract. The high energy neutron -nucleus collisions is discussed by means of the multiple - diffraction theory. The analysis shows that when the preasymptotic corrections are absent, we have the zero polarisations. In the case of diffraction scattering a nonzero polarization of the scattered particles arises, which is related to the logarithmic derivative of the differential scattering cross section. Polarization changes sign in those processes whose angular distributions contain the second diffraction maximum. It was found that the sign of the polarization change between the quasielastic and deep inelastic range of energies. This is due to the interference of spin transfer from the positive and negative scattering angles and different signs of polarization associated with positive and negative scattering angles.

***Key words**: nucleon, scattering, diffraction, spin-orbital interaction, polarization, cross section.*

1. Introduction

At the present time the theoretical and experimental research leads to the conclusion about the essential role of the spin of the particles in the high energy scattering. This makes a basis for the hypothesis about the existence of a non-zero polarization research on the future accelerators will provide information about the structure of the nucleon interaction at large distances.

Polarization of particles scattered from unpolarized particles can occur primarily due to the spin–orbit interaction between the continuum projectile and the target [1]. The filtration of unpolarized neutron beam through a polarized beam of the target will be relatively enriched hadrons with the polarization direction for which the interaction cross section of the smaller, there will be a polarization of the beam in this direction.

In this paper we consider the model results for the polarization effects of neutron-nuclei scattering at high energies. The spin-polarization effects are used not only as battle probes for determining the accuracy of the model employed, but also play a critical role in understanding the spin-dependent interactions involved in the collision dynamics.

2. Cross - section and polarization function

The applicability of the Glauber-Sitenko diffraction scattering is determined [2] by the conditions of adiabaticity and eikonality. Adiabaticity is the neglect of the nucleus internuclear nucleus motion during the passage of a falling particle through it. The eikonal approximation (high-energy approximation) is widely and successfully used to describe the scattering of particles in complex nuclei as scattering in a certain continuous optical medium. In this approximation, instead of the law of conservation of energy, the law of conservation of the momentum projection holds. This means that the movement in the transverse directions is completely neglected. In high-energy scattering, the wavelength of a particle is much smaller than the dimensions of the potential. In addition, in the eikonal approximation, no restrictions are imposed on the masses and coordinates of the particles, both the final radius and the recoil are considered exactly, and the effect of distortion is taken into account only in the phase of the plane wave. Therefore, the eikonal approximation can be used to calculate the angular distributions of scattered particles. In the case of elastic scattering in this approximation, the scattering amplitude is calculated by the eikonal wave functions.

Under the assumption that the kinetic energy of the incident neutron is large in comparison with the binding energies of the individual particles, the interaction of the incident particle with the particles of the nucleus can be treated independently. The maximum collision frequency is *A*. With each scattering center, the incident particle interacts only once. It can not dissipate at one of the potential centers, then on some other and again at the first. This is due to the fact that in the diffraction approximation the particle propagates only along a straight line and can not be scattered backward.

*) Corresponding author: sajida.gafar@gmail.com

In the case of a spherically symmetric central field we have the following expression for the scattering amplitudes

$$f(k,\theta) = ik\int bdbJ_0(qb)\left[1-e^{i\chi_c(b)}\right]. \qquad (1)$$

In terms of the transmitted momentum (1) is as follows

$$f(\mathbf{q}) = \frac{ik}{2\pi}\int \exp(i\mathbf{qb})\left\langle \Psi\left|\Gamma(\mathbf{b})\right|\Psi\right\rangle d\mathbf{b}\,, \tag{2}$$

$$\Gamma(\mathbf{b}) = 1 - \prod_{j=1}^{A}\left[1-\gamma_j(\mathbf{b}-\mathbf{s_j})\right]. \tag{3}$$

Here **q** is the momentum transfer, k is the value of the wave vector of the nucleon, **b** is the impact-parameter vector, $\Psi(\mathbf{r}_1,\mathbf{r}_2,...,\mathbf{r}_A)$ is the ground state wave function of the nuclei, $\Gamma(\mathbf{b})$ is the total nucleon–nuclei interaction profile function, $\gamma_j(\mathbf{b})$ is the profile function for the nucleon-nucleon interaction, brackets $\langle||\rangle$ mean interactions over the nucleon coordinates.

Using the (2) the elastic scattering cross section is equal to

$$\sigma_{el} = 2\int\left(1 - \mathrm{Re}e^{-\frac{i}{v}\int_{-\infty}^{\infty} V\left(\mathbf{b}+\hat{k}_i z\right)dz}\right)d^2b\ . \tag{4}$$

We use the term 'spin-flip' above to denote the abrupt (discontinuous) change in the spin state which can occur when a particle emits a photon. There is no deterministic time evolution linking the spin states before and after a spin-flip photon emission. If one runs time backwards, the spin does not return from the 'down' to the 'up' state. There is, however, another widely employed usage for the term 'spin-flip'. This alternative usage is generally employed when discussing nonradiative polarization. It simply means a reversal of the spin direction, i.e. a 180° spin rotation, but not a discontinuous change of the spin state. In this case, there is a deterministic time evolution linking the final spin state to the initial spin state, although it may be complicated to calculate. If one runs time backwards, the spin does return to its original state. Indeed, the classical spin model is used to describe the spin motion throughout such a spin-flip process.

At sufficiently high energies of the relative motion of the colliding nucleons, we can confine ourselves to the first Born approximation. The scattering amplitude f is elements of the 2 x 2 matrix, which can be expressed in terms of the Pauli matrices $\boldsymbol{\sigma}$ and the identity matrix *E*

$$f = g\mathrm{E} + (\mathbf{h}\boldsymbol{\sigma})\,. \tag{5}$$

In (5), the factor *g* corresponds to an interaction independent of spin, and the vector *h* to the interaction causing the reorientation of the spin [3].

Due to the spin dependence of the interaction, the scattering cross section can depend on the polarization of the incident particle and on the polarization of the target. Using the definition of the differential scattering cross section we obtain that

$$\sigma(\theta,\varphi) = \{1 + P(\theta)\cos\phi\}\left(|g(\theta)|^2 + |h(\theta)|^2\right), \tag{6}$$

$$P(\theta) = 2\frac{\mathrm{Re}(g^* h)}{I(\theta)}\ . \tag{7}$$

In the scattering of unpolarized neutrons on nuclei, polarization of elastically scattered neutrons arises. Since the scattering amplitude contains a term that depends on the orientation of the spin, and a term that does not depend on the spin orientation, the polarization is due to interference between these two scattering parts. Large values of the degree of polarization (the absolute value of the polarization vector is called the degree of polarization) are possible in the case when the interference value is comparable with the scattering cross section.

The model prediction for the polarisation of elastic n-^9Be scattering, corresponding to the experimental data at neutron energy 350 MeV [4] is shown in fig.1. Note that the model predicts a large polarisation at high energies in the range of the diffraction peak. The polarization vector of particles scattered on nuclei with zero spin is always directed perpendicular to the scattering plane. It should be noted that the polarization parameter decreases with increasing energy at small momentum transfers, since with increasing energy the region of small momentum transfers increasingly corresponds to the collinear configuration of the scattered particles, and the polarization must be zero. The analysis shows that when the preasymptotic corrections are absent, we have the zero polarisations. It is important to emphasise that the case of the nucleon-nuclei scattering the leading asymptotic terms of the spiral amplitudes is also determined by the contribution of the quark cluster with the evident replacement of $f(q)$ by the pion-nucleon scattering amplitudes.

Large values of the degree of polarization (the absolute value of the polarization vector is called the degree

of polarization) are possible in the case when the interference value is comparable with the scattering cross section.

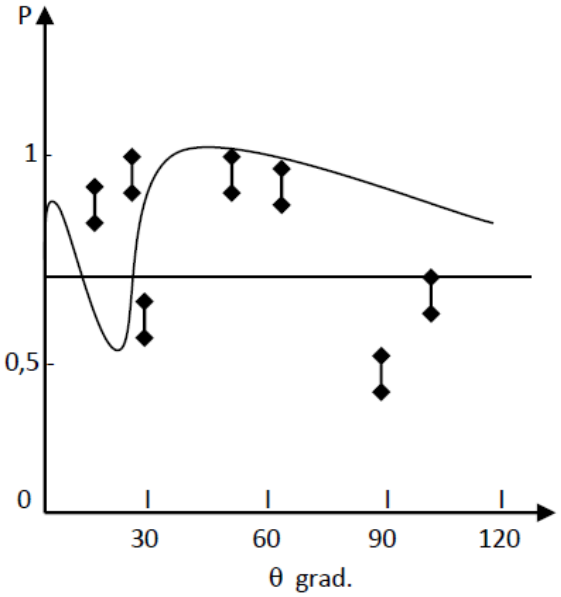

Fig.1 The polarisation of the proton in n^{9}Be reaction. The solid line corresponds to the theoretical data, point data from [4].

The analysis performed shows that in this case the reliable results of the predicted spin effects should be expected at an energy above 350Mev. At a lower energy the agreement of the theory with experiment can be only qualitative.

If polarization measurements were performed as a function of energy, it was found that the sign of the polarization varies between the quasielastic and deep inelastic regions of energy. This is explained by the interference of spin transfer from positive and negative scattering angles [5]. Different polarization signs are associated with positive and negative scattering angles and the polarization can be zero if there is a balance of scattering from both sides.

It has been shown in the works [6, 7] that polarization function arises from the quantum spin-entanglement of the projectile-target system in addition to the separable total spin depending on the collision energy and scattering angle.

3. Conclusion

Spin effects are important from the point of view of studying the structure of particles, in particular, the problem of the relationship between the spin of a particle and the spin of its components and the interaction mechanism of the components. A qualitative description of the polarization of hyperons is explained by the spin-orbit interaction in a scalar field that connects quarks within the hadron.

Experiments on the study of polarization effects are carried out in all accelerators. After the experimental discovery of a number of important spin effects, taking into account the spin degrees of freedom became a necessary part of the theoretical analysis. The spin dependence of forces between nucleons is the need for a large number of experiments to determine the interaction. If this dependence is absent, the scattering experiments could identify only a single value for each scattering angle and energy - the differential cross section.

Using different hypotheses about the property of the nucleon interaction at large distances a number of model approaches lead to the nondisappearing polarization in high -energy processes at small transfer moment.

We assume that the considered scaling property for polarization processes rejects selfsimilarity of the spin structure of the colliding objects, interaction mechanism of their constituents, and process of fragmentation of the polarized constituents in the final state

The study of spin phenomena gives more rich information than the study of spin-averaged quantities, and the quantities measured in the corresponding experiments are more fundamental, which allows for a detailed analysis of various theoretical concepts and approaches.

REFERENCES

[1] K. F. Haque et al J. Phys. Commun. **1** 035014, (2017).

[2] F.G. Sitenko, PEAN, V.4(2), p. 546, (1973).
[3] R.A. Ahmedov, Proceedings of the ıx Internatıonal Workshop on Nuclear Structure Properties, Turkey, p.30, (2016).
[4] B.M. Bichkov et all, PEAN, V.14(2), p. 373,(1983).
[5] Bartschat Kand, S. F. Santos, Phys. Rev. A 95 042707 (2017).
[6] Blum Kand, B. Lohmann, Phys. Rev. Lett. 116 033201 (2016).
[7] Lohmann, B. Blum Kand Langer, Phys. Rev. A 94 032331 (2016).

ANALYTICAL BOUND STATE SOLUTIONS OF THE DIRAC EQUATION FOR HULTHÉN POTENTIAL WITHIN THE SPIN-ORBIT COUPLING TERM AND SPIN SYMMETRY

M. V. QOCAYEVA[1], S. M. ASLANOVA[2], A. I. AHMADOV[2]

[1]Institute of Physics, Azerbaijan National Academy of Sciences,
H.Javid Avenue,131, AZ-1143, Baku, Azerbaijan
E-mail:mefkureqocayeva@yahoo.com
[2]Baku State University,Z. Khalilov str.23, AZ-1148, Baku, Azerbaijan,
E-mail:ahmadovazar@yahoo.com

Abstract. In this paper the approximately analytical bound state solutions of the Dirac equation with the Hulthén potential for arbitrary spin–orbit coupling quantum number k are carried out by taking a properly approximate expansion for the spin–orbit coupling term. In the case of exact spin symmetry, and pseudospin symmetry the associated two-component spinor wave functions of the Dirac equation for arbitrary spin–orbit quantum number k are presented and the corresponding bound state energy equation is derived. The bound state energy eigenvalues and the corresponding spinors are obtained in the closed forms.

Key words: Hulthén potential, exact spin symmetry, pseudospin symmetry

1. Introduction

One of the primary goals in the quantum mechanics is to find exact solutions of the stationary wave equation, for example Dirac equation because they contain all the necessary information on quantum system consideration. Since the wave function contains all essential information for full description of a quantum system, therefore, an analytical solution of the Schrödinger, Klein-Fock-Gordon and Dirac equations is of high importance in quantum mechanics [1]. There are few potentials for which the Dirac equation are able solved exactly for any spin-orbit coupling quantum number k.

However, analytic solutions are possible only for a few simple quantum systems like the movement in the spherical simmetrical field and the linear harmonic oscillator. In general, many quantum systems can only be treated by approximation methods or numerical solutions.

As known, one of the main purpose in theoretical physics since the early years of quantum mechanics (QM) is to obtain an exact solution of the Dirac equation for some special potentials in physical interest. It would be interesting and an significant to solve the Dirac equation for the Hulthén potential any spin-orbit coupling quantum number k in cases exact spin and pseudospin symmetry. Hulthén potential for spin-orbit quantum number k since it has been extensively used to describe the bound and continuum states of the interacting systems. The pseudospin symmetry with the nuclear shell model has been introduced many years ago and it has been widely applied to explain and describing of phenomena in nuclear physics and related others areas.

It is very significant to notice that Dirac eduqtion for the Manning-Rosen and Hulthén potentials are studied in Refs. [2,3]. In Ref.[4] a complete solution of the problem of squaring the Dirac equation with arbitrary external electromagnetic field is expounded.

Therefore, it would be interesting and important to solve Dirac equation for the Hulthén potential since it has been extensively used to describe the bound and the continuum states of the interaction systems.

Thus, the main purpose of our investigation is the analytical solution of modified Dirac equation for the Hulthén potential for arbitrary spin–orbit quantum number k in the case of exact spin symmetry and pseudospin symmetry within quantum mechanics using Nikiforov-Uvarov (NU) method[5]. This method is based on solving the second-order linear differential equation by reducing to a generalized equation of hypergeometric-type which is a second-order type homogeneous differential equation with polynomials coefficients of degree not exceeding the corresponding order of differentiation.

The Hulthèn potential is defined by [6,7]

$$V_H(r) = -\frac{Ze^2\delta e^{-\delta r}}{(1-e^{-\delta r})}. \qquad (1)$$

Here Z and δ are respectively the atomic number and the screening parameter, determining the range for the Hulthèn potential.
The Hulthèn potential is one of the important short-range potentials in physics, extensively using to describe the bound and continuum states of the interaction systems. It has been applied to the several research areas such as nuclear and particle physics, atomic physics, condensed matter and chemical physics, so the analyzing relativistic effects for a particle under this potential could become significant, especially for strong coupling. At small values of the radial coordinate r, the Hulthèn potential behaves like a Coulomb potential, whereas for large values of r it decreases exponentially so that its influence for bound state is smaller than, that of Coulomb potential. In contrast to the Hulthèn potential, the Coulomb potential is analytically solvable for any l angular momentum. Take into account of this point will be very interesting and important solving Dirac equation for the Hulthèn potential for any l states within ordinary quantum mechanics.

2. Bound states of the Hulthèn potential with arbitrary k

The Dirac equation of a nucleon with mass *M* moving in an attractive scalar potential $S(r)$ and a repulsive vector potential $V(r)$ can be written as $(\hbar = c = 1)$:

$$\left[\vec{\alpha}\vec{p} + \beta(M + S(r))\right]\psi(r) = \left[E - V(r)\right]\psi(r) \tag{2}$$

where E is the relativistic energy of the system, and α and β are the 4×4 Dirac matrices.

For spherical symmetrical nuclei, the total angular momentum of the nucleon J and spin–orbit matrix $\hat{K} = -\beta(\hat{\sigma}\cdot\hat{L} + 1)$ commute with the Dirac Hamiltonian $[\hat{H}^D, \hat{K}] = 0$, where L is the orbital angular momentum. The eigenvalues of *K* are $k = \pm(j + 1/2)$, where $k = -(j + 1/2) < 0$ is for the aligned spin $j = l + 1/2 (s_{1/2}, p_{3/2}, ets)$ and $k = (j + 1/2) > 0$ is for the unaligned spin $j = l - 1/2 (p_{1/2}, d_{3/2}, ets)$. The complete set of the conservative quantities can be taken as (H, K, J^2, J_z) and the spinor wave functions can be classified according to their angular momentum j, k and the radial quantum number n. The spherically symmetric Dirac spinor wave functions can be written as

$$\psi_{nk} = \frac{1}{r}\begin{bmatrix} F_{nk}(r) & Y^l_{jm}(\theta,\varphi) \\ iG_{nk}(r) & Y^{\tilde{l}}_{jm}(\theta,\varphi) \end{bmatrix} \tag{3}$$

where the upper and lower components $F_{nk}(r)$ and $G_{nk}(r)$ are real square-integral functions, $Y^l_{jm}(\theta,\varphi)$ and $Y^{\tilde{l}}_{jm}(\theta,\varphi)$ are the spherical harmonic functions, and m is the projection of the total angular momentum on the third axis, and $l(l+1) = k(k+1)$, $\tilde{l}(\tilde{l}+1) = k(k-1)$

The substitution of Eq. (3) into (2) yields two coupled differential equations as follows:

$$\left(\frac{d}{dr} + \frac{k}{r}\right)F_{nk}(r) = \left[M + E_{nk} + S(r) - V(r)\right]G_{nk}(r), \tag{4}$$

$$\left(\frac{d}{dr} - \frac{k}{r}\right)G_{nk}(r) = \left[M - E_{nk} + S(r) + V(r)\right]F_{nk}(r). \tag{5}$$

By eliminating $G_{nk}(r)$ in Eq. (4) and $F_{nk}(r)$ in Eq. (5), one is able to obtain two second-order differential equations for the upper $F_{nk}(r)$ and lower $G_{nk}(r)$ components as follows:

$$\left\{\frac{d^2}{dr^2} - \frac{k(k+1)}{r^2} - \left[M + E_{nk} - \Delta(r)\right]\left[M - E_{nk} + \Sigma(r)\right] + + \frac{\frac{d\Delta(r)}{dr}\left(\frac{d}{dr} + \frac{k}{r}\right)}{M + E_{nk} - \Delta(r)}\right\}F_{nk}(r) = 0, \tag{6}$$

$$\left\{\frac{d^2}{dr^2} - \frac{k(k-1)}{r^2} - \left[M + E_{nk} - \Delta(r)\right]\left[M - E_{nk} + \Sigma(r)\right] + \frac{\frac{d\Sigma(r)}{dr}\left(\frac{d}{dr} - \frac{k}{r}\right)}{M - E_{nk} + \Sigma(r)}\right\}G_{nk}(r) = 0, \tag{7}$$

here $\Delta(r) = V(r) - S(r)$ and $\Sigma(r) = V(r) + S(r)$.

Now, let us consider the exact spin symmetry, in this case $d\Delta/dr = 0$ then $\Delta = const$. In this work we take $\Sigma(r)$ as the Hulthén potential, $\Sigma(r) = V_H(r)$

$$\Sigma(\mathrm{r}) = -\frac{\mathrm{Ze}^2\delta \mathrm{e}^{-\delta \mathrm{r}}}{1-\mathrm{e}^{-\delta \mathrm{r}}}. \tag{8}$$

Substituting Eq. (8) into Eq. (6) then we obtain:

$$\left\{\frac{\mathrm{d}^2}{\mathrm{dr}^2} - \frac{\mathrm{k(k+1)}}{\mathrm{r}^2} - \left[\mathrm{M} + \mathrm{E_{nk}} - \mathrm{c}\right]\Sigma(\mathrm{r}) + \left[\mathrm{E_{nk}^2} - \mathrm{M}^2 + \mathrm{c(M - E_{nk})}\right]\right\}\mathrm{F_{nk}(r)} = 0 \tag{9}$$

This equation cannot be solved analytically except for *s*-wave $k = -1$ case due to the spin–orbit coupling term $\mathrm{k(k+1)/r}^2 \to 0$. Therefore, we must use a proper approximation to spin–orbit coupling term. For the solving this problem in this work we apply a new approximate scheme to the centrifugal term [8-10]

$$\frac{1}{\mathrm{r}^2} \approx \delta^2\left(\mathrm{C_0} + \frac{\mathrm{e}^{-\delta \mathrm{r}}}{(1-\mathrm{e}^{-\delta \mathrm{r}})^2}\right). \tag{10}$$

where the parameter $\mathrm{C_0} = 1/12$ [11], is a dimensionless constant. However, when $\mathrm{C_0} = 0$, the approximation scheme becomes the convectional approximation scheme suggested by Greene and Aldrich [12].

Substituting expression (10) into (9) then we obtain:

$$\left[\frac{d^2}{dr^2} - \left[M + E_{nk} - c\right]\Sigma(r) + \left[E_{nk}^2 - M^2 + c(M - E_{nk})\right] - k(k+1)\delta^2\left(C_0 + \frac{e^{-\delta r}}{(1-e^{-\delta r})^2}\right)\right]F_{nk}(r) = 0. \tag{11}$$

Main aim to transform Eq. (11) the equation of the generalized hypergeometric type which is in the form:

$$\chi''(x) + \frac{\tilde{\tau}}{\sigma}\chi'(x) + \frac{\tilde{\sigma}}{\sigma^2}\chi(x) = 0. \tag{12}$$

The Eq.(11) can be further simplified using a new variable $s = e^{-\delta r}$. Taking into account, that here $\mathrm{r} \in [0,1]$ and $\mathrm{s} \in [1,0]$, then we obtain:

$$\frac{d^2F_{nk}(s)}{ds^2} + \frac{1}{s}\frac{dF_{nk}(s)}{ds} + \left[\frac{Ze^2}{\delta s(1-s)}\left[M + E_{nk} - c\right] + \frac{1}{s^2\delta^2}\left[E_{nk}^2 - M^2 + c(M - E_{nk})\right] - \right.$$
$$\left. - \frac{k(k+1)}{s^2}\left[C_0 + \frac{s}{(1-s)^2}\right]\right]F_{nk}(s) = 0. \tag{13}$$

Here we use following ansats in order to make the differential equation more compact,

$$\alpha^2 = \frac{Ze^2\left(M + E_{nk} - c\right)}{\delta} \quad \text{and} \quad \beta^2 = \frac{M^2 - E_{nk}^2 - c(M - E_{nk})}{\delta^2}. \tag{14}$$

Now, NU method can be successfully applied to define the eigenvalues of energy. By comparing Eq.(13) with Eq.(12) and applying Nikiforov-Uvarov metod after this a long and cumbersome calculations for energy spectrum we find:

$$\beta^2 = \left[\frac{\alpha^2 - (k+n+1)^2}{2(k+n+1)}\right]^2 - k(k+1)C_0 \tag{15}$$

Take into account (14) into (15), then for energy spectrum we obtain:

$$\mathrm{M}^2 - \mathrm{E_{nk}^2} - \mathrm{c(M - E_{nk})} = \delta^2\left[\frac{Ze^2\left(M + E_{nk} - c\right)}{2\delta(k+n+1)} - \frac{k+n+1}{2}\right]^2 - k(k+1)C_0\delta^2 \tag{16}$$

If in the Eq.(16) we take $\mathrm{C_0} = 0$ then we directly obtain result [3].

If we take the following factorization

$$\mathrm{F_{nk}(s)} = \phi(\mathrm{s})\mathrm{y(s)} \tag{17}$$

for the appropriate function $\phi(\mathrm{s})$, Eq.(13) takes the form of the well-known hypergeometric-type equation. The appropriate $\phi(\mathrm{s})$ function has to satisfy the following condition:

$$\frac{\phi'(\mathrm{s})}{\phi(\mathrm{s})} = \frac{\pi(\mathrm{s})}{\sigma(\mathrm{s})}, \tag{18}$$

where function $\pi(s)$ is defined as

$$\pi(s)=\frac{\sigma'-\bar{\tau}}{2}\pm\sqrt{\left(\frac{\sigma'-\bar{\tau}}{2}\right)^2-\bar{\sigma}+k\sigma}\ . \tag{19}$$

Finally for $\pi(s)$ we found:

$$\pi(s)=-\frac{s}{2}\pm\begin{cases}\left(\sqrt{c}-\sqrt{c+a-b}\right)s-\sqrt{c}\ , & k=(b-2c)+2\sqrt{c^2+c(a-b)}\\ \left(\sqrt{c}+\sqrt{c+a-b}\right)s-\sqrt{c}\ , & k=(b-2c)-2\sqrt{c^2+c(a-b)}\end{cases}. \tag{20}$$

Solving the Eq.(18) then for $\phi(s)$ we found:

$$\phi(s)=s^{\sqrt{c}}(1-s)^K\ . \tag{21}$$

Here, $K=k+1$, and $\sqrt{c}=\sqrt{\beta^2+k(k+1)}$. Then for $\phi(s)$ finally we obtain:

$$\phi(s)=s^{\sqrt{\beta^2+k(k+1)}}\ . \tag{22}$$

Furthermore, the other part of the wave function $y(s)$ is the hypergeometric-type function whose polynomial; solutions are given by Rodrigues relation

$$y_n(s)=\frac{C_n}{\rho(s)}\frac{d^n}{ds}\left[\sigma^n(s)\rho(s)\right] \tag{23}$$

where C_n is a normalizing constant and $\rho(s)$ is the weight function which is the solution of the Pearson differential equation. The Pearson differential equation and $\rho(s)$ for our problem is given as

$$(\sigma\rho)'=\tau\rho\ . \tag{24}$$

It is easy to find the second part of the wave function from the definition of weight function. Thus, solving the Eq.(24) very easy we found the second part of the wave function in this form:

$$\rho(s)=(1-s)^{2K-1}s^{2\sqrt{c}}\ . \tag{25}$$

Substituting Eq.(25) in Eq.(23), we get

$$y_n(s)=C_n(1-s)^{1-2K}s^{2\sqrt{c}}\frac{d^n}{ds^n}\left[s^{2\sqrt{c}+n}\cdot(1-s)^{2K-1+n}\right]=C_nP_n^{(2\sqrt{c},2K-1)}(1-2s)\ . \tag{26}$$

Finally substituting $\phi(s)$ and $y(s)$ into Eq.(17), then for the $F_{nk}(s)$ eigenfunctions we obtain:

$$F_{nk}(s)=C_ns^{\sqrt{c}}(1-s)^KP_n^{(2\sqrt{c},2K-1)}(1-2s) \tag{27}$$

After simple calculations, we obtain normalization constant as

$$C_n=\sqrt{\frac{n!2\sqrt{c}(n+K+\sqrt{c})\Gamma((2K+\sqrt{c})+n)}{(n+K)\Gamma(n+2\sqrt{c}+1)\Gamma(n+2K)}}\ . \tag{28}$$

In the case of exact pseudospin symmetry in Eq. (7) we take $d\Sigma(r)/dr=0$, and $\Sigma(r)=c=const$, then Eq.(7) we can write in this form:

$$\left[\frac{d^2}{dr^2}-\frac{k(k-1)}{r^2}-\left[M+E_{nk}-\Delta(r)\right]\left[M-E_{nk}+c\right]\right]G_{nk}(r)=0 \tag{27}$$

here $k=-\tilde{l}$ for $k<0$ and $k=\tilde{l}+1$ for $k>0$, $\Delta(r)$ is the Hulthèn potential. The energy eigenvalues depend on n and $\tilde{l}$, $E_{nk}=E(n,\tilde{l}(\tilde{l}+1)$. The eigenstates with $j=\tilde{l}\pm1/2$ are degenerate for $\tilde{l}\neq0$ which is well known as the exact pseudospin symmetry. Here, also as above Eq.(16) cannot be solved exactly for the Hulthén potential for $k\neq0$ by using the standard methods. Therefore, the solving this problem we apply a new approximate scheme to the centrifugal term presented in Eq.(27).

Thus, solving Eq.(27) by NU method for the energy eigenvalues obtain:

$$\beta^2 = \left[\frac{\alpha^2}{2(n+1-k)} - \frac{n+1-k}{2} \right]^2 - k(k-1)C_0 \tag{28}$$

To take into account in the case exact pseudospin symmetry β^2 defined in this form:

$$\beta^2 = \frac{M^2 - E_{nk}^2 + c(M + E_{nk})}{\delta^2} \ . \tag{29}$$

Substituting expression (29) into (28) then we obtain:

$$(M + E_{nk})(M - E_{nk} + c) = \delta^2 \left[-\frac{Ze^2(M - E_{nk} + c)}{2\delta(n+1-k)} - \frac{n+1-k}{2} \right]^2 - k(k-1)C_0\delta^2 \tag{30}$$

For arbitrary spin–orbit coupling quantum number $k \neq 0$ in the exact pseudospin symmetry case $G_{nk}(s)$ eigenfunctions of this potential defined in this form:

$$G_{nk}(s) = C_n s^{\sqrt{c}} (1-s)^{\tilde{K}} P_n^{(2\sqrt{c}, 2\tilde{K}-1)}(1-2s) \, . \tag{31}$$

Where $\tilde{K} = k$

As is seen from Eqs.(16,27) and (30,31) energy spectrum and eigenfunctions very sensitive the choosing spin–orbit coupling quantum number k .

3. Conclusion

In this work, we have presented the bound state solutions of the Dirac equation for the Hulthén potential within the framework by using the developed scheme to overcome the centrifugal part.

For arbitrary spin–orbit coupling quantum $k \neq 0$ state, we have obtained the energy eigenvalues and Dirac spinors in the closed form for the case of the exact spin symmetry and exact pseudospin symmetry cases. The analytical formulas, given by Eqs. (16,27,30,31) may have interesting applications in nuclear and particle physics and related areas. Regarding the method presented in this study, we should point out that it is a systematic one and it is very efficient and practical in solving the exact spin and pseudospin symmetric systems for any spin–orbit coupling quantum $k \neq 0$ state.

A closed form of the normalization constant of the wave functions is also found. The energy eigenvalues and corresponding eigenfunctions are obtained for arbitrary $k \neq 0$ spin–orbit coupling quantum number and n_r radial quantum numbers.

It is worth to mention that the Hulthén potential is one of the important exponential potential, and it is a subject of interest in many fields of physics and chemistry. The main results of this paper are the explicit and closed form expressions for the energy eigenvalues, eigenfunctions and the normalized wave functions. The method presented in this study is a systematic one and in many cases it is one of the most concrete works in this area.

Consequently, studying of analytical solution of the modified Dirac equation is obtained for the Hulthén potential within the framework quantum mechanics could provide valuable information on the dynamics at nuclear, atomic and molecule physics and opens new window.

We can conclude that our analytical results of this study are expected to enable new possibilities for pure theoretical and experimental physicist, because the results are exact and more general.

References

[1]. W. Grenier, Quantum Mechanics An Itroduction, Fourth ed. Springer, Berlin, 2000.
[2]. Gao-Feng Wei and Shi-Hai Dong, Physics Letters A, **373**, 49 (2008).
[3]. A. Soylu, O Bayrak and I. Boztosun, Journal of Mathematical Physics **48**, 082302 (2007).
[4]. V.G.Bagrov, Russian Physical Journal **61**, 403 (2018).
[5]. A.F. Nikiforov and V.B. Uvarov, Special Functions of Mathematical Physics, Birkhäuser, Basel 1988.
[6]. L. Hulthén, Arkiv för Mathematik, Astronomi och Fysik A **28**, 5 (1942).
[7]. L. Hulthén, Arkiv för Mathematik, Astronomi och Fysik **29** B, 1 (1942).
[8].Wen-Chao Qiang, Shi-Hai Dong, Physics Letters A **363**, 169 (2007).
[9]. Gao-Feng Wei, Shi-Hai Dong, Physics Letters A **373**, 49 (2008).
[10]. Wen-Chao Qiang, Shi-Hai Dong, Physica Scripta **79**, 045004 (2009).
[11]. C.S. Jia, T. Chen and L. G. Cui, Physics Letters A **373**, 1621 (2009).
[12]. R.L. Greene and C. Aldrich, Physical Reveiw A **14**, 2363 (1976).

ELECTROPHYSICAL PARAMETERS OF PP+Fe_3O_4 BASED NANOCOMPOSITES DEPENDING ON TEMPERATURE-TIME MODE OF CRYSTALLIZATION

M.A.RAMAZANOV, H.A.SHIRINOVA, F.V.HAJIYEVA, A.M.MAHARRAMOV, LUCA DI PALMA

[a]*Baku State University, Physics Faculty, Z. Khalilov Street, 23 Baku, AZ1148, Azerbaijan*
Department of Chemical Engineering Materials Environment, Sapienza University, Via Eudossiana 18, 00184 Roma, Italy

Abstract. In the present study, the influence of the temperature–time mode of crystallization (TTC) on the electrophysical properties of polymer-based PP+Fe_3O_4 nanocomposite materials was investigated. Also, the effect of the temperature-time mode of crystallization of nanocomposites on the negative magnetoresistance (NMR) effect that observed in this material was investigated. It was found that dielectric permittivity of polymer nanocomposites rises with increasing of cooling rate. The cooling rate of nanocomposites after hot-pressing also affects the NMR effect of these materials. The conductivity of the material under the influence of magnetic field improves with increasing of its cooling rate, which leads to increasing of NMR effect.

Key words: *Isotactic polypropylene, magnetite, dielectric permittivity, negative magnitoresistance*

1. Introduction

Electronic materials are the foundation of the devices we use daily to make our lives easier and more productive and are a key building block for the technologies of the future. As we demand more capability from these devices—working at room temperature, with high elasticity, low cost smaller components, —the need grows for correlated physical and electrical characterization at the nanometer scale.

Spintronics, also known as spin electronics, is the study of the intrinsic spin of the electron and its associated magnetic moment, in addition to its fundamental electronic charge, in solid-state devices. The spin-dependent conduction of ferromagnetic materials in heterostructures gives rise to new phenomena such as giant magnetoresistance (GMR) in magnetic multilayers or tunnel magnetoresistance (TMR) in magnetic tunnel junctions [1-2]. The system in which the non-magnetic insulating polymer serves as a matrix, while magnetic inorganic materials are used as the fillers is potential new materials for spintronics. The polymer layer between two ferromagnetic nanoparticles plays the role of the potential barrier for electron transportation. Under the influence of the external magnetic field, the spin of the ferromagnetic nanoparticles, distributed in the polymer matrix is oriented in the same direction[3]. If the magnetizations are in a parallel orientation it is more likely that electrons will tunnel through the insulating film than if they are in the oppositional (antiparallel) orientation. Consequently, such a junction can be switched between two states of electrical resistance, one with low and one with very high resistance.

The electric conductivity and other electrophysical parameters of the nanocomposites significantly depend on the interphase layer between the matrix and filler. Formation of the conduction channel in the binary nanosystem mostly depends on the interfacial contact area between the two conducting nanograin. In the present work, we studied the influence of the temperature–time mode of crystallization (TTC) on the structures and electrophysical properties of polymer-based nanocomposites PP+Fe_3O_4.

Materials and Methods

2.1. Materials

Isotactic polypropylene (PP grade Moplen HF500N, homopolymer); density - 0,92g/cm^3 at 25^{0}C, Mw = 250000, Mn = 67000, Melt Mass-Flow Rate- MFR = 11,5g /10 min (230^{0}C, 2.16 kg), melting T = 162^{0}C. Fe_3O_4 nanopowder with size 7-15nm[1].

2.2. Synthesis of magnetic polymeric nanocomposites

The polymer nanocomposite materials were prepared as follows: isotactic polypropylene was solved in toluene solvent, at a temperature 120^{0}C. Magnetite nanoparticles were added to the polymer solution at different weight contents (1%, 5%, 7%, 10%) and stirred for two hours in order to prepare a homogeneous mixture. The mixture was transferred to a Petri dish and dried in a vacuum oven during the day. From these samples by hot-pressing at the melting temperature of

polypropylene and a pressure of 10 MPa were obtained 100 micron thin film. Cooling of the film after hot pressing was carried out at 3 modes: cooling by liquid nitrogen (cooling rate 20000 /min); cooling in water (cooling rate 200°/min) and the slow cooling under press for 24 hours (cooling rate 20 /min)[4].

2.3. AFM analysis

The morphology of the nanocompositeswas studied using atomic force microscopy Integra Prima (NT-MDT, Zelenograd). For the scan used special silicon cantilevers fabricated by plasma etching method with the needle radius of curvature of 20 nm and the resonance frequency of 1-5 Hz. Scan size was 2×2 mm. The measurements were performed in the semicontact microscopy mode in air, needle change of the cantilever oscillation amplitude was fixed, determining the surface topography. The scanning speed and the number of scanned lines of the imageare respectively 256 and 1,969 Hz

2.4. Method for measuring dielectric properties

The frequency dependences of the dielectric permittivity and dielectric losses tangent were measured at a temperature T = 298 K in the frequency range f = 10^2–10^6 Hz using the dielectric spectroscopy (MNIPIE7-20).

3. Results and discussion:

The influence of the temperature–time mode of crystallization (TTC) on the morphology and properties of the PP+Fe_3O_4 based nanocomposite was also investigated.

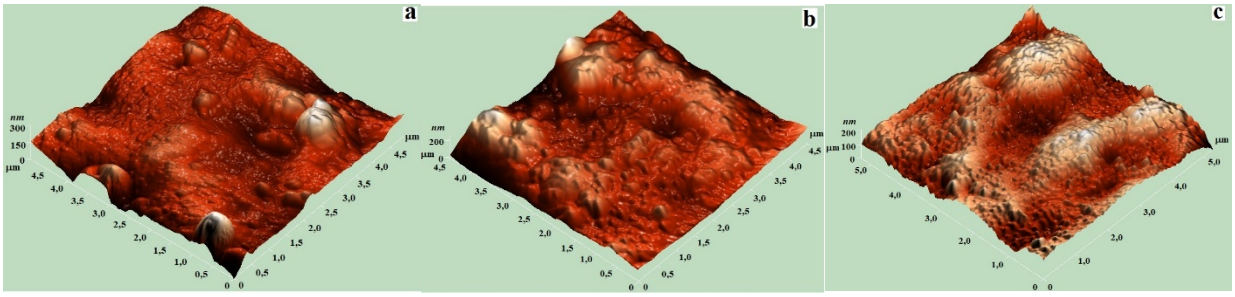

Fig.1. 3D AFM surface images of PP+Fe_3O_4nanocomposites prepared in different TTC mode: a)β=20 °⁄min; b)β=200 °⁄min c) β=2000 °⁄min

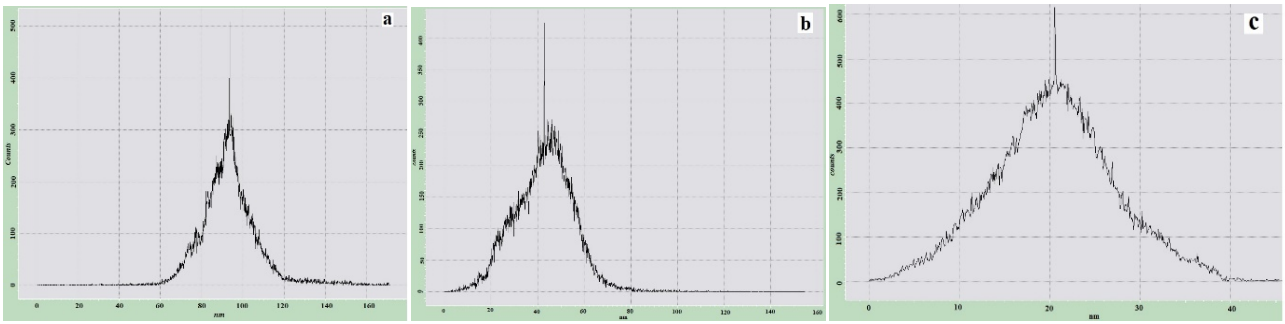

Fig. 2 Histogram of surface roughness of PP+Fe_3O_4nanocomposites prepared in different TTC mode: a)β=20 °⁄min; b)β=200 °⁄min c) β=2000 °⁄min

Fig.1 shows 3D AFM images of PP+Fe_3O_4nanocomposites obtained by different temperature-time mode of crystallization. AFM study shows that the root means square roughness of the PP+Fe_3O_4 samples are 90–95, 40, 20 nm for β=20°/min, 200°/min and 2000°/min cooling rate, respectively(Fig2). It can be concluded from the AFM images that, in samples quenched in liquid nitrogen (β=2000°/min) formed smaller crystallites than in the case of the other two modes. During slow cooling of the alloy, the polymer macromolecules find ways of creating a regular and large supramolecular structure around nanoparticles. With the increase of the cooling rate of the alloy, the polymer macromolecules are without the possibility of to form a regular supramolecular structure and ultimately the structural elements on the surface of the nanocomposite become smaller.

Fig3. shows the dependence of the permittivity (ε) on the frequency for the composite based on PP + Fe_3O_4obtained by different temperature-time mode of crystallization.It can be seen from figure that the dielectric permittivity of the composite rises with the increasing of the cooling rate.It related to the supramolecular structure of the polymer. The dielectric permittivity and dielectric loss tangent of polymer nanocomposites depend on the structure of the

polymer[5]. Dielectric relaxation of polycrystalline polymer-PP depends on its degree of crystallinity. With decreasing amorphous phase of the polymer, the dielectric permittivity and dielectric loss tangent also decrease.

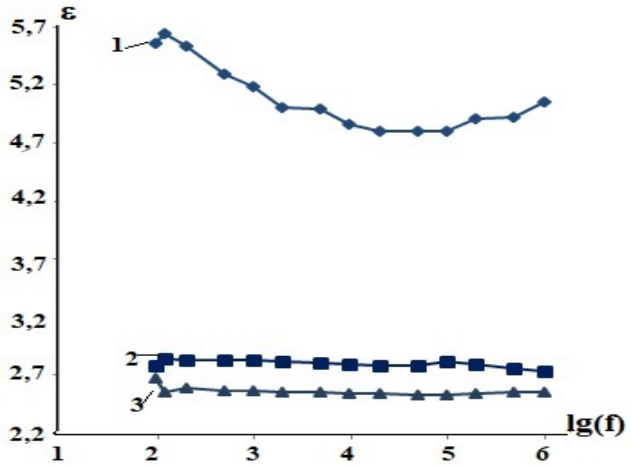

Fig.3. Frequency dependence of the dielectric constant of$PP+Fe_3O_4$nanocomposites prepared in different TTC mode:a)β=2000 °/min; b)β=200 °/min c) β=20 °/min

Previous studies have shown that the degree of crystallization decreases with increasing of cooling rate. This agrees with the value of dielectric permeability, depending on the TTC mode. fig.4 demonstrate frequency dependence of the dielectric loss tangent of $PP+Fe_3O_4$ nanocomposites prepared in different TTC mode. The value of the dielectric loss tangent of the composite increases with the increase in the cooling rate. This result corresponds to the result obtained from theε(β)dependence.

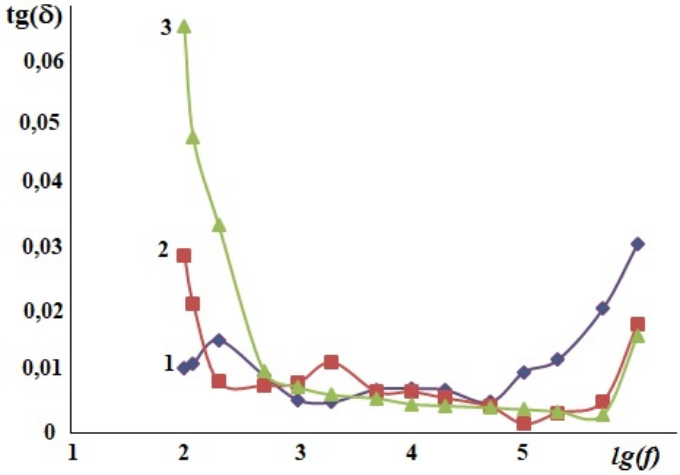

Fig.4. Frequency dependence of the dielectric lost tangent of$PP+Fe_3O_4$nanocomposites prepared in different TTC mode:a)β=20 °/min; b)β=200 °/min c) β=2000 °/min

Depending on the temperature-time mode of crystallization magnetoresistance effect of polymer nanocomposites based on $PP+Fe_3O_4$ was investigated. Fig.5 demonstrates the dependence of negative magnetoresistance of $PP+Fe_3O_4$nanocomposites produced in different TTC mode on cooling rate. The magnetoresistance ratio, defined as:

$$\boldsymbol{\Delta\rho/\rho_0 = [(\rho(H) - \rho(0))/\rho(0)] \cdot 100\%}$$

Here ρ(H) andρ(0) represent the resistivities in the presence and the absence of a magnetic field, respectively. We presented next a summary of the experimental results, given in table 1.

Table1. Depending of magnetoresistance of $PP+Fe_3O_4$ based nanocomposites prepared in different temperature-time modes of crystallization on cooling rate.

Samples	Cooling rate	$\rho_{0(10^{-8})}$	$\rho(H)_{(10^{-8})}$	$\Delta\rho_{(10^{-8})}$	$\Delta\rho/\rho_0$
$PP+7\%Fe_3O_4$	**β=20**	**9,2**	**9,1**	**-0,1**	**-0,011**
$PP+7\%Fe_3O_4$	**β=200**	**9**	**7.2**	**-1.8**	**-0,2**

PP+7%Fe_3O_4	**β=2000**	**9,3**	**4,5**	**-4,8**	**-0,516**

The electrical resistance of the PP+Fe_3O_4 based nanocomposite was found to reduce strongly with increasing cooling rate, under the influence of a magnetic field.

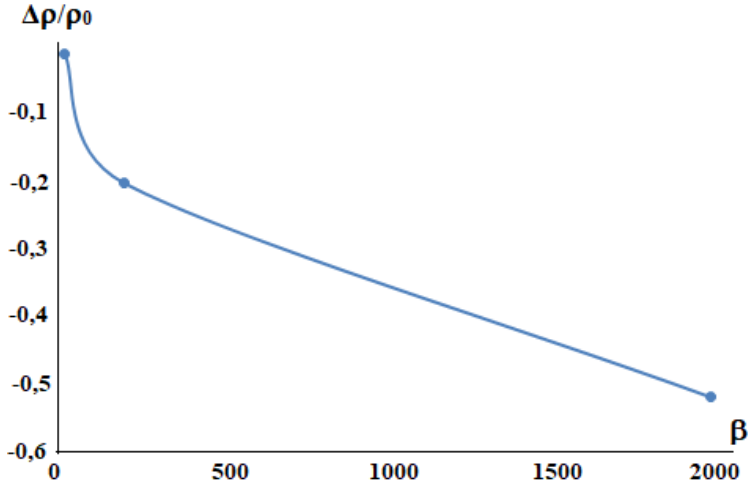

Fig5. The dependence of magnetoresistanceof PP+Fe_3O_4based nanocomposites prepared in different temperature-time modes of crystallization on cooling rate.

The electric conductivity and other electrophysical parameters of the nanocomposites significantly depend on the interphase layer between the matrix and filler. Formation of the conduction channel in the binary nanosystem mostly depends on the interfacial contact area between the two conducting nanograin[6]. As already noted, with an increase in the cooling rate, the size of the structural elements decreases. Reduction of the thickness of the isolator barrier leads to an increase in the number of the charge carriers passing through that barrier under influence of the external magnetic field. Consequently, the electrical resistance of this nanosystem reduced under the external magnetic field.

Conclusion

Polymer-based PP+Fe_3O_4 nanocomposite was obtained in various temperature-time modes of crystallization. The structure of nanocomposites was investigated by AFM. It was found that with the increase of the cooling rate of the nanocomposites grinding of the structural elements are takes place. The dielectric properties of the polymer-based PP+Fe_3O_4 nanocomposite were studied. The dielectric permittivity of the composite rises with the increase of the cooling rate.The dielectric relaxation of polycrystalline polymer-PP depends on its degree of the crystallinity. With the decrease in the amorphous phase of the polymer, the dielectric permittivity and dielectric loss tangent also decrease. Depending on the temperature-time mode of the crystallization the magnetoresistance effect of polymer-based PP+Fe_3O_4 nanocomposites was also investigated. The electrical resistance of the PP+Fe_3O_4 nanocomposite was found to reduce strongly with increasing cooling rate, under the influence of the magnetic field. Reduction of the thickness of the isolator barrier leads to an increase in the number of the charge carriers passing through that barrier under influence of the external magnetic field. Consequently, the electrical resistance of this nanosystem is reduced under the external magnetic field.

Reference

[1] Wendong Wang, Jibao He, Jinke Tang. Journal of Applied Physics 105, 07B105 (2009)
[2] Yun Li, Eok Kyun Lee. 2010 Sixth International Conference on Natural Computation (ICNC 2010)
[3] M. A. Ramazanov, B. Atakishiyeva , M. A. Nuriyev , Sh.Sh.Amirov. Optoelectronics and advanced materials – rapid communications vol. 4, No. 9, September 2010, p. 1387 – 1390.
[4] M. A. Ramazanov, A. M. Maharramov, F. V. Hajiyeva, H. A. Shirinova, Luca Di Palma. Journal of Inorganic and Organometallic Polymers and Materials 28(5).
[5] Edin Suljovrujic, Maja Micic, Dejan Milicevic. Journal of engineered fibers and fabrics 8(3):131-143.
[6] Regina Galceran, Ll. Balcells, Carlos Martínez-Boubeta et al. September 2015 Physical Review B 92(9):094428

PSEUDOSPIN SYMMETRIC SOLUTION OF THE DIRAC EQUATION FOR THE WOODS - SAXON POTENTIAL

J. Z. MAMMADLI, V. H. BADALOV

Baku State University, Z. Khalilov st. 23, AZ-1148, Baku, Azerbaijan
mammadlijala@yahoo.com

Abstract. In the work, the pseudospin symmetric solutions of the radial Dirac equation are studied for the Wood-Saxon potential by using the Pekeris approximation. The energy eigenvalues and radial wavefunctions are found for any k - state via the Nikiforov-Uvarov method. Furthermore, a finite number energy spectrum depending on the depth of the potential V_0, the radial n and the spin - orbit coupling k quantum numbers and parameters R_0, a, C_{ps} are identified as well.

Key words: *Pseudospin symmetry, Wood-Saxon potential, Dirac equation*

1. Introduction

The spin and pseudospin possess the invariant symmetries in the Dirac Hamiltonian. Spin symmetry or spin doublet leads to degeneracy between two states with quantum numbers $(n,l,\ j=l-s)$ and $(n,l,\ j=l+s)$. These two states are considered as a spin doublet with $(n,l,\ j=l\pm s)$. Here $(n,l,\ j)$ and s are radial, orbital angular momentum, total angular momentum, and spin quantum numbers, respectively. The spin symmetry is used to explain the spectrum of antinucleon in a nucleus and small spin-orbit splitting in hadrons. Pseudospin symmetry or pseudospin doublet causes degeneracy between two states with quantum numbers $(n,l,\ j=l+1/2)$ and $(n-1,l+2,\ j=l+3/2)$. These two states are regarded as a pseudospin doublet with quantum numbers $(\tilde{n}=n-1,\tilde{l}=l+1,\tilde{j}=\tilde{l}\mp\tilde{s})$,where $\tilde{l}$ and $\tilde{s}=1/2$ are pseudoorbital angular momentum and pseudospin quantum numbers, respectively. The pseudospin symmetry is used to explain deformation, identical bands, magnetic moment, and effective shell-model in the nuclear structures.

The pseudospin symmetry was studied firstly in non-relativistic framework [1, 2], and then in relativistic mean field theory. There were reported the comprehensive investigations for spin and pseudospin symmetries in the Refs. [3, 4]. An analytical solution of the radial Dirac equation with a physical potential is of paramount importance in relativistic quantum physics since the wave function and its associated eigenvalues contain all necessary information for full description of a quantum system. Hence it would be interesting and important to solve the radial Dirac equation for Woods-Saxon potential in any arbitrary spin-orbit coupling (SOC) number k, since it has been extensively utilized to describe the bound and continuum states of the interacting systems.

Woods and Saxon proposed a potential to describe the distribution of 20 MeV protons on the heavy nuclei, such as platinum or nickel. The Woods-Saxon potential that was widely used to study the nuclear structure within the shell model has received significant attention in nuclear mean field model. In the present work, motivated by the Woods-Saxon potential is of the most realistic short - range potential in physics, the bound state solutions of the Dirac equation for the Woods-Saxon potential with pseudospin symmetry is presented. The standard Woods-Saxon potential [5] is defined by

$$V_{WS}(r)=-\frac{V_0}{1+e^{\frac{r-R_0}{a}}}, \tag{1}$$

where V_0 is the potential depth, R_0 is the width of the potential, a is the surface thickness. Hence, the quasi-exact solution of the Dirac equation is studied for the Wood-Saxon potential under the framework of Nikiforov-Uvarov (NU) method [5]. By using the Pekeris approximation, the bound state energy eigenvalues and corresponding upper and lower radial wave functions are found for arbitrary spin-orbit coupling (SOC) number *k* under pseudospin symmetry.

2. Pseudospin symmetric solution of the radial Dirac equation

In the presence of an attractive scalar $S(r)$ and a repulsive vector $V(r)$ potentials, the Dirac equation for a nucleon with mass M is written as follows

$$[c\vec{\alpha}\cdot\hat{\vec{p}}+\beta(Mc^2+S(r))+V(r)]\psi(\vec{r})=E\psi(\vec{r}), \tag{2}$$

where E is the relativistic energy of the system, $\hat{\vec{p}} = -i\hbar\vec{\nabla}$ is the momentum operator, $\vec{\alpha}$ and β are the 4 × 4 Dirac matrices, while $\vec{\alpha}$ is defined in terms of 2×2 $\vec{\sigma}$ - Pauli spin matrices, and β is described in terms of 2×2 I unit matrices:

$$\vec{\alpha} = \begin{pmatrix} 0 & \vec{\sigma} \\ \vec{\sigma} & 0 \end{pmatrix}, \quad \beta = \begin{pmatrix} I & 0 \\ 0 & -I \end{pmatrix}. \tag{3}$$

For a spherical symmetrical nuclei, the total angular momentum operator $\hat{\vec{J}}$ and spin-orbit coupling operator $\hat{K} = -\beta(\vec{\sigma}\cdot\hat{\vec{L}} + \hbar)$ commute with Dirac Hamiltonian, where $\hat{\vec{L}}$ is orbital angular momentum operator. Then $(\hat{H}, \hat{K}, \hat{\vec{J}}^2, \hat{J}_z)$ can be taken as a complete set of the conservative quantities. Hence, the spinor wavefuncnions can be written according to radial quantum number n and SOC number k as

$$\psi_{nk}(\vec{r}) = \begin{pmatrix} f_{nk}(\vec{r}) \\ g_{nk}(\vec{r}) \end{pmatrix} = \frac{1}{r}\begin{pmatrix} F_{nk}(r)Y^{l}_{jm}(\theta,\phi) \\ iG_{nk}(r)Y^{\tilde{l}}_{jm}(\theta,\phi) \end{pmatrix}, \tag{4}$$

where $F_{nk}(r)$ and $G_{nk}(r)$ are the upper and lower radial wave functions, respectively. $Y^{l}_{jm}(\theta,\phi)$ and $Y^{\tilde{l}}_{jm}(\theta,\phi)$ are the spin and pseudospin spherical harmonics, respectively. The eigenvalues of spin-orbit coupling operator $\hat{K}$ is equal $k = \pm(j+1/2)$, i.e.

$$k = j+1/2 = \begin{cases} l, & (p_{1/2}, d_{3/2}, f_{5/2}, etc.), \quad j = l-1/2\ , \ unaligned\ spin\ \ (k>0) \\ \tilde{l}+1, & (p_{1/2}, d_{3/2}, f_{5/2}, etc.), \quad j = \tilde{l}+1/2\ , \ unaligned\ spin\ \ (k>0) \end{cases} \tag{5}$$

and

$$k = -(j-1/2) = \begin{cases} -(l+1), & (s_{1/2}, p_{3/2}, d_{5/2}, etc.), \quad j = l+1/2\ , \ aligned\ spin\ \ (k<0) \\ -\tilde{l}, & (s_{1/2}, p_{3/2}, d_{5/2}, etc.), \quad j = \tilde{l}-1/2\ , \ aligned\ spin\ \ (k<0) \end{cases}. \tag{6}$$

Substituting Eqs.(3) and (5) into Eq.(2) and by using the following expressions

$$(\vec{\sigma}\cdot\hat{\vec{L}})Y^{l}_{jm}(\theta,\phi) = -\hbar(k+1)Y^{l}_{jm}(\theta,\phi) \tag{7}$$

$$(\vec{\sigma}\cdot\hat{\vec{L}})Y^{\tilde{l}}_{jm}(\theta,\phi) = \hbar(k-1)Y^{\tilde{l}}_{jm}(\theta,\phi) \tag{8}$$

$$\left(\frac{\vec{\sigma}\cdot\vec{r}}{r}\right)Y^{l}_{jm}(\theta,\phi) = -Y^{\tilde{l}}_{jm}(\theta,\phi) \tag{9}$$

$$\left(\frac{\vec{\sigma}\cdot\vec{r}}{r}\right)Y^{\tilde{l}}_{jm}(\theta,\phi) = -Y^{l}_{jm}(\theta,\phi) \tag{10}$$

we obtain two radial coupled Dirac equations

$$\left(\frac{d}{dr} + \frac{k}{r}\right)F_{nk}(r) = \frac{Mc^2 + E_{nk} - V(r) + S(r)}{\hbar c}G_{nk}(r), \tag{11}$$

$$\left(\frac{d}{dr} - \frac{k}{r}\right)G_{nk}(r) = \frac{Mc^2 - E_{nk} + V(r) + S(r)}{\hbar c}F_{nk}(r). \tag{12}$$

By elimating $G_{nk}(r)$ in Eq.(11) and $F_{nk}(r)$ in Eq.(12), two different second order differential equations have been obtained for the upper and lower radial wave functions, respectively

$$\left[\frac{d^2}{dr^2} - \frac{k(k+1)}{r^2} + \frac{(E_{nk} + Mc^2 - \Delta)(E_{nk} - Mc^2 - \Sigma)}{\hbar^2c^2} + \frac{\frac{d\Delta}{dr}\left(\frac{d}{dr} + \frac{k}{r}\right)}{Mc^2 + E_{nk} - \Delta}\right]F_{nk}(r) = 0, \tag{13}$$

$$\left[\frac{d^2}{dr^2}-\frac{k(k-1)}{r^2}-\frac{(Mc^2+E_{nk}-\Delta)(Mc^2-E_{nk}+\Sigma)}{\hbar^2c^2}-\frac{\frac{d\Sigma}{dr}\left(\frac{d}{dr}-\frac{k}{r}\right)}{Mc^2-E_{nk}+\Sigma}\right]G_{nk}(r)=0\,, \tag{14}$$

where $\Delta(r)=V(r)-S(r)$, $\Sigma(r)=V(r)+S(r)$, $k(k+1)=l(l+1)$ and $k(k-1)=\tilde{l}\,(\tilde{l}+1)$.

It should be noted for the Woods – Saxon potential, the above upper and lower radial Dirac equations (13) and (14) cannot solve the analytically in the general case. However, in the case of spin and pseudospin symmetry, the second order differential equations can be solved analytically with Woods-Saxon potential.

In the pseudospin symmetry we obtain: $d\Sigma(r)/dr=0$ or $\Sigma(r)=V(r)+S(r)=C_{ps}=const$.

By substituting the expression $S(r)=C_{ps}-V(r)$ into the Eq. (14), one gets the following form equation:

$$\left[\frac{d^2}{dr^2}-\frac{k(k-1)}{r^2}-\frac{(Mc^2+E_{nk}-2V(r)+C_{ps})(Mc^2-E_{nk}+C_{ps})}{\hbar^2c^2}\right]G_{nk}(r)=0\,. \tag{15}$$

The potential $V(r)$ can be taken as $V(r)=\frac{1}{2}V_{WS}(r)$. It should be noted that this choice for the potential $V(r)$ enables us to reduce the resulting relativistic bound state solutions (relativistic energy spectrum, upper and lower wavefunctions) to their non-relativistic limit under appropriate transformations. Because of the SOC term that is, $V_{so}(r)=\frac{k(k-1)}{r^2}$, the Eq.(15) cannot be solved analytically, except for $k=0$ and $k=1$ cases. Therefore, the following approximation which is called the Pekeris approximation [5] is applied to the SOC term in any arbitrary k state

$$V_{so}(r)=\frac{k(k-1)}{r^2}=\frac{k(k-1)}{R_0^2}\left(C_0+\frac{C_1}{1+e^{(r-R_0)/a}}+\frac{C_2}{(1+e^{(r-R_0)/a})^2}\right), \tag{16}$$

where C_0, C_1, C_2 are constants and their quantities depend on R_0, a, which specific potential parameters were defined as [8-10]:

$$C_0=1-\frac{4}{\alpha}+\frac{12}{\alpha^2}\,,\ C_1=\frac{8}{\alpha}-\frac{48}{\alpha^2}\,,\ C_2=\frac{48}{\alpha^2}\,. \tag{17}$$

After substituting the expression Eq.(16) and the Woods-Saxon potential Eq.(1) into Eq.(15), and new variable of the form $z=(1+e^{(r-R)/a})^{-1}$, it is found as

$$\left[\frac{d^2}{dz^2}+\frac{(1-2z)}{z(1-z)}\frac{d}{dz}+\frac{-\tilde{\mu}^2+\tilde{\nu}^2z-\tilde{\gamma}^2z^2}{z^2(1-z)^2}\right]G_{nk}(r)=0\,. \tag{18}$$

Here

$$\tilde{\mu}^2=\left[\frac{(Mc^2+C_{ps})^2-E_{nk}^2}{\hbar^2c^2}+\frac{k(k-1)}{R_0^2}C_0\right]a^2\,, \tag{19}$$

$$\tilde{\nu}^2=-\left[\frac{2V_0(Mc^2-E_{nk}+C_{ps})}{\hbar^2c^2}+\frac{k(k-1)}{R_0^2}C_1\right]a^2\,, \tag{20}$$

$$\tilde{\gamma}^2=\frac{k(k-1)}{R_0^2}C_2a^2\,. \tag{21}$$

According to the NU-method, the following expression is obtained for defining energy eigenvalues:

$$\tilde{\mu}=\frac{1}{2}\left(n'+\frac{\tilde{\nu}^2-\tilde{\gamma}^2}{n'}\right). \tag{22}$$

Here

$$n'=\frac{1}{2}\left(\sqrt{1+\frac{4k(k-1)a^2C_2}{R_0^2}}-1\right)-n\,, \tag{23}$$

where n is radial quantum numbers, $n=0,1,2,\ldots$.

Substituting the Eqs.(19) - (21) into Eqs.(22), one can find energy eigenvalues E_{nk} as

$$E_{nk}=\frac{1}{2}\left(1+\frac{V_0^2a^2}{4\hbar^2c^2n'^2}\right)^{-1}\left\{-\frac{V_0}{2}\left[1-\frac{a^2}{n'^2}\left(\frac{k(k-1)}{R_0^2}(C_1+C_2)+\frac{V_0}{\hbar^2c^2}(Mc^2+C_{sp})\right)\right]\pm\right.$$
$$\pm\left[4(Mc^2+C_{ps})(Mc^2+C_{ps}+V_0)-\frac{\hbar^2c^2n'^2}{a^2}+\frac{k(k-1)\hbar^2c^2}{R_0^2}\left(4\left(1+\frac{V_0^2a^2}{4\hbar^2c^2n'^2}\right)C_0+\right.\right. \quad (24)$$
$$\left.\left.+2(C_1+C_2)-\frac{k(k-1)a^2}{R_0^2n'^2}(C_1+C_2)^2-\frac{4(Mc^2+C_{ps})(C_1+C_2)a^2}{\hbar^2c^2n'^2}\right)\right]^{1/2}\Bigg\}.$$

Hence, according to the NU method $G_{nk}(z)$ is obtained as the following form for the lower radial Dirac wavefunctions

$$G_{nk}(z)=C_{nk}z^{\tilde{\mu}}(1-z)^{\sqrt{\tilde{\mu}^2-\tilde{\nu}^2+\tilde{\gamma}^2}}P_n^{(2\tilde{\mu},\,2\sqrt{\tilde{\mu}^2-\tilde{\nu}^2+\tilde{\gamma}^2})}(1-2z)\,, \quad (25)$$

where C_{nk} is the normalization constant, $P_n^{(2\tilde{\mu},2\sqrt{\tilde{\mu}^2-\tilde{\nu}^2})}(1-2z)$ is the Jacobi polynomial.

The upper radial wave function $F_{nk}(r)$ can be obtained as:

$$F_{nk}(r)=\frac{\hbar c}{Mc^2-E_{nk}-C_{ps}}\left(\frac{d}{dr}-\frac{k}{r}\right)G_{nk}(r)\,, \quad (26)$$

where $E_{nk}\neq Mc^2-C_{ps}$.

Finally, according to the Eq.(24), the nonrelativistic limit of the energy eigenvalues E_{nk} is in the following form:

$$E_{nl}=\frac{\hbar^2\tilde{l}(\tilde{l}+1)}{2MR_0^2}-\frac{\hbar^2}{2Ma^2}\left[\frac{1}{4}\left(\sqrt{1+\frac{\tilde{l}(\tilde{l}+1)C_2a^2}{R_0^2}}-2n-1\right)-\frac{\frac{2MV_0a^2}{\hbar^2}+\frac{\tilde{l}(\tilde{l}+1)a^2}{R_0^2}(C_1+C_2)}{\left(\sqrt{1+\frac{\tilde{l}(\tilde{l}+1)C_2a^2}{R_0^2}}-2n-1\right)}\right]^2. \quad (27)$$

It should be noted that the Eq. (27) is the same as the energy eigenvalues expression in Ref. [9].

3. Conclusion

In this work we have studied the pseudospin symmetry of the Dirac particles subjected to scalar and vector Woods-Saxon potentials by using the Pekeris - type approximation scheme to the pseudo-centrifugal term for any arbitrary spin-orbit coupling (SOC) number k. The approximate energy eigenvalues and corresponding upper and lower radial functions for bound states have been obtained by the Nikiforov - Uvarov method. The energy eigenvalues depending on V_0, R_0, a and C_{ps} parameters have a finite number of energy spectrum for the Wood-Saxon potential. So, it puts some limitation on the potential parameters during the solution of the bound states within the framework of relativistic quantum mechanics. The nonrelativistic limit of the energy eigenvalues and corresponding eigenfunctions agree with previous ones obtained Ref.[9].

References

[1] Arima, M. Harvey, and K. Shimizu, Physics Letters. B, **30** (8), 517 (1969).
[2] K.T. Hecht and A. Adler, Nuclear Physics A, **137** (1), 129 (1969).
[3] J.N. Ginocchio, Physics Reports, **414** (4-5), 165 (2005).
[4] H. Liang, J. Meng, and S.- G. Zhou, Physics Reports, **570**, 1 (2015).
[5] R.D. Woods and D.S. Saxon, Physical Review **95** (2), 577 (1954).
[6] A.F. Nikiforov and V.B. Uvarov, Special Functions of Mathematical Physics, Birkhäuser, Basel, 1988.
[7] C.L. Pekeris, Physical Review **45** (2), 98 (1934).
[8] V.H. Badalov, H.I. Ahmadov and S.V. Badalov, News of Baku University, 2, 157 (2008).
[9] V.H. Badalov, H.I. Ahmadov, and A.I. Ahmadov, International Journal of Modern Physics E, **18** (3), 631 (2009).
[10] V.H. Badalov, H.I. Ahmadov, and S.V. Badalov, International Journal of Modern Physics E, **19** (7), 1463 (2010).

PARAMETRIC INTERACTION OF WAVES IN METAMATERIALS IN THE SECOND ORDER DISPERSION THEORY

SH. SH. AMIROV [1,3], R. J. KASUMOVA [2] , Z.H.TAGIEV [1] , N.V. KERIMLI [1]

[1]Azerbaijan Medical University , Baku, Azerbaijan , [2]Baku State University Baku, Azerbaijan,[3]Khazar University, Baku, Azerbaijan
phys_med @mail.ru, renakasumovaj@gmail.com

Abstract. A theory of three-wave parametrical amplification in metamaterials is developed in the second order dispersion theory taking into account effects of group velocity mismatch (GVM) as well as group velocity dispersion(GVD) on the wave propagation process . The process of nonlinear interaction of a ultrafast pulse with a longer pulse of high intensity idler wave is considered for the case when refractive index is negative at frequency of signal wave . Analytical expressions for the amplitude, spectral density and energy of signal wave are obtained in the constant field approximation. Effects of GVM and GVD on the spectral density and energy of signal wave are discussed . It was found that at larger nonlinear lengths or when characteristic lengths of group velocity mismatch and group velocity dispersion are less than the nonlinear length of medium the excited pulse is separated into several spikes. In some cases energy transferred from pump and idler waves to the signal wave becomes significantly greater in the presence of GVM and GVD in comparison with the their absence .

Key words: *Metamaterials, non-stationary parametric amplification, dispersion theory, group velocity mismatch, group velocity dispersion*

1. Introduction

The growing interest in nonlinear properties of negative index materials (NIM) is motivated by specifics on the interaction of electromagnetic waves with those materials [1-3] . Distinctly from usual nonlinear media in metamaterials the Poynting vector, characterizing the energy flux has opposite direction to the wave vector. Therefore different signs of refractive index correspond to different frequency intervals of the interacting waves. Therefore the energy fluxes of the waves with a positive sign of refractive index will propagate in opposite direction to those with frequencies corresponding to a negative sign of refractive index. By the authors [4] the generation of harmonics in metamaterials has been studied. Using constant intensity approximation (CIA) [5,6] authors were studied the second and third harmonic generations in the metamaterials. The dynamics of three wave interaction in negative index materials (NIM) was considered for the case of second harmonic generation in [7]. In the works [8,9] the results which are being used for the developments the metamaterials in the near IR and visible ranges of spectrum were obtained. Note that ,metamaterials are characterized with the presence of large losses. By the authors [10] has been proposed the method that has allowed to amplify a signal attenuated due to losses. The feasibility of parametric amplification using three-wave interaction for compensation losses in NIM was considered in [11] . Earlier we have analyzed the efficiency of energy conversions between two direct waves with respect to the energy of the backward signal wave for the case of signal-wave amplification in metamaterials [12] in the constant intensity approximation (CIA), taking into account the reverse reaction of excited wave on the exciting one. By employing the CIA we studied the parametric interaction of optical waves in metamaterials under low-frequency pumping in the case of a negative index at a signal wave frequency [13] .The analytic expressions obtained in CIA showed , that the choice of the optimum parameters for the pump intensity, total length of the metamaterial and phase mismatch will facilitate obtaining the regimes of an effective amplification as well as the generation of signal wave. The process of combination scattering of light in crystals (the analog of parametric processes in NIM) was considered in [14].The characteristic processes observed at parametric interactions of running and counterwaves in metamaterials are the transition processes [15]. Authors analyzed transition processes in the first approximation of dispersion theory[16,17,18] in the medium with quadratic nonlinearity. In case of counter waves the phase matching condition is executed due to opposite directionality of the Poynting vector to the wave vector.Note that the growing interest to the non-stationary interaction of ultra-short pulses of light in nonlinear medium is related to the development of powerful sources of light pulses of femtosecond duration [19,20].Under reduction in the pulse duration the character of interaction of modulated wave significantly depends on the dispersion properties of a medium. To pump the nonlinear crystal of parametrical amplifier the nanosecond pulses of laser radiation are required. Parametric amplification of light in nonlinear crystals can be used for amplification the radiation being used with the aim of optical stochastic cooling of the relativistic heavy ions[21] . Earlier in the work [22] we were studied influence of group velocity mismatch (GVM) as well as group velocity dispersion (GVD) to the generation of sum frequency of ultra- short pulses in an external cavity under the phase matching and absence of

linear losses . It was shown that in some cases efficiency of conversion in the existence of GVM and GVD can be significantly higher as compared as to the absence of mismatch and dispersion. Using the Gaussian pulse with quadratic phase modulation as the input signal pulse led to compression of spectrum with increase in GVM and decrease in GVD. It was obtained that maximum energy of conversion to the sum-frequency is reached not at group phase matching, but at the definite characteristic lengths of GVM and GVD.

Note that earlier we investigated the stationary optical parametric amplification [23] in the constant intensity approximation. Here optimization of various parameters such as the length of the nonlinear medium, wave mismatch, intensities of the pump and idler waves were considered to maximize the signal wave gain.

2. Theory

In the present work we investigate theoretically the non-stationary parametric amplification in metamaterials in the second approximation of dispersion theory by taking into account influence of phase mismatch and linear losses. We study this problem assuming that the nonlinear crystal has length l , and its cross section is much larger than the input laser beam.We ignore any reflections at the crystal surfaces. The beam axis (which we term) is normal to the crystal surface, and this is the direction of the input wave vector. The input surface of the crystal is at $z = l$. During the wave propagation in a nonlinear medium as a result of the nonlinear interaction the energy exchange occurs between the counter wave packets of two types : direct waves (the idler and pump waves) and an backward wave (the signal wave); this leads to the energy transfer from the pump and idler waves into the signal-wave energy. The efficiency of this process is a function of the optimum phase relationship between interacting waves. Violation of this condition leads to a phase mismatch of the waves and as a consequence , to a decrease in the efficiency of parametric amplification. One of the main reasons of the violation of the optimum phase condition is the phase detuning. A change in the phase of interacting waves in a nonlinear medium can be taken into account**.** A weak input field referred to as the signal field (the field with the amplitude $A_1(t,z)$ in our case) becomes amplified through a nonlinear interaction with a powerful pump field (the undepleted field with the amplitude $A_3(t,z)$ in the case considered here) in such a scheme of optical parametric amplification the third field(the field with the amplitude $A_2(t,z)$) is called the idler wave. We have solved the second order dispersion-theory equations for the slowly varying envelope $A(t,z)$of a laser pulse by taking into account the negative values of the dielectric permittivity and magnetic permeability at the signal wave frequency ω_1 and the positive values at the frequencies ω_2 , ω_3 for the pump wave as well as the idler wave. Upon solution the set of reduced equations [19] with the group velocity mismatch and dispersion of group velocities :

$$\left(\frac{\partial}{\partial z}+\frac{1}{u_1}\frac{\partial}{\partial t}-i\frac{g_1}{2}\frac{\partial^2}{\partial t^2}+\delta_1\right)A_1=-i\gamma_1A_3A_2^*e^{i\Delta z}$$

$$\left(\frac{\partial}{\partial z}+\frac{1}{u_2}\frac{\partial}{\partial t}-i\frac{g_2}{2}\frac{\partial^2}{\partial t^2}+\delta_2\right)A_2=-i\gamma_2A_3A_1^*e^{i\Delta z} \quad (1)$$

$$\left(\frac{\partial}{\partial z}+\frac{1}{u_3}\frac{\partial}{\partial t}-i\frac{g_3}{2}\frac{\partial^2}{\partial t^2}+\delta_1\right)A_3=-i\gamma_3A_1A_2e^{-i\Delta z}$$

where A_j (j=1-3) are the corresponding complex amplitudes of the signal, idler and pump waves respectively , δ_j are the absorption coefficients of the medium at frequencies ω_j (j=1-3), u_j are the group velocities of the interacting waves , $\Delta= k_1 - k_2 - k_3$ is the phase mismatch between the interacting waves , $g_j = \partial^2 k_j/\partial\omega_j^2$ (the 3-rd term in the Taylor expansion around the central frequency ω_0: $\Delta\omega = \omega - \omega_0$, $k_n(\omega) \cong k_n(\omega_0) + k_n'\Delta\omega + \frac{1}{2}k_n''\Delta\omega^2 + \cdots$) is the dispersion of group velocities and γ_j are the coefficients of nonlinear coupling . Difference in group velocities is given by $\nu = 1/u_2 - 1/u_1$ and to solve above set the new variable $\eta= t - 1/u_1$ is introduced. If the field at the frequency ω_3 is strong and remains un-depleted in the process of nonlinear optical interaction $A_3(z,t) = A_{30}$, the set of coupled equations contains the amplitudes of the remaining two fields in the non-stationary regime.

$$\left(\frac{\partial}{\partial z}-i\frac{g_1}{2}\frac{\partial^2}{\partial\eta^2}+\delta_1\right)A_1(z,\eta)=-i\gamma_1A_{30}A_2^*(z,\eta)e^{i\Delta z}$$

$$\left(\frac{\partial}{\partial z}+\nu\frac{\partial}{\partial\eta}-i\frac{g_2}{2}\frac{\partial^2}{\partial\eta^2}+\delta_2\right)A_2(z,\eta)=-i\gamma_2A_{30}A_1^*(z,\eta)e^{i\Delta z} \quad (2)$$

Set of equations (2) can be solved by using the Fourier transform method if A (z,ω) is the Fourier transform of A(z, η)

$$A_{1,2}(z,\eta)=\frac{1}{2\pi}\int_{-\infty}^{+\infty}A_{1,2}(z,\omega)e^{-i\omega\eta}d\omega \quad (3)$$

Differentiating equation (3) with respect to η and z, then putting in equation (2) yields the expression for the amplitude $A_1(\omega, z)$ of a signal wave. A spectral density $S_1(\omega, z)$ of an amplified signal wave is found through the amplitude $A_1(\omega, z)$. From the formula obtained for the $S_1(\omega, z)$ it follows that the shape of the spectrum of a signal wave is determined the ratios $\frac{z}{l_{n/l.}}, \frac{l_{n/l}}{l_{GVM.}}$, and $\frac{l_{n/l}}{l_{GVD.}}$. At the larger nonlinear lengths or when characteristic lengths of GVD and GVM are less than the nonlinear length of medium the form of spectrum is complex. The excited pulse is divided into several spikes. In this case the maximum power in the spectrum of parametric amplification does not correspond to the value $\omega = 0$ and a contour of spectrum displaces toward the higher frequencies. When the group velocity is not taken into account maxima of a spectra of the signal wave displace toward greater values of the phase modulation parameter $\omega\tau$ with increase in $\frac{l_{n/l}}{l_{GVM.}}$. All graphs obtained for different values of $\frac{l_{n/l}}{l_{GVM.}}$ intersect each other at a point $\omega\tau = 0$. The idler wave at the input of nonlinear crystal we assume to be Gaussian with the quadratic phase modulation.

$$A_2(t) = A_{20} e^{-\frac{t^2}{2\tau^2} - i\gamma\frac{t^2}{2}}$$

By inverse Fourier transformation it into the frequency domain for the spectrum of a signal wave we get

$$S_2(\omega) = \frac{A_{20}\tau^2}{2\pi} \frac{1}{\sqrt{1+p}} e^{-\frac{\omega^2\tau^2}{1+p}}$$

where $p = \gamma^2\tau^4$ is the coefficient of frequency modulation.

A study of spectral density of a signal wave as a function of phase modulation showed that the spectrum becomes symmetric relatively parameter $\omega\tau$ at greater values of nonlinear length than the l_{GVD} when $\frac{l_{nl}}{l_{GVM.}}$ is zero. In this work we also investigated dependencies of the energy of a signal wave on the parameters such as $\frac{z}{l_{nl.}}, \frac{l_{n/l}}{l_{GVM.}}, \frac{l_{n/l}}{l_{GVD.}}$ and $\omega\tau$. Studies of dependences of energy of a signal wave versus phase mismatch parameter $\frac{\Delta l_{n/l}}{2}$ showed that maximum of energy is obtained not at the value $\frac{\Delta l_{n/l}}{2} = 0$, but it corresponds to definite value of this parameter. Dependences of the energy of a signal wave on the length of metamaterial demonstrate obtaining the maximum energy in the input of the medium.

We have considered parametric amplification of ultrafast pulses in metamaterial by employing second order dispersion theory, which has allowed to take into account influence of group velocity mismatch as well as the group velocity delay on the three-wave interaction. An analytical expressions for the spectral density as well as the energy of a signal wave have been derived . We showed that values of both spectral density and energy of a signal wave are affected by the ratios of characteristic lengths. When $l_{nl}/l_v = 0$, the shape of a plot for the spectral density becomes symmetric relatively ordinate axis and this has the maximum at positive values of phase modulation when $l_{nl}/l_d = 0$. For the ratios of characteristic lengths differ from zero maxima of spectral density are obtained not at zero $\omega\tau$ but at different values of this parameter. It was demonstrated that at the given ratio of l_{nl}/l_d maxima of reduced energy of signal wave displace toward greater values of phase mismatch parameter with increase in the l_{nl}/l_v. It was demonstrated that at the given ratio of l_{nl}/l_d maxima of reduced energy of signal wave displace toward greater values of phase mismatch parameter with increase in the l_{nl}/l_v.

Reference

[1] K. Sarychev and V.M. Shalaev, Electrodynamics of Metamaterials, World Scientific, Singapore, 2007
[2] J. B. Pendry, Phys. Rev. Lett., 85, 3966 (2000)**.**
[3] D.R. Smith, W.J. Padilla, D.C. Vier, et al., Phys. Rev. Lett., 84, 4184
[4] A.K. Popov and V. M. Shalaev, Appl. Phys. B, 84, 131 (2006)
[5] Tagiev Z .H., ChirkinA.S., Sov.Phys. JETP, 46, 669 (1977) [Zh. Eksp. Teor.Fiz. 73, 1271 (1977); TagievZ.H., Kasumova R.J., Salmanova R.A., KerimovaN.V. J.Opt B., 3, 84 (2001)
[6] DmitrievV.G., TarasovL.V., Prikladnayanelineynayaoptika (Applied Nonlinear Optics) (Moscow, Fizmatgiz, 2004), p.352
[7] A.I. Maimistov, I.R. Gabitov and E.V.Kazantseva, Opt. Spectrosk., 102, p. 99 (2007) [Opt. Spectros. (Eng.Transl.), 102, p.90]
[8] Zhang S. et al. Phys. Rev. Lett., 95 (2005)
[9] Cai W., ShalaevV.M. Optical Metamaterials, Fundamentals and Applications (New York, Springer, 2010)
[10] Smalley J. S. T.,ValliniF., Montoya S.A., Ferrari I., Shahin S., Riley C.T., Kante B., FullertionE.E., Liu Z., Fainman Y., Nature Commun., 8, 13793 (2017)
[11] A.K.Popov and Vladimir M. Shalaev, Opt. Lett. 31, 2169-2171 (2006)

[12] R.J. Kasumova, Z. H. Tagiev, Sh. Sh. Amirov, Sh. A. Shamilova and G.A. Safarova, Journal of Russian Laser Research, Vol. 38, No. 4, p.211-218
[13] R.J. Kasumova, Sh. Sh. Amirov, Sh. A. Shamilova, Quantum Electronics 47 (7) p.655-660 (2017)
[14] Popov A.K., Nefedov I.S., et al. Proc. SPIEInt.Soc.Opt.Eng., 8725, 87252E (2013)
[15] Slabco V.V., A.K.Popov, C.A. Myslivets, E.V.Rasskazova, V.A.Tkachenko KvantovayaElectronika 45, No 12 p.1151-1152 (2015)
[16] Popov A. K., Shalaev V.M. Appl.Phys. B, 84 131 (2006)
[17] Shalaev M.I., Myslivets S.A., et al. Opt. Lett., 36, 3861 (2011)
[18] Shadrirov I.V., Zharov A.A.,Kivshar Y.S. J.Opt.Soc.Am.,B, 23, 529 (2006)
[19] Akhmanov S.A. and Khokhlov R.V., Problems of nonlinear optics (in Russian) M., VINITI , 1964, - 295 p.
[20] Akhmanov S.A.,Visloukh V.A., ChirkinA.S. ,UFN 1986 , v. 149, issue 3, p.449-509
[21] Piskarskas A., Stabinis A., Yankauskas A // UFN 1986 , v.150, issue 1, p. 127-143
[22] AmirovSh.,Sh., TagievZ.A. Optika i SpektroskopiyaV.69, issue 3, p.678-683 (1990)
[23] TagievZ.A., AmirovSh.Sh.,Sov. J. Quantum Electron. 19 (11) p.1442-1445

DETERMINATION THE FUNDAMENTAL PARAMETERS OF THE GIANT HR8718 (F5II)

Z. A. SAMEDOV[1,2], S.S.KULIYEVA[2], U.R. GADIROVA[2],

[1]*Baku State University, Baku,*
[2]*Shamakhy Astrophysical Observatory, Azerbaijan*
Zahir.01@mail.ru

Abstract. The atmosphere of the HR8718 (F5II) star is studied by the atmosphere model. The effective temperature T_{eff} of the star and the surface gravity g are determined: T_{eff} = 6800 ± 100 K, logg=4.0. Based on FeII lines the microturbulent velocity is determined: ξt = 3km/sec. In the atmosphere of the star the iron abundances are calculated and compared with the abundance in the Sun. The iron abundance are determined by the comparison of measured from observation and theoretically calculated values of equivalent width FeII. The iron abundance is close to the abundance in the Sun: logε (FeII) = 7.47 ± 0.05.

Key words: *fundamental parameters - stars; chemical composition stars; individual- HR8718 (F5II).*

1. Introduction

In this work the atmosphere of the HR8718 (F5II) star is studied by the atmosphere model. The effective temperature T_{eff} of the star, the surface gravity g in the atmosphere, the microturbulent velocity ξ_t, iron abundances are determined. The synthesis reactions of Hydrogen to Helium are mostly CNO cycles in the the main sequence stars with the temperature $T \geq 15 \cdot 10^6$ K in the nucleus. Evolutionary calculations of stars show that these stars turn into giant, supergiant stars with spectral classes A, F, G after their departure from the main sequence. According to the theory of modern evolution of stars, the process of mixing deep substances occurred in giant, supergiant stars with spectral classes A, F,G. As a result, the products of the C, N, O cycles reaction must be delivered to the atmosphere, and the abundance of elements C,N,O in the atmosphere of these stars should be changed, i.e., the abundance of light elements in giant, supergiant stars with the spectral classes A, F,G should be differ from the abundance of light elements found in matter that are formed by these stars. Thus, the determination of the chemical composition of the atmosphere of giant, supergiant stars with A, F, G spectral classes is an actual problem from the point of view of the evolution of stars.

The giant HR8718 (F5II) were studied by model and parallax methods. The effective temperature, surface gravity, microturbulent velocity and iron abundances in the star atmosphere were determined. Star spectra were obtained by 2 m telescope of the ShAO of ANAS using the Echelle spectrograph with CCD matrix. The spectra are worked out by the DECH-20 program. Equi valent widths of the spectral lines were measured.

2. THE ATMOSPHERIC PARAMETERS. EFFECTIVE TEMPERATURE AND SURFACE GRAVITY

Determination of the effective temperature T_{eff} of the star and surface gravity logg was carried out by the atmospheric model and based on the application of parallaxes described in [1]. The following criteria are considered in the atmospheric model method:

a). Comparison of the observed and theoretically calculated values of the index β.

b). Comparison of the observed and theoretical values of the index $[c_1]$.

c). Comparison of the observed and theoretical values of the index Q.

In the narrow-band four-color uvby photometric system and the UBV photometric system, the indices $[c_1]$ and Q are determined by the formulas $[c_1] = c_1$-0.2(b-y) and Q = (U-B) -0.72 (B-V), respectively. The uvby system was supplemented with a value of β to measure the intensity of the H_β lines. By comparing the values of the above indices found from observations with theoretical values, the values of T_{eff} and logg were determined. The observed values of $[c_1]$, Q and β are found using the catalog [2]. Calculations of color indices in the UBV and uvby systems being necessary to calculate the indices Q and $[c_1]$ were performed by Castelli and Kurucz [3]. Theoretical values of the β-index were taken from Castelli and Kurucz [4].

In addition to the above criteria, the parallax method is used to determine T_{eff} and logg.

d). The use of parallax.

This method is independent on the atmospheric models and has allowed to enhance significantly the accuracy of determination of g. The method is a new and is described in detail in an article by L.S. Lyubimkov et al. [5].

The diagram for determining T_{eff} and logg is shown in Fig.1.

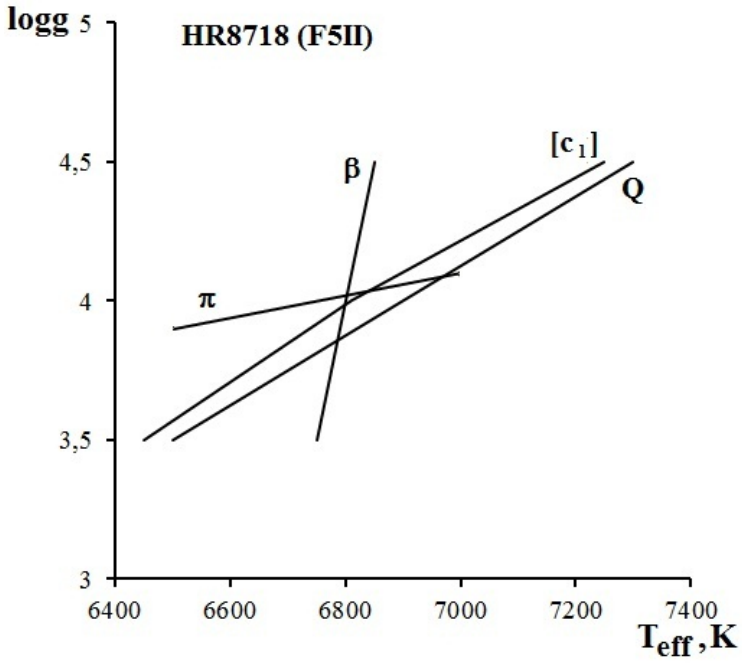

Fig.1. The diagram for determination the parameters T_{eff} and logg of a star HR8718 (F5II).

On the basis of Fig.1 the following values of atmospheric parameters were accepted: T_{eff} = 6800 ± 100 K, logg=4.0. As shown in the catalogs, the star HD8718 is not IIa IV-V of the luminosity class, in accordance with the parameters found for this star. The method that we apply is widely described in [1, 5] and the accuracy of this method is motivated. Therefore, we consider that the results determined by us are more preferable.

3. MICROTURBULENT VELOCITY AND CHEMICAL COMPOSITION

To determine the microturbulent velocity ξ_t it must be a plurality of lines that contain a wide equivalent widths range of the atoms or ions of any given element. The microturbulent velocity ξ_t is chosen such that the abundance of elements determined by the different lines does not change with the increasing of the equivalent widths . The most lines in the studied spectrum are the FeI and then the FeII lines. However, the effect of the LTT extremes to the neutral iron lines is significant. If the calculations are carried out in LTT, the abundance determined on the FeI lines is less than the abundance when refused from LTT [6,7]. Unlike FeI lines there is no effect of the LTT extremes to the the FeII lines. Therefore, in the atmosphere of the star, the microturbulent velocity ξ_t and the iron abundance are determined on FeII lines. As is shown in Lyubimkov and Samedov [8] that the velocity ξ_t increases with the altitude of the height in the the atmosphere of spectral classes stars F. The effect is more effective if the line is stronger. For weak lines, this dependence is not taken into account and it is assumed that the microturbulent velocity ξ_t is constant in the atmosphere of star. Only the weak lines are used when determining the microturbulent velocity ξ_t.

When the ξ_t, is determined we use only sufficiently weak lines. These lines are formed in deep layers, which can be considered as plane-parallel layers in the state of LTE. Based on the Kurucz atmosphere model [9], corresponding to the found parameters T_{eff} and logg, we calculated the logε (FeII) content for several values of ξ_t values. The iron content is determined by comparing the calculated and observed equivalent widths of the FeII spectral lines. We used atomic data from the VALD-2 database for spectral lines [10].

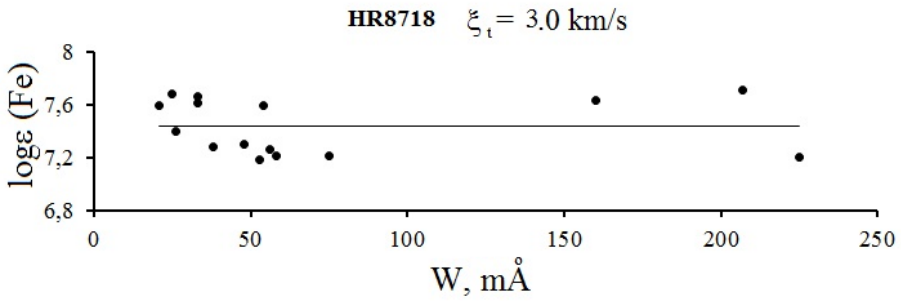

Fig.2. Determination the parameter of microturbulence ξ_t.

As can be seen from Fig.2 on which the logε (FeII) content is plotted as a function of equivalent widths, there is no correlation between logε and W_λ at ξ_t = 3.0 km/s.

When analyzing the microturbulent velocity along FeII lines, the content of iron logε (Fe) is simultaneously determined. $\log\varepsilon_\odot$ (Fe) = 7.45 obtained in [11]. The fundamental parameters of the studied stars: T_{eff} = 6800 ± 100 K, logg = 4.0 ± 0.1, ξ_t = 3.0 km/s, logε (Fe) = 7.47. [Fe/H] = Δlogε = logε (Fe) - $\log\varepsilon_\odot$ (Fe) = 0.02.

It should be noted that the quantity [Fe/H] is often used as an index of the metallicity of a star. This value can be considered as another fundamental parameter, since it characterizes the content of metals in the substance from which the star was formed. It can be seen that the metallicity of the stars considered is close to the solar one. This means that the star considered was formed from a substance with the same metallicity as the Sun.

In the future, we will determine the abundance of light elements on the atmospheric of the star

4. MAIN RESULTS

1. Using the model method the effective temperature T_{eff} of the HR8717 star and the surface gravity g are determined: T_{eff} = 6800 ± 100 K, logg = 4.0 ± 0.1.

2.Based on the FeII lines the microturbulent velocity ξ_t is determined: ξ_t = 3km/sec.

3. In the atmosphere of the star the iron abundances are calculated and compared with the abundance in the Sun. It has been found that the iron abundance is close to abundance in the Sun.

References

[1] L. S. Lyubimkov, «The chemical composition of stars: the method and results of the analysis» NPF Astroprint, Odessa, 323 (1995).
[2] B. Hauck, M. Mermilliod, Astron. Astrophys. Suppl. Ser., **129,** 431 (1998).
[3] F. Castelli, R.L. Kurucz, N.E. Piskunov, W.W. Weiss, D.F. Gray, Astron. Soc. Pac., San Francisco, A20 (2003).
[4] F. Castelli, R.L. Kurucz, Astron. and Astrophys,**454**, 333 (2006).
[5] L.S. Lyubimkov, D.L. Lambert, S.I. Rostopchin, T.M. Rachkovskaya, and D.B. Poklad, Monthly Notices Roy. Astron. Soc. **402**,1369 **(**2010).
[6] A.A. Boyarchuk, I.S. Savanov, Izvestia, **70,** 57 (1985).
[7] F.Thevenin, T. P. Idiart, The Astrophysical Journal, **521**(2), 753 (1999)
[8] L.S. Lyubimkov, Z.A. Samedov. Astrophysics **32**, 49 (1990).
[9] R.L. Kurucz, CD-ROM13, ATLAS9, SmithsonianAstrophys.Obs.(1993).
[10] F.N. Kupka, T. Piskunov, A. Ryabchikova, H.C. Stempels, W.W. Weiss, **138,**119 (1999).
[11] P. Scott, M. Asplund, N. Grevesse, M. Bergemann, and A.J. Sauval, Astron. and Astrophys. **26**, 573 (2015).

SPECTRAL RESEARCHES OF SPECTRAL-BINARY AE/BE HERBIG TYPE STAR MWC 361

H.N.ADIGOZALZADE, U.Z.BASHIROVA

N.Tusi Shamakhy Astrophysical Observatory of Azerbaijan National Academy of Sciences, Y.Mammadaliyev sett., Shamakhy, Azerbaijan, AZ 5626
hadigozalzade@gmail.com

Abstract*:* Results of spectral researches of spectral-binary Be Herbig type star MWC361 is presented. Observational phases are corresponding to the minim of the radial velocity curve of the system. Emission hydrogen lines Hα and Hβ show the low condition of radiation. First time in the spectrum we have discovered diffuse interstellar bands DIB λλ 5780, 5797 Å. For 3 month of observations we have discovered a conciderable increase of relative intensiies of emission lines components of hydrogen and in emission lines Si λλ 6347 6371 Å and [OI] λλ 6300, 6363 Å.

Key words: *Ae/Be Herbig type stars, emission spectrum, circumstellar matter, variability, MWC 361.*

1. Introduction

The Herbig Ae/Be type stars (HAeBe) are pre-main sequence (PMS) objects of intermediate mass 2-10 M and are considered to be the progenitors of Vega type stars, which are surrounded with a residual protoplanetary disks. Spectral monitoring of individual objects has shown that in the spectra of these stars are observed variable emission and absorption lines The same features are also characteristic of classical T Tauri stars. It is known that in young stars, emission lines, as well as some absorption lines, are formed in the circumstellar disks or in the envelopes of the stars. Such circumstellar matter can often participate in accretion, polar outflows, winds and other forms of disk interaction with the central star [1].

Tracking the variation in the observed spectral lines makes it possible to perform diagnostics of the physical processes that are occurring in the stellar atmosphere and in the circumstellar environment. In young stars, in particularly, these processes can directly affect the formation of the planets and their evolution. Consequently, one of the important problems in the study of the early stage of evolution of stars is the study of the characteristics of the circumstellar structure and the processes of interaction of the central star with the surrounding matter. HD 179218 (MWC 614, Sp B9-A2) is an isolated HAeBe type star. Despite the fact that the star is relatively bright comparatively to other HAe stars, it has been studied less. Only when the star was included in the catalog of The et al. [2], it became the subject of active research.

According to the classification of Meeus et al., the spectral energy distribution (SED) of the star belongs to group I, i.e. starting with the infrared band K and further there is an excess of radiation excited in the dust. The profile of the line Hα is consisting of a stable single-peak structure. Perhaps the star has a close companion, about 2.5 arcsec apart. The showed that the star has two dust rings at distances of 1 AU and 20 AU, and the space between from 1 to 6 AU from the star filled with gas. The magnetic field of the star was measured by Hubrig where on the data 2008 they have got about 51 ± 30 G.

The purpose of this paper is to carry out monitoring of the spectral variability of the star on spectral lines obtained in the visual range of spectrum [3].

2.Observations

Spectral observations have been conducted in Cassegrain focus of the 2-m telescope of ShAO of ANAS. Echelle - spectrometer, operating at basis of UAGS spectrograph was used CCD matrix with 530x580 elements was used as a light detector. Observations of program stars were performed in the range of λλ 4700-6700 Å. Spectral resolution is R=14000. Signal- to- noise level in the field of Hα line was S/N=80–100 averagely, but in the field of Hβ line – S/N=10-20. 15 echelle spectrograms of a star were obtained for May-September, 2016. Ismailov and others [have been stated in detail the technique of observations and processing of a material in the work.

Error in intensity measurement due to a continuum depending on the S/N level was 0.5-1% in the region of Hα line and to 2-4% in the region of Hβ line. Value limit of equivalent width which can be measured in a red part of a spectrum is 0.03 Å [4]. The average error in measurements of radial velocities by separate lines in spectra of stellar standards does not exceed ±1.5–2.5 km/s.

According to Altamore et al. (1980) and Baschek et al. (1982) a bright component of MWC 361 (HD200775) system has a spectral class B3Ve. This is one of the brightest Be Herbig type star and it is known as spectral-binary star with the orbital period of about P ≈ 1345 days). Data of six different authors on the solution of radial velocity curves of the system considerably differs from each other that makes it necessary to define radial velocity curves of separate components of the system[8].

3.Results

Our observations were conducted for June-September, 2015 and correspond to 0±0.3 phases on radial velocity curves provided by different authors. In the top line of the table 1 the references to the works of authors are given, the second line presents the phases calculated by us for the elements obtained by these authors; the third line presents the average values of these phases [9]. Such phases of stellar spectrum are of interest for studying separate spectral lines which are formed in close and far parts of circumstellar disk from a central star.

Table 1. Phases of our observations calculated on orbital elements provided by different authors

Author	Pogodin et al. (2004)	Ismailov (2003)	Bisyarina et al. (2015)	Beristy et al. (2013)	Monnier et al. (2006)	Alecian et al. (2008)
Interval	0.988-0.057	0.255-0.335	0.832-0.900	0.734-0.799	0.829-0.897	0.798-0.865
Average	0.026	0.299	0.870	0.769	0.866	0.835

Figure 1 shows the fragments of certain sites of a stellar spectrum. The left low panel contains the site of Si II λ6347, 6371 Å and [OI] 6363 Å emission lines. The spectral site containing forbidden line [OI] 6300 Å is provided in the right top panel. We have detected diffusion interstellar bands (DIBs) λλ 5780 and 5797 Å (the left top panel) in stellar spectrum. Our spectral resolution does not allow separating the structure of separate components of these lines. It is interesting that Pogodin have provided in their work line profiles of Si II λλ 4128, 4131 Å ion which unlike Si II λ6347, 6371 Å lines according to our observations have a pure absorption profile [5].

[OI] λλ6300 and 6363 Å lines are confidently separated from noise. Equivalent widths of [OI] λ 6363 Å line show considerable scatter from an average 0.098 ± 0.056 Å. Average value of equivalent widths of the line is in good agreement with the data of Hernandez. Radial velocities of the line were determined by the shift of emission peak and at the level of a half of intensity. [OI] λ6300 Å line shows diffusion emission with an equivalent width of 0.087 ± 0.033 Å, and any structure in this line as well as in [OI] λ6363 Å line cannot be detected. As seen from the right top panel of fig. 1 that near [OI] λ6300 Å line there are rather intensive telluric lines, the positions of which (O2 λλ 6292.1621, 6295.179, 6305.8101 Å and H2O λλ 6292.6136, 6294.6473, 6302.005 Å) are shown with vertical segments.

On our spectrograms Hα and Hβ line profiles have binary emission peak divided by the central absorption. The general structure of line profiles did not show considerable variations during our observations. However intensity ratio of a blue component to red V/R shows by wavy variation. In fig. 2 the dependency diagram of V/R parameter for Hα and Hβ lines is provided. As it is seen at the beginning of observations intensity ratio of a blue component to red in Hα is about 1, and by the end of a season this ratio became equal to about 1.3, but in Hβ line it is about 2. Such variation occurs for about 90 days.

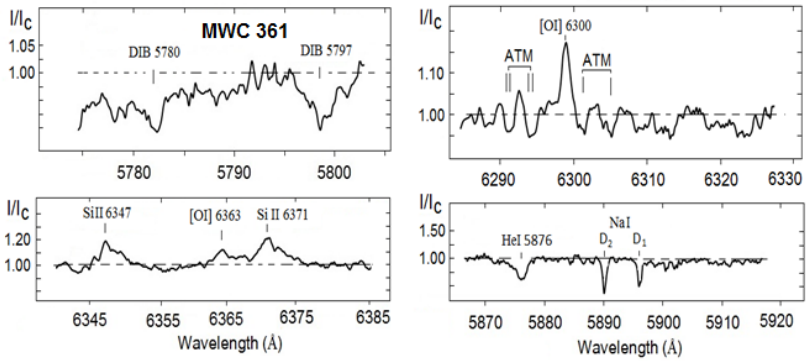

Fig.1. Separate fragments of MWC 361 spectrum.

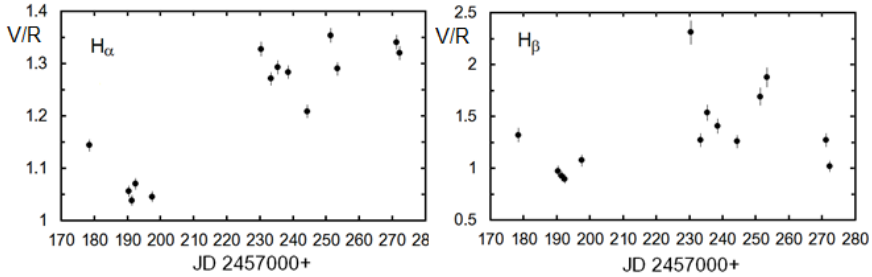

Fig.2. Variation of intensity ratio of blue components to red V/R Hα and Hβ emission lines.

Thus, though the period of a system is rather long (3.68 years), the considerable change of emission intensity in Hα

and an Hβ line is observed for 3 months. More likely, such variations are not related to orbital motion of components.

4. Discussions

To detect the variable structure of Hα line profile first we averaged line profiles and obtained a seasonably average profile on a wavelength to the Sun. Thus, a line shift for orbital motion was not considered, since a line shift must be insignificant for an observed time [10].

Average Hα line profile for all observation intervals is provided on the left panel of fig. 3. Then all line profiles were divided into an average profile by different dates. On the right panel of fig. 3 the residual structure of Hα line profile obtained for each night is provided. Here I – intensity of profiles for each night, Im – intensity of an average profile in this wavelength. It follows that the structure of a residual profile considerably changes by different dates. It is interesting that both at the beginning and at the end of a season the most intensive peaks in a residual profile have shifts from 0 to-45 km/s [6].

After that, we calculated mean-square deviation from an average Σ on residual profiles. Variation of Σ value on wavelength is provided on the left lower panel in fig. 3. Here triple noise factor 3σ of Σ value was drawn with dotted line. As shown here the maximum variation occurs in the central part of a profile, inside interval of about 10 Å. Fig. 4 shows the diagram of radial velocity variation and equivalent widths of separate components of Hα line. Symbols correspond to: Vr1, Vr2 shift of separate emission peaks, Vra – absorption shift between peaks, and Vr1/2 – line shift at the half-intensity level. According to our observations average value of these parameters are -68, 50, -2 and -25 km/s, respectively. As fig. 4 shows radial velocity of separate components of the line showed a fluctuation reaching 20 km/s. The average value of radial velocity at the half-intensity level (bisector velocity) corresponds - 20 km/s. According to the data of Pogodin such velocity occurs in phases 0.0 on a radial velocity curve, drawn on Hα line and photospheric lines. According to Beristi et al. such shift must occur near 0.90P phase [11].

According to us the average value of complete equivalent width of Hα line is about Wλ ~57 Å in scattering from an average to ± 3.41 Å that makes about 5.9% of average value W. Wλ ~57 Å value is minimum as confirmed by the data of other authors. As shown in the work of Pogodin equivalent widths of Hα line for all orbital periods show changes. Our observations showed that, as in relative intensities (fig. 2), small increase in equivalent width is observed after the date of JD2457230.

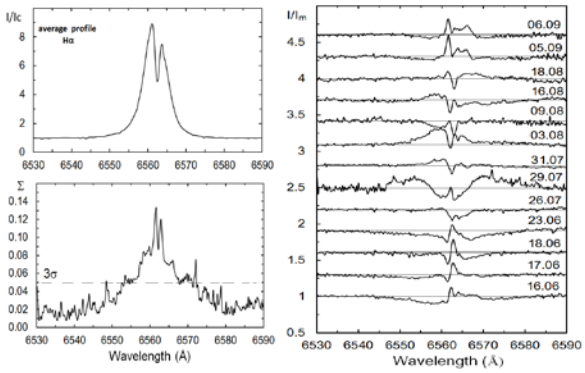

Fig.3. In the top left: averaged Hα profile lines for different nights of observations. Right panel: residual profiles for separate nights of observations, obtained by division of each profile into average.

In the below left:standard shift of Σ of relative intensity I/Im by wavelength for all residual profiles. Here I – profile intensity for every night, Im –average profile intensity at given wavelength. 3σ level shows triple value of mean-square error of measurements of a relative intensity.

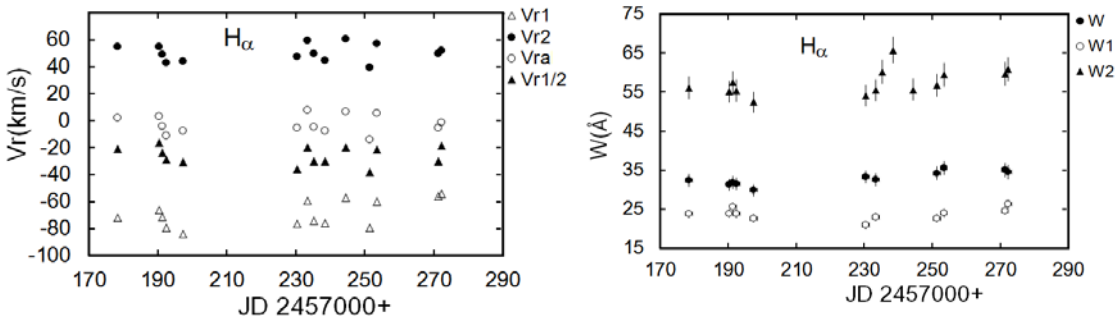

Fig.4. Variation of radial velocities (left panel) and equivalent widths (right panel) of separate components of emission Hα line. Symbols correspond to: Vr1 , Vr2 shift of separate emission peaks, Vra – the shift of the central absorption and Vr1/2 – line shift at half-intensity level, W1, W2 and W – equivalent widths of blue and red components and full equivalent width of emission in Hα.

HeI λ5876 Å line profile is purely absorbing and has no distinction from previous profiles obtained in our observations). As it was noted in Ismailov's work line profile shows variation of steepness and width of a red or blue wing. In spectrograms we observed an expansion in blue wings of the line. Apparently, such variation is related to the orbital motion of components in binary system. Perhaps, the secondary component of the system also gives a certain radiation to helium line. This assumption conforms to the opinion of Bisyarina et al. [6] who think that the second component of the system is also B-star.

5. Conclusion

Thus, our spectral observations on Ae/Be Herbig MWC361 spectral-binary system are interesting with the fact that they have been obtained at a minimum of radial velocity curve. According to different authors the longitude of periastron of the system has values of ω = 200-250° '[6]. At such orientation of an orbit the minimum of radial velocity curve corresponds to the transit time of a star near apastron. The second component of the system is too far from the satellite[7].

Observations show that in some binary T Tauri stars there is an increase in emission activity near periastron which can be the reason of asymmetrical accretion. Beristi assumed that the increase of Hα emission in periastron may result in accretion on a disk of primary component. Perhaps, the main reason for smooth variation of equivalent widths of Hα and Hβ emission lines is perturbation which occurs at the approach of components of the system to periastron. In our case, values of equivalent widths of emission lines of hydrogen are minimum which confirm our assumption.

According to Pogodin values of equivalent widths of Hα line are Wλ (Hα) ≥ 80 Å only in the range of JD 2451800-JD2452250, i.e. for 450 days that makes approximately quarter of the orbital period. The rest of the time Hα line shows a smaller radiant state. Thus, the variation of equivalent widths of a line occurs smoothly. According to Pogodin. borders of a certain time interval of an active radiant state correspond to the interval of 0.977P - 0.312P phases, respectively. As the table 1 shows the phases of our observations enter to this interval, however values of equivalent widths conform to a quiet state. Apparently, the values of a period and elements of an orbit of the system should be defined. As to Bisyarina [6] the last period of a minimum of values of equivalent widths of Hα line corresponds to JD2456600-JD2456800 that corresponds to phases of 0.556P - 0.705P period on Pogodin's elements. In other words, in 2013 - 2014 the minimum emission value of Hα line was observed. Our data of 2015 show the continuation of minimum radiation in this line. We assume that in 2016 increase of equivalent width in Hα emission line, at least, to the level of 2012 is expected (~ 92 Å according to Bisyarina et al. [6].

Observations showed that after JD 2457230 certain variations occurred in circumstellar structure of the star. Intensity ratios of emission components in Hα and Hβ lines increased, the shift of some SiII λλ 6347, 6371 Å emission lines and DIB λλ5780, 5797 Å absorbing bands in a red part of spectrum were detected and their equivalent widths increased at this moment. Beginning from this date radial velocities of [OI] λλ 6300, 6363 Å lines show a shift to a blue part of spectrum. Our results have shown that there is a rapid variability of both emission and absorbing spectrum of a star for about 90 days. This makes only 0.067 part of an orbital period. The reason of such variations can be different processes which are not related to the orbital motion of components, for example, activities in a star (emissions, pulsations), and in a circumstellar disk of components (accretion). Weak variation both in forbidden oxygen lines and in bands of interstellar origin DIB λλ5780, 5797 Å demonstrates the variation of physical conditions in the most external parts of a circumstellar structure [9].

HeI λ5876 Å line is absorbing and traces of emission components in our spectra are not separated. If the system really consists of two B-stars, the total value of equivalent widths of photospheric He lines of separate B-star would be rather constant. In this case the reason of variations in equivalent widths of He line is not totally clear. The asymmetric expansion of blue or red wing of the line at certain moments [12] is not also quite clear.

References

[1] S.H.P., Alencar, G.Basri, "Profiles of Strong Permitted Lines in Classical T Tauri Stars" The Astronomical Journal, Volume **119**, Issue 4, pp. 1881-1900, (2000).
[2] E. Alecian, C. Catala, G. A. Wade, et al., "Characterization of the magnetic field of the Herbig Be star HD200775", Monthly Notices of the Royal Astronomical Society, Volume **385**, Issue 1, pp. 391-403. MNRAS, 385, 391 (2008).
[3] A. Altamore, G. B. Baratta, A. Casatella, et al., "Ultraviolet, optical, and infrared observations of the Herbig Be star HD 200775", Astronomy and Astrophysics, vol. **90**, no. 3, Oct. 1980, p. 290-296. Astron. Astrophys. 90, 290 (1980).
[4] G.Basri, , C. M. Johns-Krull, , & R. D. Mathieu, "The Classical T Tauri Spectroscopic Binary DQ Tau. II. Emission Line Variations with Orbital Phase.", Astronomical Journal v.**114**, pp. 781-792 (1997) Astron.J., 114, 781 (1997).
[5] C. Bertout, G.Basri, J. Bouvier, "Accretion disks around T Tauri stars", Astrophysical Journal, Part 1 (ISSN 0004-637X), vol. **330**, July 1, 1988, p. 350-373. Astrophys.J, 330, 350 (1988).
[6] A. P. Bisyarina, A. M.Sobolev, S. Yu.Gorda, S. Yu. Parfenov, "Optical spectroscopic monitoring of the Herbig Be binary star HD 200775: New maximum of activity and refinement of the orbital period", Astrophysical Bulletin, Volume 70, Issue 3, pp.299-309, (2015) Astrophys Bull., **70**, №3, 316 (2015).
[7] N. Z. Ismailov, "The Herbig Ae/Be Star HD 200775 as a Spectroscopic Binary", Astronomy Reports, vol. 47, Issue 3, pp.206-213, (2003). Astron.Report. **47**, No. 3, 202 (2003).
[8] N.Z.Ismailov, G.R.Bahaddinova, O.V.Khalilov, Kh.M.Mikailov, "Spectral variability of IL cephei", Astrophysical

Bulletin, Volume **68**, Issue 2, pp.196-207, (2013). Astrophys.Bull., 68, № 2, 196 (2013).
[9] V. G. Klochkova and E. L. Chentsov, "The Optical Spectrum of an LBV Candidate in the Cyg OB2 Association", Astronomy Reports, Vol. **48**, Issue 12, pp.1005-1018, (2004). Astron. Rep. 48, 1005 (2004).
[10] K.Malfait, E.Bogaert, C.Waelkens, "An ultraviolet, optical and infrared study of Herbig Ae/Be stars",Astronomy and Astrophysics, v.**331**, pp.211-223 (1998). Astron.Astrophys., 331, 211 (1998).
[11] G.H. Herbig, "The Diffuse Interstellar Bands", Annual Review of Astronomy and Astrophysics, Volume **33**, pp. 19-74. 1995. Ann.Rev.Astron.Astrophys. 33, 19 (1995).
[12] Mikailov Kh. M., Khalilov V. M., and Alekberov I. A., Circl. ShAO **109**, 21 (2005)

DEPENDENCE OF FULL RADIATION FLUX ON TEMPERATURE IN λ>912 Å REGION OF CENTRAL STARS OF PLANETARY NEBULAE

A.H.ALILI, K.I.ALISHEVA

Baku State University, Z. Khalilov Street 23, Baku, AZ1148, Azerbaijan
aynurresul@mail.ru, galaktika2002@mail.com

Abstract: This paper gives detailed information on planetary nebulae. Wide range of literature data was studied and parameters of planetary nebulae were presented in one table. In addition, the parameter characterizing full radiation flux of selected planetary nebulae was determined. More precise Hertzsprung–Russell diagram was plotted for central stars of nebulae.

***Key words**: planetary nebulae, Hertzsprung–Russell diagram, radii of central stars.*

1. Introduction

Study of evolution of planetary nebulae, as well as their central stars is always one of the topical issues of astrophysics. Evolution of these objects directly depends on the evolution of their central stars. For this reason visual study of evolution is the construction of Hertzsprung–Russell diagram for these stars. It is important to specify the luminosity of central stars to determine the evolution sequence of central stars on this diagram.

2. Parameter characterizing radiation flux and Hertzsprung–Russell diagram

The empirical formula for direct determination of radii of central stars was unknown till now. For this reason it was impossible to calculate clearly according to the formula $L = 4\pi R_*^2 \sigma T_*^4$. Luminosity has been approximately calculated indirectly using the expressions:

$$L_{H_\beta} = 4\pi d^2 F(H_\beta)$$

$$L_* = 150\, L_{H_\beta} \quad (1)$$

Here L_{H_β} - luminosity for radiation flux of nebula in line H_β, L_* is luminosity of a central star. Until now, 150 multiplier in the expression (1) was considered the same for all planetary nebulae, and it was probable that its real value could change up to 2 times, and more than twice for cold stars [1,2]. For the first time we have accepted 150 mutiplier as H_Σ in the expression (1) characterizing full radiation flux radiated by nebula in λ>912Å region in a line and continuum:

$$L = 4\pi d^2 H_\Sigma F(H_\beta) \quad . \quad (2)$$

From the other side in the expression

$L = 4\pi R_*^2 \sigma T_*^4$ (3) considering

$$R_*^2 = \frac{2\cdot 10^{-27} n_e^2 \varepsilon R^3 \sum_{i=3}^{\infty} i^2 A_{i2} b_i e^{\chi_i / kT_e}}{T_*^3 T_e^{3/2} \sum_{n=0}^{2} e^{-(n+1)x_0} \left[\frac{x_0^2}{n+1} + \frac{2x_0}{(n+1)^2} + \frac{2}{(n+1)^3} \right]} \quad [3]$$

and $R = d\sin\theta = \frac{d\theta''}{206265''}$ the expression (3) will be

$$L = \frac{1.62\cdot 10^{-46} n_e^2 \varepsilon d^3 \theta^3 T_* \sum_{i=3}^{10} i^2 A_{i2} b_i e^{-\chi_i / kT_e}}{T_e^{3/2} \sum_{n=0}^{2} e^{-(n+1)x_0} \left[\frac{x_0^2}{n+1} + \frac{2x_0}{(n+1)^2} + \frac{x_0}{(n+1)^3} \right]} \quad (4)$$

Considering the expressions (2) and (4) we will obtain

$$d = \frac{7.7\cdot 10^{46} F(H_\beta) T_e^{3/2} H_\Sigma \sum_{n=0}^{2} e^{-(n+1)x_0}\left[\frac{x_0^2}{n+1}+\frac{2x_0}{(n+1)^2}+\frac{x_0}{(n+1)^3}\right]}{n_e^2 \varepsilon \theta^3 T_* \sum_{i=3}^{10} i^2 A_{i2} b_i e^{-\chi_i/kT_e}} \quad (5)$$

If we express with d- sm, $F(H_\beta)$- erq/sm^2·sec., we will obtain

$n_e \varepsilon^{1/2} = \left\{2.33\cdot 10^{41}\left[F(H_\beta)\, t^{0.88}/\theta^3 d\right]\right\}^{1/2}$ and

$$d = \frac{2.33\cdot 10^{41} F(H_\beta) t^{0.88}}{\theta^3 n_e^2 \varepsilon} \quad (6)$$

from (5) and (6) equations we will get

$$H_\Sigma = \frac{3\cdot 10^{-6} t^{0.88} T_* \sum_{i=3}^{10} i^2 A_{i2} b_i e^{\chi_i/kT_e}}{T_e^{3/2} \sum_{n=0}^{2} e^{-(n+1)x_0}\left[\frac{x_0^2}{n+1}+\frac{2x_0}{(n+1)^2}+\frac{2}{(n+1)^3}\right]} \quad (7)$$

Here $x_o = \frac{h\nu_o}{kT_*}$, ν_o – frequency in the border of Lyman series, T_* - temperature of a central star. For 121 planetary nebulae H_Σ full radiation flux was calculated with accuracy of 10^{-2}, it was found that the value of full radiation flux varies in the range of 51÷158. Results are given in table 1.

Table 1.

№	Nebula	T^*	T_e	$F(H_\beta)$, 10^{-12}	d (kps)	H_Σ
1	NGC 6751	105000	10 600	0,27	2	74,89
2	NGC 246	150000	12000	31,56	0,5	90,25
3	NGC 2371	135000	14500	12,11	1,41	83,04
4	NGC 6905	141000	11500	0,22	1,58	86,85
5	NGC 5189	135000	12100	0,16	1,44	84,02
6	NGC 4361	126000	23000	33,76	0,95	80,30
7	NGC 7008	97000	13000	49,52	0,7	70,48
8	NGC 2022	108000	14900	21,04	1,8	73,20
9	NGC 40	38000	10600	713,18	0,8	80,23
10	NGC 1360	105000	18000	65,25	0,38	72,08
11	NGC 1535	80000	11000	54,75	2,1	68,09
12	NGC 2392	80000	14600	115,77	1,5	79,72
13	NGC 2440	188400	15000	178,65	1,36	105,77
14	NGC 2452	100000	12000	13,73	2,84	71,76
15	NGC 2792	130000	14000	115,88	1,9	81,23
16	NGC 2867	141000	8950	78,92	2	89,76
17	NGC 3132	100000	9600	49,66	0,81	73,64
18	NGC 3211	162000	12000	11,40	2,901	95,40
19	NGC 3242	80000	11900	244,57	0,55	67,55
20	NGC 3918	140000	12700	218,57	1,84	85,69
21	NGC 5315	51000	8600	505,82	2	78,81
22	NGC 5882	68000	9400	312,03	1,2	69,30
23	NGC 6210	65000	9600	134,15	1,57	69,59
24	NGC 6445	170000	13 000	916,22	1,39	97,61
25	NGC 6543	60000	7900	481,06	1	73,49
26	NGC 6572	80800	10400	52,80	1,86	68,62
27	NGC 6629	35000	8600	79,84	2	127,87
28	NGC 6720	148000	10700	95,15	0,7	90,47
29	NGC 6741	144400	12600	686,12	1,9	87,55
30	NGC 6778	107200	8000	14,49	1,24	78,26
31	NGC 6790	96 700	12800	88,47	1,13	57,84
32	NGC 6853	135000	12000	383,53	0,38	79,25
33	NGC 6886	164600	13000	24,24	2,6	94,30
34	NGC 7009	87000	7200	207,40	1,45	77,47
35	NGC 7026	130500	9200	94,62	1,5	76,45
36	NGC 7027	175000	8000	363,75	0,89	113,97

№	Nebula	T^*	T_e	$F(H_\beta)$, 10^{-12}	d (kps)	H_Σ
37	NGC 7662	126400	12200	219,08	1,2	65,75
38	IC 418	38800	8900	1153,45	1	124,15
39	IC 1747	126000	10 500	23,52	1,3	75,53
40	IC 2149	42000	10300	65,31	1,52	93,85
41	IC 2165	134000	14600	179,80	1,5	68,53
42	IC 4997	70000	10200	31,56	1,59	82,80
43	IC 5217	95000	10800	6,99	1,02	69,17
44	J 900	116000	12100	5,12	4,3	72,46
45	Hu 1-2	140000	17000	23,15	1,5	70,32
46	NGC 3587	101000	11 600	39,32	0,76	90,62
47	NGC 6302	220000	16100	12817,40	0,74	121,18
48	NGC 6644	125000	12600	10,58	2,1	80,45
49	NGC 6818	145000	13400	79,82	2	88,21
50	NGC 6891	50000	6000	37,07	2,9	87,39
51	NGC 6826	50100	9400	180,30	1,4	79,48
52	IC 351	134000	12000	3,93	1,4	84,46
53	IC 3568	50000	11500	15,65	1,08	77,62
54	J 320	85000	12600	7,46	6,3	68,57
55	He 2-131	33000	10200	71,55	3,67	142,14
56	BD+30	32000	8000	809,10	1	158,51
57	Me 2-1	145000	23000	13,06	2,3	88,25
58	Hb 12	35000	10200	10,92	1	125,84
59	Cn 3-1	64400	7800	12,28	1,5	72,93
60	Ps -1	39000	12000	0,88	10	102,41
61	NGC 2438	114000	10900	21,13	1,2	77,69
62	NGC 6072	140000	11400	65,55	0,57	87,33
63	NGC 6439	80 000	10400	12,41	1,3	69,19
64	NGC 6563	123000	10600	23,01	1,67	81,23
65	NGC 6772	135000	12000	26,61	1,2	84,86
66	NGC 6781	112000	10000	36,63	0,95	77,83
67	NGC 6565	67000	8000	11,80	4,66	72,10
68	NGC 6537	180000	15700	16865,53	3,46	102,74
69	NGC 7293	110000	11000	426,58	0,22	76,21
70	NGC 7354	96000	12000	134,34	1	71,32
71	A 24	137000	12000	5,47	0,53	85,67
72	A 31	85000	12000	36,49	0,48	68,86
73	A 71	123000	11600	20,69	2,8	80,44
74	A 84	100000	12000	4,36	1,68	72,42
75	K 1-22	115000	10200	4,50	1,33	78,68
76	K 2-2	67000	12000	8,39	0,3	68,07
77	Pw -1	94000	12000	22,62	0,37	70,80
78	Jn -1	93000	12000	3,92	0,9	70,55
79	LT -5	150000	12000	0,82	0,5	91,08
80	NGC 1514	60000	14000	64,33	0,54	69,14
81	A 39	160000	12000	1,73	1,81	95,41
82	NGC 2346	100000	13000	25,98	0,9	71,96
83	NGC 6804	85000	10140	3917,42	1,47	70,17
84	NGC 6369	62000	11000	2,77	1,55	69,81
85	NGC 2818	185000	14000	9,38	1,998	106,74
86	NGC 6326	80300	11000	19,93	5,3	64,75
87	NGC 1501	134 500	11500	46,67	1,167	85,01
88	NGC 6567	47000	11510	54,48	3,652	81,82
89	NGC 5979	116000	13885	11,33	1,93	76,80
90	NGC 6578	63000	8250	33,50	3,68	72,52
91	NGC 6803	72900	9700	6,83	0,95	69,40
92	NGC 6842	80000	17300	2,06	2,7	66,98
93	NGC 6884	114800	11000	49,32	2,55	77,89
94	NGC 7048	148000	12600	4,02	1,97	89,86
95	NGC 7094	110000	17700	2,22	1,39	74,29
96	NGC 7139	117000	10300	45,62	2,4	79,30
97	NGC 6881	115000	11400	25,93	1,44	77,66
98	IC 2448	85000	12500	279,77	1,4	68,62
99	NGC 6153	109000	9200	275,04	1,1	77,75

№	Nebula	T^*	T_e	$F(H_\beta)$, 10^{-12}	d (kps)	H_Σ
100	NGC 6894	100000	10200	17,66	1,31	73,75
101	A13	113000	10200	1,47	1,93	77,97
102	A30	66000	11200	0,99	1,12	68,70
103	M1-5	40300	11000	14,61	7,01	98,44
104	Pe1-1	85700	10320	48,06	5,47	70,14
105	Hb5	172000	13000	164,97	1,4	100,09
106	NGC2899	215000	14900	18,96	1,37	119,09
107	Vy1-1	60000	6000	8,46	2,19	79,03
108	IC 1297	91000	10540	18,58	4,1	71,04
109	IC 2003	89900	11000	12,23	2,429	70,45
110	NGC 5307	42900	10700	16,94	3,16	90,94
111	NGC 6620	109648	9600	26,69	6,31	77,44
112	NGC 6309	55000	11300	6,81	2,147	51,65
113	A 33	100000	12800	5,01	1,16	72,04
114	Vy 1-2	118900	9700	3,43	8,13	80,66
115	Vy 2-2	59000	15000	2,95	4,68	69,35
116	M1-14	39900	8800	23,68	4,68	103,02
117	M1-17	96000	10300	4,51	3,11	72,53
118	K 1-2	85000	11000	0,56	3,61	69,47
119	K 1-27	105000	20000	0,24	1,686	72,85
120	NGC 6026	35000	15000	7,26	1,31	121,84
121	Hu 1-1	114000	12000	2,69	1,85	76,92

Thus, full dependence between full flux and temperature was obtained and the dependence is given in figure 1.

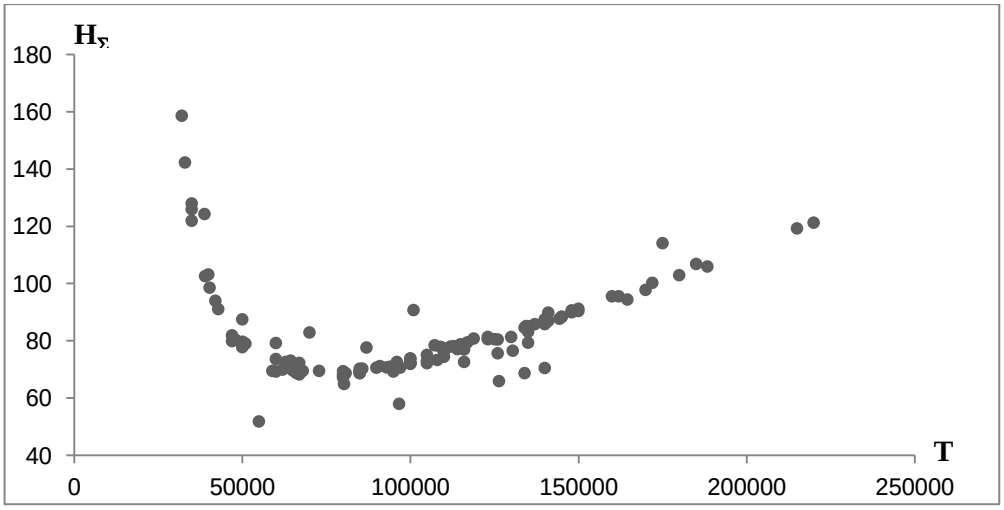

Fig.1. Dependence of H_Σ *full radiation flux on temperatures of central stars of nebulae*

3. Discussion and conclusion

Calculations showed that H_Σ full radiation flux differs from previous constant 150 value tens of times for various nebulae. As seen from the dependence in low temperature ranges H_Σ decreases sharply, then proceeds in the direction of increase [1]. It was shown that constant 150 multiplier is incorrect for nebulae of which the temperatures of central stars are lower than 50000K. Indeed, it varies in a wide range for nebulae on the left of a hole in the graph. For hotter nebulae H_Σ full radiation flux increases as the temperature rises.

References

[1] Zijlstra, A. A. & Pottasch, S. R. Astronomy and Astrophysics (ISSN 0004-6361), vol. 216, no. 1-2, p. 245-252, (1989).
[2] Gesicki K., Acker A., and Zijlstra A. A. A & A no. MS3219, 20 Jan., (2003).
[3] Guseinov R.E., Alisheva K.I. Fizika. 6, 1, p.60-63 (2000)
[4] Acker A., Stenholm B., Tylenda R. and Raytchev B. Astron. Astrophys. Suppl. Ser.90, p.89-101, October (1991).

[5] David J.F. Planetary Nebulae in the Solar Neighbourhood: statistics, distance scale and luminosity function, A thesis submitted to Macquarie University in accordance with the requirements of the degree of Doctor of Philosophy, Department of Physics Division of Information and Communication Sciences Macquarie University, NSW 2109, Australia, July (2008).
[6] Pottasch S.R. and Bernard-Salas J. Astronomy & Astrophysics no evol. 2, v.7. May 19, (2010).
[7] Jacob R., Schönberner D., Steffen M. Astronomy & Astrophysics no 21532, September 18, (2013).
[8] Sterling N. C. and Dinerstein H.L. The Astrophysical Journal Supplement Series, 174:158–201, January (2008).
[9] Martin A.G., Jesus A.T., Juan J.M. and etc. A&A 557, A121 (2013)
[10] Geoffrey C.C., Orsola De M., Jason N. and etc. The Astronomical Journal, June, (2014)
[11] Giammanco1 C., Sale S. E., Corradi1 R. L. M., Barlow M. J. and etc. A & A no.14, July 7, (2010).
[12] Acker A., Marcout J., Ochsenbein F., Stenholm B., Tylenda R. The Strasbourg –ESO Catalogue of Galactic Planetary Nebulae, Part II, (1992)
[13] Phillips J. P. Mon. Not. R. Astron. Soc. 344**,** 501–520 (2003)
[14] Y. Zhang, X.-W. Liu, R. Wesson, P. J. Storey, Y. Liu and I. J. Danziger. Mon. Not. R. Astron. Soc. 351**,** 935–955 (2004).
[15] Gloria Delgado-Inglada and Monica Rodrıguez. The Astrophysical Journal, 784:173 (18pp), April, (2014)
[16] Yu. V. Milanova and A. F. Kholtygin. ISSN 1063-7737, Astronomy Letters, Vol. 35, No. 8, pp. 518–533, (2009).

AN ALTERNATIVE METHOD OF AN ELECTROMAGNETIC FIELD INTRODUCTION INTO A STANDARD MODEL

K.K. MERKOTAN [1], T.M. ZELENTSOVA [1], N.O. CHUDAK [1], D.A. PTASHYNSKYI [1], V.V. URBANEVICH [1], O.S.POTIIENKO [1], V.V. VOITENKO [1], O.D. BEREZOVSKYI [1], I.V. SHARPH [1], V.D. RUSOV [1]

[1] *Odessa National Polytechnic University1, Shevchenko Ave., Odessa, 65044, Ukraine*
sharph@ukr.net

In our opinion, the theory of the electroweak interaction [1-3] has a number of theoretical problems that are accompanied by a certain disagreement with recent experimental results [4-6]. In more detail these problems and disagreements we analyzed in work [7].

On the theory side, from our point of view, the introduction of the electromagnetic field as a linear combination [1-3, 8, 9] leads to essential problems of the Standard Model

$$A_{a_1}(x) = \sin(\theta_W) A_{a_1, g_1=3}(x) + \cos(\theta_W) B_{a_1}(x). \quad (1)$$

Here $A_{a_1}(x)-$ field functions of the electromagnetic field, a_1- a Lorentz index, $A_{a_1,g_1}(x)-$ field functions of the gauge field, that restores the local $SU(2)-$ symmetry, g_1- an internal index, $B_{a_1}(x)-$ a gauge field that restores the local $U(1)-$ symmetry in the Weinberg-Salam-Glashow model, θ_W- a Weinberg angle. The problems, that arise from the introduction of the electromagnetic field in the form of the linear combination of fields (1) with different transformation laws, are associated to the fact, that in this way the electromagnetic field stops being related to a definite group of the Lagrangian transformations. It thus loses the basic physical function of the gauge field, which is to provide the Lagrangian invariance with respect to a certain local symmetry group, since such a function in the Standard Model Lagrangian is performed by the $A_{a_1,g_1}(x)$ and $B_{a_1}(x)$ fields. Let's consider the mentioned problems in detail.

The first problem that accompanies the expansion of (1) is, in our opinion, that the dynamic equations for the electromagnetic field will depend on the gauge choice of the $SU(2)-$ fields. Indeed, a part of the Lagrangian of the electroweak theory containing the field functions of the electromagnetic field can be written as:

$$L_A^{int} = L_A^0 + \sum_{k=1}^{6} L_{A,k}^{int}, \quad (2)$$

where

$$L_A^0 = -\frac{1}{4} g^{a_1 a_{11}} g^{b_1 b_{11}} \left(\frac{\partial A_{b_1}(x)}{\partial x^{a_1}} - \frac{\partial A_{a_1}(x)}{\partial x^{b_1}} \right) \left(\frac{\partial A_{b_{11}}(x)}{\partial x^{a_{11}}} - \frac{\partial A_{a_{11}}(x)}{\partial x^{b_{11}}} \right), \quad (3)$$

$$L_{A,1}^{int} = -\frac{i}{2} e g^{a_1 a_{11}} g^{b_1 b_{11}} A_{a_{11}}(x) \left(\frac{\partial W_{b_1}^{+}(x)}{\partial x^{a_1}} W_{b_{11}}^{-}(x) - \frac{\partial W_{b_1}^{-}(x)}{\partial x^{a_1}} W_{b_1}^{+}(x) \right), \quad (4)$$

$$L_{A,2}^{int} = -\frac{i}{2} e g^{b_1 b_{11}} g^{a_1 a_{11}} A_{a_1}(x) \left(W_{b_{11}}^{+}(x) \frac{\partial W_{a_{11}}^{-}(x)}{\partial x^{b_1}} - W_{b_{11}}^{-}(x) \frac{\partial W_{a_{11}}^{+}(x)}{\partial x^{b_1}} \right), \quad (5)$$

$$L_{A,3}^{int}=\frac{1}{2}e^2g^{b_1b_{11}}g^{a_1a_{11}}A_{a_1}(x)A_{b_{11}}(x)W_{b_1}^{+}(x)W_{a_{11}}^{-}(x), \tag{6}$$

$$\begin{aligned}L_{A,4}^{int}&=\frac{1}{2}e^2ctg(\theta_W)g^{b_1b_{11}}g^{a_1a_{11}}\Big(Z_{a_1}^{0}(x)W_{a_{11}}^{-}(x)W_{b_1}^{+}(x)A_{b_{11}}(x)+\\&+Z_{b_{11}}^{0}(x)W_{b_1}^{+}(x)W_{a_{11}}^{-}(x)A_{a_1}(x)-2Z_{b_1}^{0}(x)W_{a_1}^{+}(x)W_{a_{11}}^{-}(x)A_{b_{11}}(x)\Big),\end{aligned} \tag{7}$$

$$L_{A,5}^{int}=-\frac{1}{2}e^2g^{a_1a_{11}}g^{b_1b_{11}}A_{b_{11}}(x)A_{b_1}(x)W_{a_1}^{+}(x)W_{a_{11}}^{-}(x), \tag{8}$$

$$L_{A,6}^{int}=\frac{i}{4}eg^{a_1a_{11}}g^{b_1b_{11}}\left(\frac{\partial A_{b_1}(x)}{\partial x^{a_1}}-\frac{\partial A_{a_1}(x)}{\partial x^{b_1}}\right)\left(W_{a_{11}}^{+}(x)W_{b_{11}}^{-}(x)-W_{a_{11}}^{-}(x)W_{b_{11}}^{+}(x)\right). \tag{9}$$

Here $e-$ an electromagnetic coupling constant, $a_1,a_{11},b_1,b_{11}-$ Lorentz indices, $g^{a_1a_{11}},g^{b_1b_{11}}-$ components of the Minkowski tensor, $Z_{b_1}^{0}-Z-$bosons field, $W_{a_{11}}^{+}(x)$ and $W_{b_{11}}^{-}(x)-$ functions describing the field of $W-$ bosons:

$$\begin{aligned}W_{a_1}^{+}(x)&=A_{a_1,g_1=1}(x)-iA_{a_1,g_1=2}(x),\\W_{a_1}^{-}(x)&=A_{a_1,g_1=1}(x)+iA_{a_1,g_1=2}(x).\end{aligned} \tag{10}$$

As it is seen from (4-9), the electromagnetic field is included to the interaction Lagrangian with factors that are not invariant under the local $SU(2)-$ transformations. The remaining terms that restore the local $SU(2)\otimes U(1)-$ invariance of the total Lagrangian do not depend on the $A_{a_1}(x)$ field and therefore will not affect the dynamic equations of this field. In addition, the term (9), that can be considered as a term in the Lagrangian of the interaction of the electromagnetic field with the $W^{\pm}-$ boson field, can not be interpreted as the result of the derivative "extension". This is a logical consequence of the introduction of the electromagnetic field (1), because in this way it loses the meaning of the field that establishes the local $U(1)-$ invariance, since in the Weinberg-Salam-Glashow model such a meaning is given to the $B_{a_1}(x)$ field. However, we were not able to find any experimental facts about observations of the quanta of this field. At the same time, in terms of the quantum-mechanical superposition principle, a photon with a probability of $\cos^2(\theta_W)\approx 0.8$ during the measurement can be converted to a state corresponding to a quantum of the $B_{a_1}(x)$ field. In other words, within the Standard Model it remains unclear why the photon and $Z-$boson states are observed in the experiment, and their linear combinations, i.e. the quanta of the fields $B_{a_1}(x)$ and $A_{a_1,g_1=3}(x)$, are not observed, which clearly contradicts the quantum-mechanical superposition principle.

Further, we will try to "return" to the electromagnetic field the status of the field "lost" in the Standard Model, which restores the local $U(1)-$ invariance.

Another problem is related to the transformation law of the electromagnetic field under the local $SU(2)\otimes U(1)-$ transformation. We apply this transformation to the fields that enter into (1). In this case, we denote the set of three $SU(2)-$ transformation parameters as $\vec{\alpha}(x)=(\alpha_1(x),\alpha_2(x),\alpha_3(x))$, and the $U(1)-$ transformation parameter as $\beta(x)$. Let us write the new gauge relation analogous to (1), denoting the corresponding field configurations as well as in (1), but "with a dash":

$$A'_{a_1}(x)=\sin(\theta_W)A'_{a_1,3}(x)+\cos(\theta_W)B'_{a_1}(x). \tag{11}$$

Using the transformation laws of the non-Abelian and Abelian fields, we obtain:

$$A'_{a_1}(x)=\sin(\theta_W)D_{3,3}\left(\vec{\theta}(x)\right)\left(\frac{\partial\theta_3(x)}{\partial x^{a_1}}+A_{a_1,3}(x)\right)+$$
$$+\sin(\theta_W)D_{3,2}\left(\vec{\theta}(x)\right)\left(\frac{\partial\theta_2(x)}{\partial x^{a_1}}+A_{a_1,2}(x)\right)+$$
$$+\sin(\theta_W)D_{3,1}\left(\vec{\theta}(x)\right)\left(\frac{\partial\theta_1(x)}{\partial x^{a_1}}+A_{a_1,1}(x)\right)+ \quad (12)$$
$$+\cos(\theta_W)B_{a_1}(x)+\cos(\theta_W)\frac{\partial\theta(x)}{\partial x^{a_1}}.$$

Here $D_{g_1,g_2}\left(\vec{\theta}(x)\right), g_1,g_2=1,2,3-$ matrix elements of the adjoint $SU(2)$- group representation. Taking (1) into account, we obtain for the electromagnetic field a complex transformation law

$$A'_{a_1}(x)=A_{a_1}(x)+\sin(\theta_W)D_{3,2}\left(\vec{\theta}(x)\right)\left(\frac{\partial\theta_2(x)}{\partial x^{a_1}}+A_{a_1,2}(x)\right)+$$
$$+\sin(\theta_W)D_{3,1}\left(\vec{\theta}(x)\right)\left(\frac{\partial\theta_1(x)}{\partial x^{a_1}}+A_{a_1,1}(x)\right)+ \quad (13)$$
$$+\left(1-D_{3,3}\left(\vec{\theta}(x)\right)\right)\cos(\theta_W)B_{a_1}(x)+$$
$$+\cos(\theta_W)\frac{\partial\theta(x)}{\partial x^{a_1}}+\sin(\theta_W)D_{3,3}\left(\vec{\theta}(x)\right)\frac{\partial\theta_3(x)}{\partial x^{a_1}},$$

which differs significantly from the electromagnetic field transformation law known from the electrodynamics, that is a natural consequence of the presence in (1) of the non-Abelian term. Therefore, there is a question, how the observed values, which are the strengths of the electric and magnetic fields, can be constructed, because for this it is necessary to find expressions that would not depend on either the gauge $SU(2)-$ field or the gauge $U(1)-$ field.

Obviously, it would be possible to require the conservation of the ordinary law of the local transformation for the electromagnetic field, but in this case the relation (1) ceases to be gauge-invariant.

Thus, to introduce an electromagnetic field using the relation (1) without the “destruction” of the well-known and repeatedly verified description of the electromagnetic field, it seems impossible. Therefore, we propose a slightly different approach to the description of the electroweak interaction, which does not “destruct” the usual description of the electromagnetic field.

References

S. Weinberg, Phys. Rev. Lett. 19, 1264 (1967).
A. Salam and J. Ward, Physics Letters 13, 168 (1964).
S. L. Glashow, Nuclear Physics 22, 579 (1961).
S. Chatrchyan et al. (CMS), Phys. Lett. B716, 30 (2012), arXiv:1207.7235 [hep-ex] .
G. Aad, B. Abbott, J. Abdallah, and et al., The European Physical Journal C 76, 6 (2016).
J. R. Andersen et al. (LHC Higgs Cross Section Working Group), (2013), 10.5170/CERN-2013-004, arXiv:1307.1347 [hep-ph] .
K. K. Merkotan, T. M. Zelentsova, N. O. Chudak, et al., (2017), arXiv:1711.01914 [physics.gen-ph] .
L. H. Ryder, Quantum field theory, 2nd ed. (Cambridge University Press, 1996).
D. V. S. Michael E. Peskin, An introduction to quantum field theory, Frontiers in Physics (Addison-Wesley Pub. Co, 1995).

LUMINESCENCE AND PHOTOCONDUCTIVITY OF THE P-GaS / N-InSe HETEROSETER UNDER THE ACTION OF LASER RADIATION

F.M. AKHMEDOVA[1], A.G. QUSEYNOV[1], V.M. SALMANOV[1], R.M. MAMEDOV[1], A.A. SALMANOVA[2]

[1] *Baku State University, Z.Khalilov str.23, AZ-1148, Baku, Azerbaijan*
[2] *Azerbaijan State University of Oil and Industry, 20 Azadliq ave., AZ-1010, Baku, Azerbaijan*

vagif_salmanov@ yahoo.com

Key words: *p-GaS/n-InSe heterojunction, laser, luminescence, photoconductivity.*

Abstract. The photoluminescence and photoconductivity spectra of the p-GaS/n-InSe heterostructure under the action of the Nd: YAG laser were studied experimentally. It is shown that the narrow luminescence lines observed in the spectra with a half-width ~ 10 Å are due to exciton and interband transitions. In n-InSe/p-GaSe heterostructures, after laser irradiation, the increase in photosensitivity is 10^2.

1. Introduction

Semiconductor heterostructures and, especially, quantum wells, filaments and points, are today the subject of intensive scientific research [1]. The GaSe, GaS, and InSe crystals from A^3B^6 semiconductor compounds are ideally suited for this purpose. Since these crystals have a layered structure, and this feature makes it possible to fabricate on their basis samples with a mirror surface and causes the chemical as well as adsorption inertness of the surfaces of natural chips. The samples are not subjected to chemical treatment. They are characterized by a low concentration of various surface states, and the interface of diode structures on their basis is more perfect.

In this paper, the luminescence spectra and the relaxation curves of the photoconductivity of the p-GaSe/n-InSe heterojunction under the action of laser radiation are experimentally studied.

2. Experimental method

The investigated single crystals of p-GaS and n-InSe were grown by the Bridgman method in the horizontal version. The entire growing process was carried out in an automatic mode, which made it possible to obtain perfect single crystals with a natural mirror surface. Samples with a thickness of 10-30 μm and an area of ~1-3 cm^2 were made by shearing from large ingots in the direction parallel to the optical axis. A thin layer of InSe was deposited on the freshly cleaved surface of the sample from GaS by thermal evaporation in vacuum (10^{-5} Torr).

The radiation source was a pulsed Nd: YAG laser with built-in 2nd and 3rd harmonic generators, designed to generate radiation with a wavelength of 1064, 532 and 335 nm. The laser pulse duration was 12 ns with a maximum power of ~ 12 MW / cm^2. The photoluminescence spectra were measured using an automated monochromator with a double dispersion M833 (spectral resolution ~ 0.024 nm at a wavelength of 600 nm) with computer control and a detector recording radiation in the wavelength range 350-2000 nm.

3. Experimental results and their discussion

When the p-GaS/n-InSe heterojunction is excited by the third harmonic of the Nd: YAG laser (eV) from the GaS side (wide-gap window), a luminescence with a maximum of 490 nm is observed (Fig. 1, a). The half-width of the lines is ~ 10 Å. In addition to this line, another line with a maximum of 561 nm is observed in the spectrum (Fig. 1, b).

In the long-wave region of the spectrum, two more lines with maxima λ_3 = 975 nm and λ_4 = 986 nm, respectively, were detected.

The observed radiation lines can be conditionally divided into two particles. The short-wave emission lines with maxima and λ_1 = 490 nm (2.53 eV) and λ_2 = 561 nm (2.21 eV) refer to radiation associated with GaS, and long-wavelength emission lines λ_3 = 975 nm (1.27 eV) and λ_4 = 986 nm (1, 25 eV) refer to a thin InSe film. In our opinion, the short-wave emission line λ_1 corresponds to an optical transition in the region of the edge of the absorption band of GaS, since the width of the forbidden band of GaS is 2.53 eV [2]. Radiation with a maximum λ_2 can be due to an acceptor level located in the forbidden band of GaS with activation energy Ea = 0.37 eV, or Ga vacancy [3]. The existence of two recombination channels, intrinsic and impurity, is also confirmed by the study of the relaxation curves of nonequilibrium photoconductivity (Fig. 2).

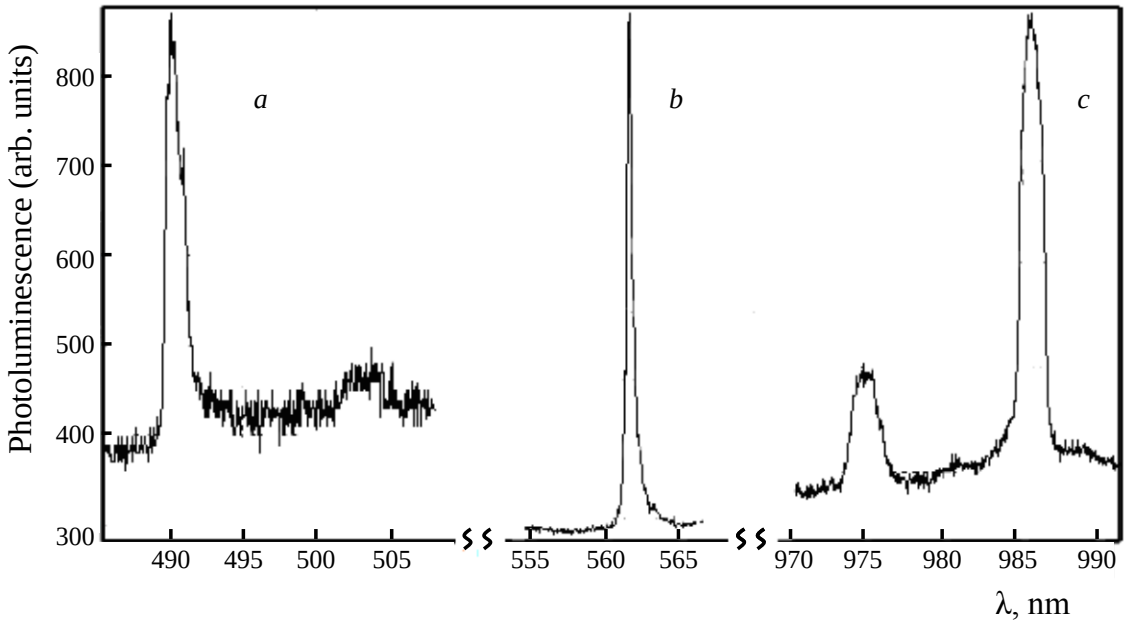

Fig.1. The luminescence spectra of the p-GaS/n-InSe heterojunction at different radiation bands (a, b, c).

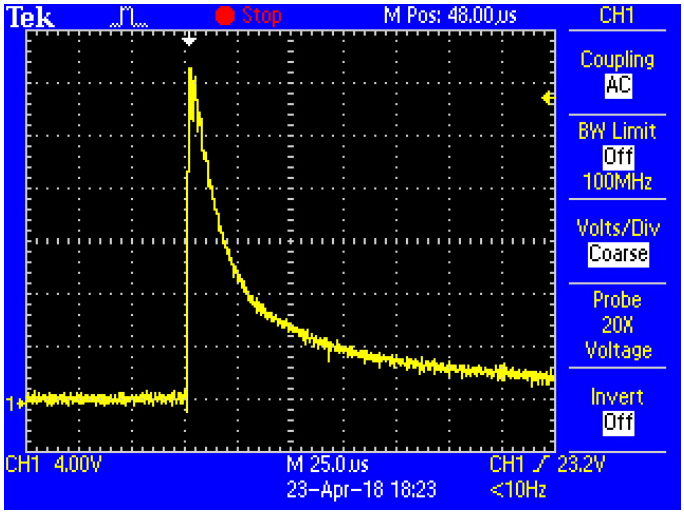

Fig.2. Relaxation of the photocurrent of the p-GaS/n-InSe heterojunction

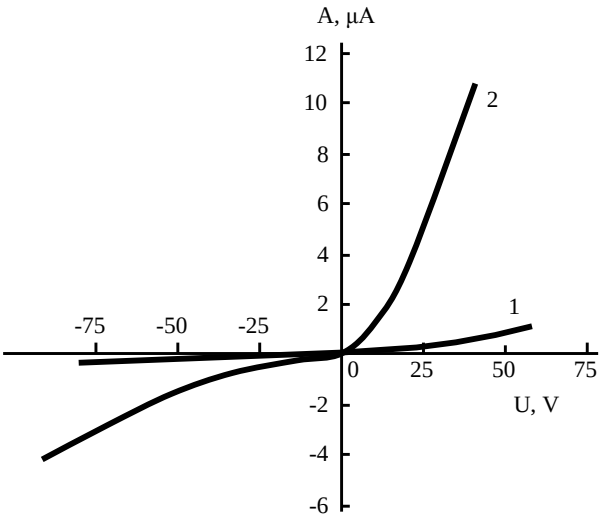

Fig.3.IV characteristic of the p-GaS/n-InSe heterojunction

Relaxation of the photocurrent occurs through fast and slow recombination channels. The fast relaxation time is $\tau \sim 15$ μs, associated with the intrinsic transition, and the slow relaxation time due to impurity excitation with $\tau \sim 200$ μs. As for the long-wavelength emission line related to InSe, rather well-known emission lines associated with an optical band-band transition, $\hbar\omega = 1.27$ eV and annihilation of free excitons, $\hbar\omega = 1.25$ eV, with a binding energy of ~ 20 meV [4].

The p-GaS/n-InSe heterostructure has a diode characteristic, and the rectification coefficient at 2 V is $\sim 2 \cdot 10^2$. As experimental results show at high levels of optical excitation W> 6 MW/cm^2, a significant change in the current-voltage characteristic of the investigated samples is observed (Fig. 3). In both the forward and backward directions, the resistance of the heterostructure increases by two orders of magnitude in comparison with the resistance before laser irradiation. After laser processing, the photosensitivity of the heterostructure also increases by two orders of magnitude.

4. Conclusion

In conclusion, we note that the emission line found at p-GaS/n-InSe heterojunctions with a maximum of 490 nm, with a half-width ~ 10 A^0, can be an effective light source in the blue region of the spectrum. The fast photocurrents observed in the relaxation curves of the nonequilibrium photoconductivity of p-GaS/n-InSe make it possible to state that laser radiation detectors operating at room temperature can be used on their basis.

References

[1] J.I. Alferov. FTP, t.32, 3,(1998)
[2] C.H.Hoa, S.L.Lin. Applied Physics., **v.100**, p.083508 (2006)
[3] Tomoyoshi Aono, Kino Kase, Akira Kinoshita. Applied Physics. v.**74**, p.2818. (1993)
[4] A.G. Kyazim-zade, V.M. Salmanov, A.G. Huseynov, R.M. Mamedov, A.A. Salmanov, F.Sh. Ahmedova. Nanosystems: Physics, Chemistry, Mathematics, **8**(5), p. 1-7, (2017)

PROPERTIES OF $(Au_2S)_n$ NANOPARTICLES ON THE BASIS OF SLATER FUNCTIONS

F. G. PASHAEV, A. G. HASANOV, L. M. AGHAYEVA

Baku State University, Baku, Azerbaijan
faig.pasha55@gmail.com

Abstract. At work geometrical paragmeters of $(Au_2S)_n$ nanoparticles have been defined. By solving equations of molecular orbitals method analitical expressions of molecular orbitals of nanoparticle have been defined. The values of orbital energies have been calculated by computer programs and various properties of nanoparticle have been investigated according to the values of orbital energies.

***Key words*:** *Au_2S, atomic orbital, nanoparticle, orbital energy*

1. Introduction

Properties of nanoparticles depend on its dimensions and the number of atoms of nanoparticle. Several ways have been suggested to find out the number of atoms of nanostructures, which constructed with different type of atoms [1,2]. However, as these ways are complicated, they create some difficulties. Special methods are suggested at work, if the dimensions of nanostructures are known. Au_2S nanoparticle is described as a sphere form.

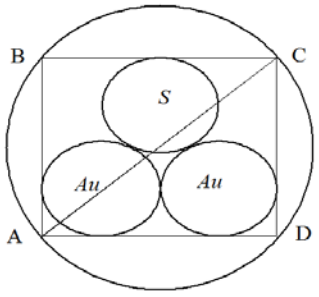

Fig 1. Au_2S compound.

Covalent radiuses of Au and S atoms have been used to define R radius of sphere. r_{Au}=0.134 nm, r_S=0.102 nm. According to the picture;

$$a = AD = 4r_{Au} = 0.536 \text{ nm}$$
$$b = AB = 2r_{Au} + 2r_S = 0.472 \text{ nm}$$

From ΔACD r calculated as below:

$$r = \frac{AC}{2} = \frac{\sqrt{a^2 + b^2}}{2} = 0.357 \text{ nm}$$

Based on tightly packed particles model the value of n in $(Au_2S)_n$ ($R \approx 0.65\ nm$) have been calculated:

$$n = \left(\frac{R}{r}\right)^3 \approx \left(\frac{0.65}{0.357}\right)^3 \approx 6$$

While considering n=6, it is possible to investigate theoretically many quantum-mechanical properties and to configure theoretical model of $(Au_2S)_6$ nanoparticle.

2. Methods

Various properties of multi-electron system can be calculated by applying of molecular orbitals method [3, 4]. Number of total basis functions of $(Au_2S)_6$ nanoparticle is m=534. If the calculations have been carried out on the valence electrons approximation, the number of basis functions is m=72. In order to construct the molecular orbitals of $(Au_2S)_6$ nanoparticle 6s-, $6p_x$, $6p_y$-, $6p_z$- valence atomic orbitals of Au atoms, and 3s-, $3p_x$-, $3p_y$-, $3p_z$- valence atomic orbitals of S atoms have been used as basis atomic orbitals. According to MO LCAO approximation molecular orbitals have been searched as following:

$$U_i = \sum_{q=1}^{m} C_{qi}\chi_q \qquad (1)$$

Here, χ_q – atomic orbitals. As atomic orbitals exponential type Slater or Gauss functions can be used. It has been identified that Slater functions describe the state of electrons in valence region better than Gauss functions [5].

C_{qi} –unknown coefficient, m- is the number of $\mathcal{X}_q = \mathcal{X}_{nlm}(\zeta, r, \theta, \varphi)$ Slater atomic orbitals taken as basis functions.

$$\chi_{nlm}(\xi, r\theta\varphi) = \frac{(2\xi)^{n+\frac{1}{2}}}{\sqrt{(2n)!}} r^{n-1} e^{-\xi r} S_{lm}(\theta\varphi) \qquad (2)$$

Here $S_{lm}(\theta\varphi)$ are real spherical functions. The values of exponential parameter ʒ of Slater atomic orbitals have been calculated by formula given in Ref. [6].

The value of C_{qi} unknown coefficients in (1) expression is calculated by solving equation:

$$\sum_{q=1}^{m} (H_{pq} - \varepsilon_i S_{pq}) C_{qi} = 0 \qquad (3)$$

H_{pq} are matrix elements of Hamilton operator. Wolfsberg-Helmholz approximation has been used for estimate the value of quantity H_{pq}. The analitical expressions which known from literature have been used to calculate S_{pq}- overlap integrals [7, 8]. In order to calculate overlap integrals based on these expressions, the values of principal n-, angular l-, and magnetic m- quantum numbers of Slater atomic orbitals, values of exponential parameters ξ-, Cartesian coordinates of atoms should be known. Computer programs created by authors have been used to solve the equation (3) [9]. By carring out computer calculations orbital enerjies of Au_2S and $(Au_2S)_6$ nanoparticles have been calculated and analitic expresisons of molecular orbitals have been defined.

3. Results and discussions

By using values of ʒ exponential parameters and formula of real Slater atomic orbitals the following analytical expressions have been defined for basis functions.

$$\chi_{6s}(\mathrm{Au}) = \chi_{600}(2{,}599004, \vec{r}) = \frac{1{,}027395}{\sqrt{\pi}} r^5 e^{-2{,}599004r}$$

$$\chi_{6p_x}(\mathrm{Au}) = \chi_{611}(2{,}4812, \vec{r}) = \frac{1{,}3162}{\sqrt{\pi}} r^5 e^{-2{,}4812r} \sin\theta\cos\varphi$$

$$\chi_{6p_y}(\mathrm{Au}) = \chi_{61-1}(2{,}4812, \vec{r}) = \frac{1{,}3162}{\sqrt{\pi}} r^5 e^{-2{,}4812r} \sin\theta\sin\varphi$$

$$\chi_{6p_z}(\mathrm{Au}) = \chi_{610}(2{,}4812, \vec{r}) = \frac{1{,}3162}{\sqrt{\pi}} r^5 e^{-2{,}4812r} \cos\theta$$

$$\chi_{3s}(\mathrm{S}) = \chi_{300}(1{,}87625, \vec{r}) = \frac{1{,}90698}{\sqrt{\pi}} r^2 e^{-1{,}87625r}$$

$$\chi_{3p_x}(\mathrm{S}) = \chi_{311}(2{,}0289, \vec{r}) = \frac{4{,}3438}{\sqrt{\pi}} r^5 e^{-2{,}0289r} \sin\theta\cos\varphi$$

$$\chi_{3p_y}(\mathrm{S}) = \chi_{31-1}(2{,}0289, \vec{r}) = \frac{4{,}3438}{\sqrt{\pi}} r^2 e^{-2{,}0289r} \sin\theta\sin\varphi$$

$$\chi_{3p_z}(\mathrm{S}) = \chi_{310}(2{,}0289, \vec{r}) = \frac{4{,}3438}{\sqrt{\pi}} r^2 e^{-2{,}0289r} \cos\theta$$

Table 1. Orbital energies of Au_2S nanoparticle (in a.u.)

ε_i(i= 1-3)	ε_i(i= 4-6)	ε_i(i= 7-9)	ε_i(i= 10-12)
-0.904186	-0.396359	-0.337629	-0.314327
-0.748882	-0.379641	-0.331995	-0.126112
-0.594769	-0.377323	-0.330904	0.008427

8 valence electrons of Au_2S nanoparticle have been located at two by two levels starting from the lowest energy level. The value of band gap can be calculated as $E_g = \varepsilon_{LUMO} - \varepsilon_{HOMO}$. Here, ε_{LUMO} is the energy of the lowest empty molecular orbital, and ε_{HOMO} is the highest energy of molecular orbital occupied by electrons.

$\varepsilon_{LUMO} = \varepsilon_5 = -10{,}330642$ eV , $\varepsilon_{HOMO} = \varepsilon_4 = -10{,}785566$ eV , $\varepsilon_{LUMO} - \varepsilon_{HOMO} = 0{,}454924$ eV. And this shows that, Au_2S nanoparticle is semi conductive material. The energy of the highest level, occupied by electrons is equal to the value of ionization potential with negative sign. $I_p = -\varepsilon_{HOMO} = -\varepsilon_4 = 10{,}785566$ eV [3]. Strength can be calculate by the formula: $\eta = \frac{1}{2}(\varepsilon_{LUMO} - \varepsilon_{HOMO})$. Consequently, as $\eta = 0.227462\ eV$, $\eta < 1eV$, Au_2S nanoparticle considered as tough material. Au_2S nanoparticle is electrophile, as ε_{LUMO} is negative sign.
The frequency of photon emitted by Au_2S can be calculated as:

$$\nu = \frac{E_g}{h} = \frac{\varepsilon_{\mathrm{LUMO}} - \varepsilon_{\mathrm{HOMO}}}{h} = 1{,}098506241 \cdot 10^{14}\ s^{-1}$$

Table 2. Orbital energies of $(Au_2S)_6$ nanoparticle (in a.u.)

ε_i(i= 1-12)	ε_i (i= 13-24)	ε_i (i= 25-36)	ε_i (i= 37-48)	(i= 49-60)	(i= 61-72)
-0.977024	-0.658313	-0.411676	-0.360713	-0.181731	-0.035657
-0.940721	-0.658288	-0.393306	-0.355716	-0.181447	-0.035327
-0.940606	-0.560542	-0.389456	-0.355702	-0.164165	-0.034471
-0.896197	-0.560430	-0.389436	-0.351717	-0.146484	-0.030728
-0.876511	-0.543308	-0.388218	-0.350038	-0.146169	0.002422
-0.876376	-0.431376	-0.388206	-0.346599	-0.118111	0.002719
-0.853218	-0.431234	-0.367410	-0.346560	-0.117906	0.049369
-0.829279	-0.427413	-0.361896	-0.335380	-0.108848	0.050135
-0.829234	-0.422856	-0.361869	-0.335364	-0.098318	0.075063
-0.700945	-0.420504	-0.361765	-0.320508	-0.098177	0.108658
-0.671057	-0.420460	-0.361184	-0.320460	-0.061589	0.109654
-0.670936	-0.411710	-0.361179	-0.320328	-0.051598	0.144036

$(Au_2S)_6$ nanoparticle has 48 valence electrons. So $\varepsilon_{LUMO} = \varepsilon_{25} = -11{,}202371$ eV., and $\varepsilon_{HOMO} = \varepsilon_{24} = -11{,}203296$ eV. The value of band gap is $E_g = \varepsilon_{LUMO} - \varepsilon_{HOMO} = \varepsilon_{25} - \varepsilon_{24} = 0{,}000925$ eV. And this shows that, $(Au_2S)_6$ nanoparticle is conductive material. The ionization potential: $I_p = -\varepsilon_{HOMO} = -\varepsilon_{24} = 11{,}203296$ eV. Strength: $\eta = 0.0004625$, $\eta < 1eV$, $(Au_2S)_6$ nanoparticle considered as tough material. $(Au_2S)_6$ nanoparticle is electrophile, as ε_{LUMO} is negative sign.
The frequency of photon emitted by $(Au_2S)_6$ is $\nu = 2{,}233602 \cdot 10^{11}\ s^{-1}$

4. Conclusion

As a result of the research we came to conclusion that Slater Atomic Orbitals are useful in the investigation of properties of nanoparticles. As the number of atoms in nanoparticle changes, their properties also changes accordingly.

Reference:

[1] Liu X.Atwater M., Wang J., & Huo Q. Colloids and Surfaces B: Biointerfaces. 2007 Jul 1; 58 (1):3-7.
[2] Ramazanov M.A., Pashaev F.G., Gasanov A.G. et.al. Chalcogenide Letters, vol. 11, No.7, July 2014, p. 359-364.
[3] R. A. Alieva, F. G. Pashaev , K. T. Makhmudov, A.G. Gasanov ISSN 1070-3284, Russian Journal of Coordination Chemistry, 2009, Vol. 35, No. 4, pp. 241–246. © Pleiades Publishing, Ltd., 2009.
[4] Pashaev F.G., Gasanov A.G., Mahmood A.T. J. Nano. Adv. Mat. 2, No. 1, 35-41 (2014)
[5] Abel M. Maharramov, Mahammadali A. Ramazanov, Arzuman G. Hasanov, Faig G. Pashaev 10(3): 1-6, 2016, Article No.PSIJ.23370 ISSN: 2348-0130
[6] Besis N., and Besis G. J. Chem. Phys., 1981, v. 74(6), p. 3628-3631
[7] Guseinov I.I. Int. J. Quantum Chem. 91, 62, (2003)
[8] Pashaev F.G. J. Math Chem (2009) 45:884-890
[9] Arzuman G. Hasanov, Faig G. Pashaev Romanian Journal of Information Science And Technology Volume 19, Number 4, 2016, 331–337

ELECTRICAL PROPERTIES OF FILMS $Cd_{1-x}Zn_xO$ DEPOSITED BY ELETROCHEMICAL WAY

V.J.MAMEDOVA, H.M.MAMEDOV, R.J.KASUMOVA

Physics Department, Baku State University, 23, acad. Zahid Khalilov str.,AZ1148 Baku, Azerbaijan.
mvusala@yandex.com

Abstract. In this paper, the electrical properties of films $Cd_{1-x}Zn_xO$ (x=0.2÷0.9) deposited by electrochemical way, are investigated, depending on the film composition (x) and heat treatment (HT) regime in an oxygen atmosphere. It is established that the no monotonic dependence of the dark resistivity (ρ_d) on x and HT regime is due to changes in the ratio of donor and acceptor concentrations, depending on the film composition. The results are explained on the basis of the energy model for polycrystalline semiconductor films.
Keywords: *electrochemical deposition, oxide films, electrical properties, heat treatment*

1. Introduction

Oxide semiconductors receive considerable attention due to their low cost of fabrication, chemical robustness, high transmittance coefficient and high thermal conductance. Films *of* $Cd_{1-x}Zn_xO$ have received much attentionbecause of their wide applications in the field of optoelectronic and photovoltaic devices. [1-5]. A variety of methods have been reported for the preparation of CdO–ZnO alloy films such as molecular beam epitaxy [6], sol–gel process [7] and spray pyrolysis [8]. Among these methods, electrodeposition is an attractive method to obtain these kinds of films [9], which is well known for its simplicity, reproducibility and possibility of producing cheap large-area films [10-12]. Although pure ZnO and CdO films have been studied by many research groups, a compound semiconductor of ZnO and CdO, that is to say, $Cd_{1-x}Zn_xO$ has seldom been studied.

In this work, we present electrical properties of $Cd_{1-x}Zn_xO$ (with x=0.1÷ 0.9) films depending on the films x and HT regime in oxygen atmosphere

2. Methods and experiments

The electrochemical deposition of $Cd_{1-x}Zn_xO$ films has been performed with a three electrode configuration: graphite electrode as anode, $Ag/AgCl_3$ electrode as reference electrode and *glass*/SnO_2 substrates as cathode [1]. Total area of working electrodes (cathode) was 1×1 cm^2. The *glass*/SnO_2 substrates were cleaned with ethanol, acetone and deionized water and then dried in flowing N_2. At electrodeposition we used aqueous solutions of $Zn(NO_3)_2$ and $Cd(NO_3)_2$ salts (99.5% purities) with different molar fraction in solution (Table 1). The solution were kept on continuous stirring for 1 hour then filtered by filter paper. The solution was homogeneous, clear, transparent and stable at room temperature. The reaction temperature was kept at 80°C.In order to investigate the electrochemistry in the deposition process of $Cd_{1-x}Zn_xO$, cyclic voltammetry study was performed in the potential range of -1.6 to +1.6 V. $Cd_{1-x}Zn_xO$ formation potentials region were registered from cyclic voltammetry curves, and are summarized in Table 1.

The thickness of $Cd_{1-x}Zn_xO$ films were about 1 μm, depending on the deposition duration. All the films showed n-type conductivity. Hall Effect measurements showed that at room temperature the resistivity of films was 1100– 80 Ω·cm and the free electron concentration was $n = 6.5\times10^{17} – 8\times10^{14}$ cm^{-3}, depending on the Zn content. EDS data were recorded to determine the composition of Cd and Zn in deposited layers.

The dark resistivity of films were was measured by using the two-probe method in the temperature range 300–450K by defining an area of 1.0 cm^2 on the film and silver paste was used for good ohmic contacts. Thus, the contact resistance can be negligible. The dark *I–V* measurements were made using dc multimeter.

Table 1. Mole fraction of salts, deposition current and potential for the $Cd_{1-x}Zn_xO$ films.

x	Mole fraction of salts(mM)		Deposition current and potential	
	$Zn(NO_3)_2$	$Cd(NO_3)_2$	J, mA/cm^2	U_c (V)
0.2	1.22	4.88	5.6	-0.96 – -

				1.21
0.4	4.13	6.21	5.1	-0.96 – -1.24
0.5	4.91	4.94	4.2	-0.93 – -1.26
0.6	5.92	3.95	3.4	-0.88 – -1.37
0.7	6.34	2.73	3.2	-0.89 – -1.38
0.8	6.5	1.63	2.7	-0.9 – -1.37
0.9	6.85	0.76	2.4	-0.91– -1.38

3. Results and discussion

The temperature dependence of dark resistivity, were conducted in films $Cd_{1-x}Zn_xO$ just after deposition with different composition. It was found that an increase of zinc concentration up to x=0.6 results to sharp increase of ρ_d. An insignificant change in the dark resistivity is observed, with further increase of x from 0.6 to 0.9. Such dependence of ρ_d on x is most likely indicative of nonmonotonic change in the ratio of N_d/N_a (where N_d and N_a are the concentrations of donors and acceptors, respectively) in films. Note that, the ratio of the photoconductivity to dark conductivity (integral photosensitivity at illumination 100 mW/cm^2) of films at room temperature is about 5-9 (depending on x).

Dark resistivity of all investigated films just after deposition and after the HT (at 600°C for 15 min) is exponentially dependent on temperature: $\rho_d(T) = \rho_0 \exp(E/kT)$ (Fig. 1).

The obtained value of the activation energy (E) of the dark resistivity for films just after deposition was 28-31 eV, which corresponds to the activation energy of desorption of oxygen [11, 12]. It is established that the value of E increases with HT temperature and, at 600°C for 15 minutes, was about 0.34 eV. This energy value, most likely, corresponds to the activation energy of cadmium and zinc vacancies or centers of more complex nature.

It is established that the current-voltage (*I-V*) characteristics of the just deposited films has a complex (nonlinear) form, which depends on the *x*. Thus, at x≤0.6, the *I-V* characteristics of films obeys an exponential (at U < 4 V), and then (at relatively high values of the applied voltage) power law (sublinear region of $I \sim U^m$, with m<1). The sublinear region of the *I-V* characteristics replaced by quadratic region, with an increase of *x*. Further, for films with x≥0.6, a region with an exponential dependence gradually disappears, and value of *m* decreases to *m*=1.

It has been established that the behavior of dark *I-V* characteristics is not monotonically dependent on the HT temperature and duration. At low HT temperatures (at 300-400^{0}C for 15 min), the nonlinear section on the *I-V* characteristics becomes linear. After HT at 600^{0}C for 15 min in oxygen atmosphere, only linear dependence is observed on the *I-V* characteristics. After that, at higher HT temperatures (>600^{0}C), despite a sharp decrease in the dark current, the linear nature of *I-V* characteristics is preserved.

The obtained results are explained on the basis of the energy model for polycrystalline semiconductor films, which can qualitatively explain the main features of various electronic processes in them. It should be noted that the features of the structure of such films determine the mechanisms of current transmission and photosensitivity, which differ from the properties of single crystals. First, because of the rather large value of the ratio of the surface area to the volume, in these films, surface effects play a dominant role. Secondly, after the removal of films from chemical solution to atmosphere, the adsorbed oxygen, due to the presence of intercrystalline pores, forms deep traps (capture levels) for electrons on the surface of individual crystallites.

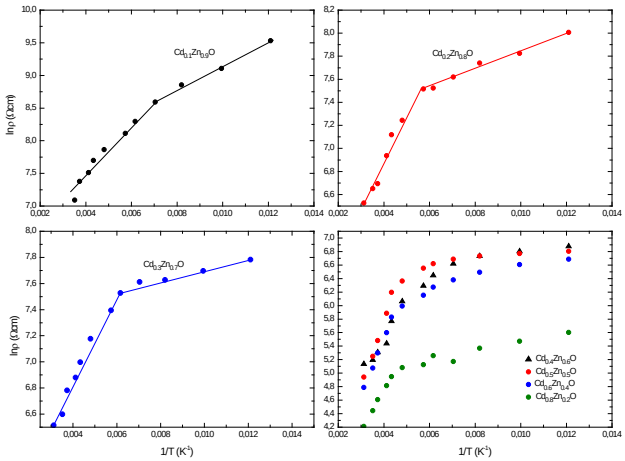

Fig. 1. Temperature dependence of dark resistivity of the $Cd_{1-x}Zn_xO$ films just after deposition.

As a result, potential barriers form at the boundaries of neighboring crystallites. The energy bands of films can be schematically depicted as a set of microcrystallites with potential barriers at the interface with neighboring and various types of local levels (trapping and trapping centers sensitizing, recombination, scattering). This is entirely permissible and is caused by the complex chemical compositions of the initial materials, the nature of the deposition process, and so on. According to this model, the film resistance as a whole consists of the sum of the resistances of individual crystallites and barriers. Therefore, changes in conductivity under the influence of any action (for example, changes in film composition, temperature, HT regime, light, injection, etc.) in addition to the change in the concentration of free carriers can also be caused by a change in their effective mobility, due to the modulation of the height and width of potential barriers . Naturally, both of these, under certain conditions, can provide a transfer of carriers between the crystallites. In this case, an important role is played also by the small thickness of the films. It should be taken into account that in polycrystalline films the crystallite sizes are usually small (30-200 nm) in comparison with the diffusion displacement length. According to SEM studies, as already noted, the crystallite sizes after HT significantly (almost 20-50 times) increase. Naturally, change in the composition and HT regime of the films can purposefully vary the main parameters of adhesion levels and micro crystallites, as well as interlayers and potential barriers between them. Within the framework of this model, a decrease of σ_d after HT, in comparison with the values in non-heat-treated films, can be explained directly by a change in the number of adsorbed oxygen molecules. The concentration of oxygen molecules adsorbed on the surface decreases with increasing annealing temperature. However, this decrease occurs not only due to desorption of oxygen molecules. If some part of this decrease in the concentration of oxygen molecules is associated with desorption, the other part is due to their decay into atoms, which play the role of capture centers for minority carriers (holes). In the general case, a decrease in the concentration of oxygen molecules after HT leads, first, to a decrease in the height of the barriers; secondly, to an increase in the ratio of the concentration of centers of various types; thirdly, to an increase in the density of capture centers of minority carriers. The capture of minority carriers by oxygen atoms leads to a decrease of σ_d with respect to the initial value. However, the rate of recombination of the main carriers also decreases. Therefore, after that, the photoconductivity increases with respect to the initial one.

Conclusion

Thin films of $Cd_{1-x}Zn_xO$ (x=0.2÷0.9) were deposited by electrochemical way. It has been established that regulating composition and HT regime can be specifically control the electrical parameters of $Cd_{1-x}Zn_xO$films.The results are explained on the basis of the energy model for polycrystalline semiconductor films.

Reference

[1] H.M.Mamedov, S.I.Shah, A.Chirakadze, V.U.Mammadov, V.J.Mammadova, Kh.M. Ahmedova, Photonics Letters of Poland, **10**, 26 (2018).
[2] H.M.Mamedov, V.U.Mammadov, V.J.Mammadova, Kh.M. Ahmedova,Journal of Optoelectronics and Advanced Materials, **17**, 67 (2015).
[3] R. J. Kasumova, N.V. Kerimova, V.J. Mamedova, Journal of Nonlinear Optical Physics & Materials, **26**, 1750019 (2017).
[4] Y. Caglar, M. Caglar, S. Ilican and A. Ates, J. Phys. D: Appl. Phys., **42**, 065421 (2009).
[5] F. Wang, Z. Ye, D. Ma, L. Zhu and F. Zhuge, J. Cryst. Growth, **283,** 373 (2005).
[6] S. Sadofev, S. Blumstengel, J. Cui, J. Puls, S. Rogaschewski, P. Schafer and F. Henneberger, Appl. Phys. Lett., **89**,201907 (2006).

[7] G. Torres-Delgado, C.I. Zuniga-Romero, O. Jimenez-Sandoval, R. Castanedo-Perez, B. Chao and S. Jimenez-Sandoval, Adv. Funct. Mater.,**12,** 129 (2002).
[8] H. Tabet-Derraz, N. Benramdane, D. Nacer, A. Bouzidi and M. Medles, Sol. Energy Mater. Sol. Cells**, 73,** 249 (2002).
[9] M. Tortosa, M. Mollar and B. Marı, J. Cryst. Growth, **304**,97 (2007).
[10] H. Mamedov, Z. Konya, M. Muradov, A. Kukovecz, K. Kordas, D. Hashim, V. Mamedov, J. Solar Energy Engineering, **136**, 044503 (2014).
[11] Abdinov, H. Mamedov, and S. Amirova, Thin Solid Films, **511**-**512**, 140 (2006)
[12] Abdinov, H. Mamedov, S. Amirova, Jpn. J. Appl. Phys.,**46**, 7359 (2007).

THE INFLUENCE OF THE CORONA DISCHARGE ON THE DIELECTRIC AND LUMINESCENT PROPERTIES OF POLYMER NANOCOMPOSITES BASED ON POLYPROPYLENE AND SILVER SULPHIDE NANOPARTICLES

S. G. NURIYEVA, M. A. RAMAZANOV

Baku State University, AZ 1148, ZakhidKhalilov Str. 23, Azerbaijan,
e-mail: aliyeva-s@list.ru

Abstract. This paper involves using a combination of two synthetic methods for preparation of nanocomposites (PP/Ag2S) based on polypropylene and silver sulphide by application of ultrasound and microemulsion techniques. The morphology of the nanocomposite and the distribution of silver sulphide nanoparticles in the polymer matrix were studied by scanning electron microscopy. The influence of corona discharge on the luminescence and electrophysical properties of PP/Ag2S nanocomposites has been studied. It was found that after polarization under the corona discharge, the intensity of the luminescence and the dielectric permittivity of PP/Ag2S nanocomposites increase. It was explained by the formation of traps for electrical charges in the polymer matrix.

***Key words*:** *nanocomposite, corona discharge, dielectric properties, luminescence properties, silver sulphide nanoparticles.*

1. Introduction

Nanocomposites consisting of the polymer which structure was modified with the help of different physical methods and semiconductor nanoparticles which sizes are comparable with the mean free pass of the electron, perspective materials that can find its application in the different field of science and technology.

There are various simple physical-technological methods of surface processing of PNCs: electric discharge, corona discharge, modification with gamma rays, thermal treatment and etc. All these modifications cause certain changes, resulting in the formation of the active groups in the composite material. All these factors change some of the properties of the material. The study of modified nanocomposites has proven to have a positive effects [1-4].

Corona discharge treatment of polymer nanocomposites can cause to the increasing their surface energy.We would like to note that in this case only the surface layer of the macromolecule is modified which leads to improvement of their hydrophilic properties and adhesion ability. Also, the electrons generated during corona discharge, impact the polymer film with energies that are enough to break the molecular bonds on the surface. The resulting polar groups on the surface, primarily hydroxyl, carbonyl and carboxyl groups enhance the chemical activity of the polymer matrix. It can increase the strength of the polymer.

Active groups of polymer material change the molecule structure of the polymer due to the high voltage field. The deformation of the structural molecules leads to the formation of traps for electric charge in the polymer material. These traps deteriorate the electro-technical properties of the insulating process by changing the supramolecular structure. As a result of oxidation and structuring, the reactivity of the polymer chain increases. Structuration is the result of the interaction of the external field and the interior of the neighboring macromolecules[5-7].

This paper presents a combinational method for the synthesis of nanocomposite PP/Ag_2S based on polypropylene and silver sulphide, also was studied the effect of corona discharge on the dielectric and luminescence properties of polymer nanocomposites based on PP/Ag_2S.

Reagents

Reagents used for research: isotactic polypropylene powder (M 250000), $AgNO_3$– silvernitrate, Na_2S-sodium sulphide , $C_6H_5CH_3$ toluene, $C_{12}H_{25}SO_4Na$–sodium lauryl (dodecyl) sulphate, H_2O-distilled water.

For obtaining of PP/Ag2S nanocomposite samples the combination of ultrasonic and microemulsion methods were used [8].

The polarization of nanocomposites was carried out with the help of corona discharge. Corona discharge is realized with the help of needle-plane electrodes. The diameter of the needles is approximately 0.3 mm, and the distance between the needles and the substance was 1 cm. The charging voltage is $U_к \approx$6-9 kV, the charging time is 5-10 min. The thickness of the samples is 100 μm. Before beginning of the experiment, the samples were thoroughly degreased. After

that, thin films were placed on a grounded electrode and charged at a voltage of 6 kV by a negative corona through a system of metal needles vertically spaced 6×10-3 m from the surface of the sample.

The XRD diffractograms of nanocomposites were examined by diffractometer Rigaku Mini Flex 600s using the X-ray tube with the copper anode (Cu-Kα radiation, 30 kV and mA) at room temperature.

The distribution of silver sulphide nanoparticles in the polymer matrix was investigated by the scanning electron microscope JEOL JSM-7600F.

The fluorescent properties of the nanocomposite were studied on spectrofluorimeter Cary Eclipse.

The measurements of dielectric permittivity have been carried out by using the immittancemeter MINIPI E7-20.

3. Results and discussion

The crystallographic structure of nanocomposites was examined by diffractometer Rigaku Mini Flex 600s using the X-ray tube with the copper anode (λ=1,5418AºCu-Kα radiation, 30 kV, and mA) at room temperature. Figure 1 shows the diffraction patterns of nanocomposites based on polypropylene and silver sulphide nanoparticles. The phases of nanocomposites were determined by comparing with XRD diffraction patterns those of known minerals.

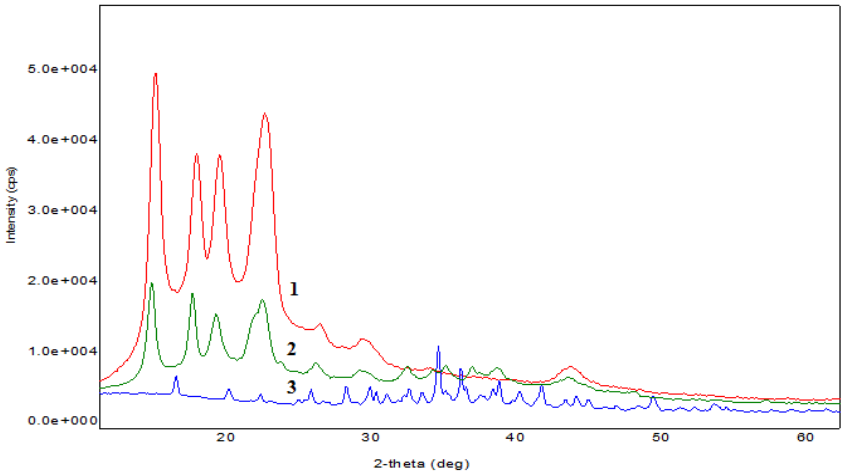

Fig. 1. XRD diffraction patterns of PP powder (1), Ag_2S nanoparticles (3) and nanocomposite based on PP/Ag_2S (2).

The diffraction patterns of pure PP powder are in good agreement with the reported data for ICDD (PDF-2/Release 2011 RDB-00-050-2397). XRD diffraction patterns show that the main peaks of 14,404(100), 17,365(040), 18,888(130), 22,093(111), 25, 76(131), 29,05(141) belong to the α-PP which has monoclinic syngony.

The diffraction patterns for synthesized Ag_2S are in good agreement with the reported data for İCDD (PDF-2/Release 2011 RDB- 00-003-0844). XRD diffraction patterns gave dominant peaks 2θ at 25,18 (11-1); 27,62 (100); 31,78 (11-3); 34,43 (12-1); 38,03(120); 42,99(20-2) and showed the orthorhombic structure of the prepared Ag_2S and are in good agreement with the reported data for Ag_2S (acanthite). The lattice constants for this crystals were a= 6,880 Å, b= 6,920 Å and c=4,770 Å. XRD pattern demonstrates the formation of PP/Ag_2S nanocomposite with characteristic peaks of PP polymer and Ag_2S nanoparticles.

The microstructure and elemental composition of the phases of the PP/Ag_2S nanocomposite were analyzed by SEM (Figure2). The study of the microstructure of the samples is often accompanied by micro X-ray analysis; the characteristic feature of the last one is its locality – the maximum excitation region of 1 μkm. This provides information on the chemical composition of the sample in any selected microscopic site.

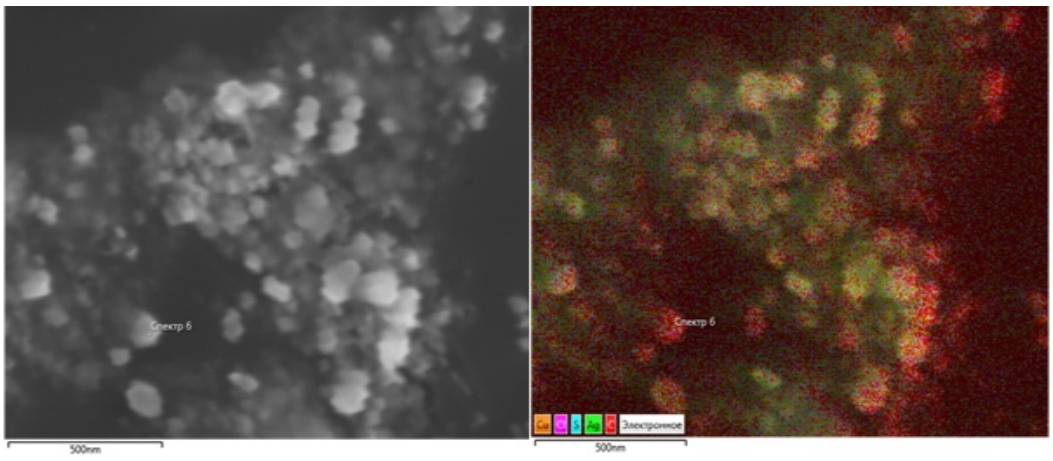

Fig. 2. Energy dispersive micro-X-ray analysis of nanocomposite PP/Ag_2S.

Energy dispersive micro-X-ray analysis of nanocomposite PP/Ag_2S was performed using energy dispersive spectrometer mode using signals of secondary electrons and backscattering electron.

In the case of energy-dispersive spectrometer there is an accumulation of the entire spectrum, so qualitative analysis is automatically performed at any measurement. Energy dispersive spectrometry performs quantitative X-ray microanalysis and spectra obtain predetermined pitch region: point, area, along the line.

To confirm the elemental composition of the phase was carried out mapping of the distribution of elements on the surface (Figure3). If we impose the maps of distribution of the chemical elements (Figure 3) on the microprobe analysis of nanocomposite microstructure (Fig. 2), we find that the light phase consist of three elements C, S, Ag, dark - only from C.

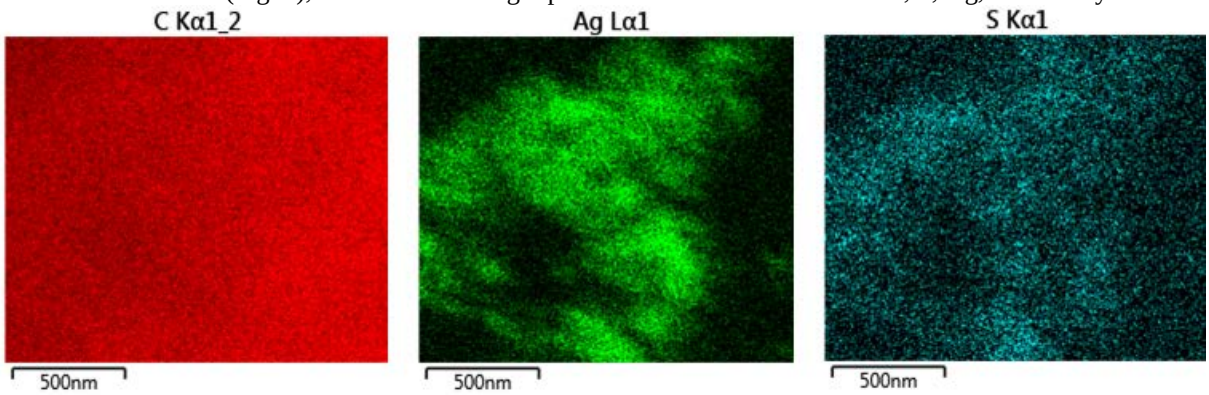

Fig. 3.SEM mapping of nanocomposite sample PP/Ag_2S.

The quantitative elemental composition of the six-point spectra revealed that the light phase is mainly composed of carbon (58 wt.%), oxygen (12wt.%), silver (25 wt.%), sulphide (4wt.%) and the rest - of the other elements.

General view of the X-ray spectrum lines, showing the presence of elements in a dark phase is shown in Figure 4.

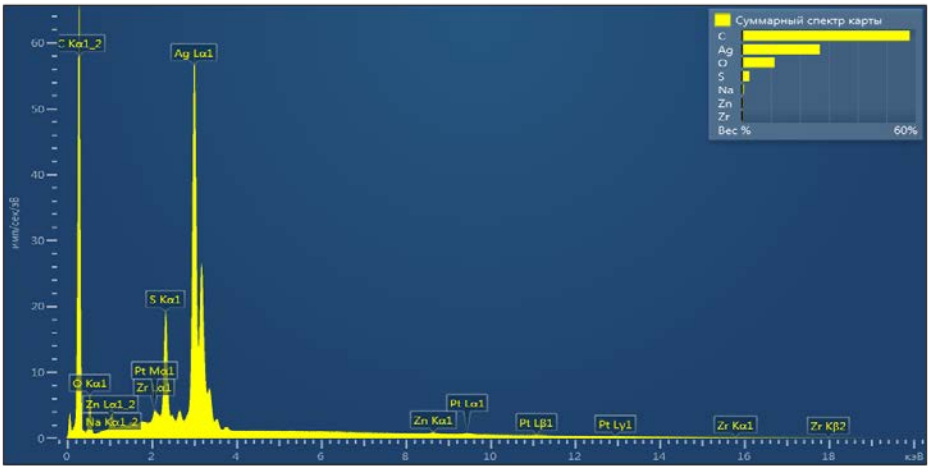

Fig.4.EDS spectrum of PP/Ag_2S nanocomposite

Figure5 shows scanning electron microscope image of PP/Ag_2S nanocomposite obtained with 0,01M contents of silver sulphide nanoparticles.

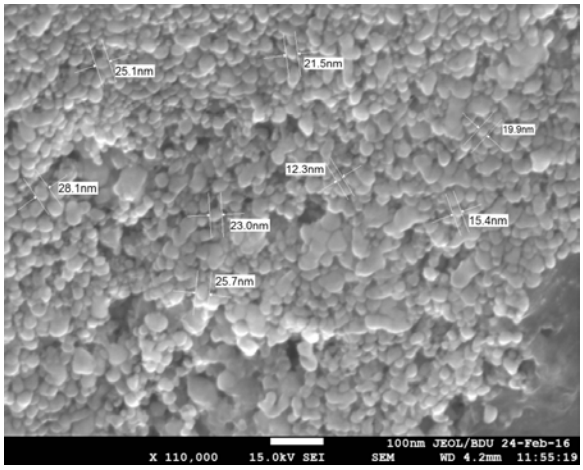

Fig. 5. Nanoparticle size of the nanocomposite PP/Ag_2S.

The figure shows that the size of the Ag_2S nanoparticles is approximately 20-50 nm in polymer matrix. Scanning electron microscopy study also showed that Ag_2S nanoparticles uniformly distributed in the pores of PP polymer.

Also, the influence of corona discharge on the luminescent properties of nanocomposites has been investigated. The luminescence spectra of PP/Ag_2S nanocomposites were studied before and after the polarization under the corona discharge (Figure 6). It was found that the intensity of luminescence increases after polarization.

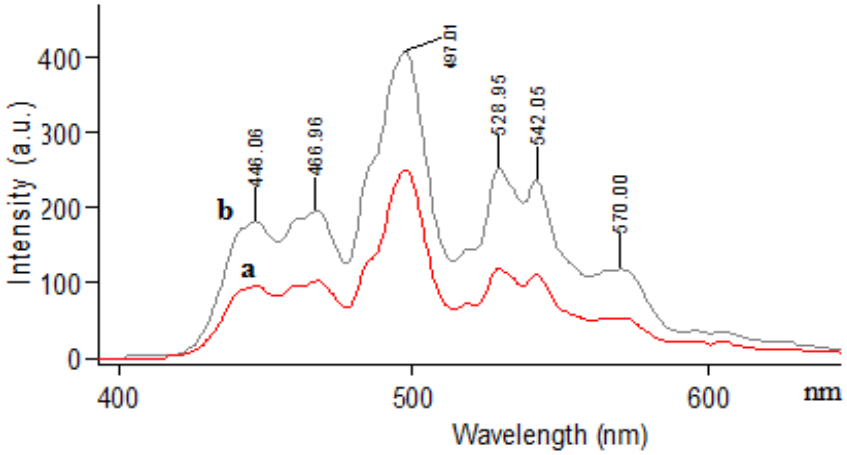

Fig. 6. Luminescence spectra of nanocomposite PP/Ag_2S before (a) and after (b) the polarization under the corona discharge.

The luminescence spectra exhibits peaks at wavelengths of 446 nm, 467 nm, 497 nm, 528 nm, 542 nm and 570 nm. It was found that luminescent peaks at 528 nm, 542 nm and 570 nm were belonging to Ag_2S nanoclusters. As it is seen, the regularities of the change in the luminescence spectra of nanocomposites based on PP/Ag_2S before polarization are the same. After the nanocomposite polarization under the influence of corona discharge, its luminescence spectrum intensity increases strongly.

This means that the value of interfacial interaction of polymer and filler in the material is change. It is assumed that this phenomenon is due to the polarization of newly formed electric charges in the supramolecular structure of nanocomposites as a result of corona discharge. It is considered that during polarization process a large amount of electric charges is accumulated at the interface of the components of the nanocomposite. So the intensity of emission spectrum of nanocomposites increases after polarization due to the activation of luminescent centers by the impact of the newly created local area.

Figure 7 shows the frequency dependences of the dielectric permittivity (ε) of the PP/Ag_2S nanocomposites obtained with 0,01M concentration of silver sulphide nanoparticles. The dielectric permittivity (ε) of PP/Ag_2S nanocomposites was recorded at room temperature and over a frequency range of 10^2-10^6Hs before and after corona discharge polarization.

There are different polarization process under the influence of corona discharge-injection of charged particles to samples and trapping of electrons in a trap, migration polarization, etc.

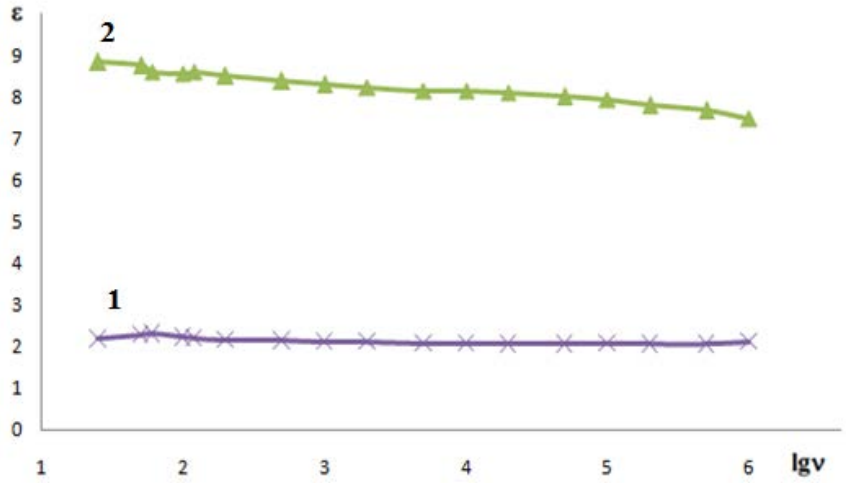

Fig.7. Dependence of the dielectric permittivity of PP/Ag_2S nanocomposites on frequency (1) before and after (2) polarization under the influence of corona discharge.

As can be seen from the graphs, the polarization under corona discharge significantly affects the value of dielectric permittivity of PP/Ag_2S nanocomposite. It was found that the dielectric permittivity of this composite materials increase after polarization process. In general, the increase in the dielectric permittivity of the PP/Ag2S nanocomposites after corona discharge polarization, associated with the emergence of traps for electrical charges. In turn this traps form polarization centers and the dielectric permeability of PP/Ag_2S nanocomposites increases. The decrease in the dielectric permittivity with increasing frequency due to the fact that polar groups can not relax at high frequency and polarization is deteriorating in this region.

4. Results

In this work was used a combination of two synthetic methods for preparation of nanocomposite (PP/Ag_2S) based on polypropylene and silver sulphide by application of ultrasound and microemulsion techniques. The size and the distribution of silver sulphide nanoparticles in the polymer matrix were studied by scanning electron microscope. It was found that depending on the technology for obtaining polymer nanocomposites, uniform and homogeneous distribution of nanoparticles in the polymer matrix can be achieved. It is shown that during polarization under the influence of corona discharge, charges accumulate at the interface of phases of the nanocomposites based on PP/Ag_2S and these charges create a sufficiently large internal local field, and in the field of this charge, the silver sulphide nanoparticle polarizes. Was found that, after polarization under the influence of corona discharge the intensity of the luminescence increases. Has been found that additional luminescent centers are excited in nanocomposites due to boundary charges, and as a result, the intensity of luminescence increases. Also was found that increasing of dielectric permeability of PP/Ag_2S nanocomposites after polarization under the corona discharge and it was explained by formation of traps for electrical. In turn this traps form polarization centers and the dielectric permeability of PP/Ag_2S nanocomposites increases.

References

[1] Ramazanov. M. A, Maharramov. A. M., Nuriyeva. S. Q. Hasanova. U. A, Hajiyeva. F. V. Chalcogenide Letters Vol. 13, No. 7, p. 317 – 324. July (2016)
[2] Ramazanov M.A., Hajiyeva F.V., Maharramov A.M.Influence of corona discharge on the electret and charge states of nanocomposites based on isotactic polypropylene and zirconium dioxide nanoparticles // Ferroelectrics, , v.493, p. 103-109. (2016)
[3] Magerramov A.M., Ramazanov M. A., Hajiyeva F. V. S.Q.Aliyeva. J Nanomedicine and Nanotechnology, v.3, p.5. (2012)
[4] Hamid Reza Ghorbania, MazaherMolaeib. Antibacterial nanocomposite preparation of polypropylene-Silver using Corona discharge, Progress in Organic Coatings 112 (2017) 187–190
[5] Electrical properties of polymers. B.I. Sazhin. Leningrad: Chemistry, 350 p. (1986)
[6] M.A.Bagirov, R.H.Abramov, V.P.Malin, V.A.Oskolonov. The role of gaseous products formed in the electric discharge in the air in the change in the structure and electrical properties of polystyrene. Polymer Science, 16B, No. 8, p.604. (1974)
[7] M.A.Bagirov, N.E.Nuraliyev, M.A.Kurbanov. Journal of Technical Physics, vol. 12 (3), p. 629-634. (1972)
[8] A.M.Maharramov, M.A.Ramazanov, S.G.Nuriyeva, F.V. Hajiyeva, U.A.Hasanova.. Journal of Optoelectronics and Biomedical Materials Vol.7, Issue 2,.p.39-4. April –June (2015)

THE MODIFICATION OF THE STRUCTURAL STATE IN PLASMAMEMBRANE OF YEAST CELLS ON THE γ– IRRADIATION

N.K. KOCHARLI [1], S.T. HUMMATOVA[1],M.A. RAMAZANOV [2], S.G. NURIYEVA[2], I.S. AHMADOV[2]

[1] Department of Biophysics and Molecular Biology, Baku State University, [2] Department of Chemical physics of nanomaterials, Baku State University
ismetahmadov@mail.ru, mamed_r50@mail.ru, sam_bio@mail.ru, aliyeva-s@list.ru

Abstract. By using the method of fluorescent zonde was conducted the estimation of micro viscosities of membranes in yeast cells under the influence of γ-irradiation at dose 5-150 Gy. According to the spectra of pyrene fluorescence has been determined the micro viscosity of lipid bilayer, zones of protein-lipid contacts and in the zone of annular lipids. Based on data, it was shown that, after the irradiation of yeast cells at doses 5-50 Gy there is change of viscosity of adaptive structural-functional rearrangements. The totality of the obtained data suggests that, adaptation processes at high radiation dose (75-100 Gy) in yeast cells, obviously, end at an earlier time.

Key words: *Delayed fluorescence, ionizing radiation, yeast cells, lipid peroxidation*

Introduction

Plasmatic membrane of cell by nature has very sensitive structure against the influence of various external agents, including the radioactive radiation. It was identified that, various doses and irradiation character (chronic or acute) differently change its physical parameters - as micro viscosity and polarity of lipid bilayer [28]. It has been determined, that is caused due to a change in the activity of lipid peroxidation (LPO) processes, by decreasing of total membrane level in phospholipids and cholesterol content, with various quantitative and qualitative changes in the plasmatic membrane structure [12,29]. It can be supposed that, by changing the content, structures, physic -chemical membrane state, one can to a certain extent judge the magnitude and dose nature of obtained cells during irradiation.
Research work by Veselova & Vesolovskii (2012) is shown that determine which processes in air-dry seeds result in bimodal changes of the pea seed quality under the influence of low doses of gamma-radiation. The latter could be the reason for the increased water content in the "improved" seeds and a decreased water permeability of cell membranes [30]. Basing on results, obtained in model membrane systems, it can be supposed that, the development of post-radial changes will happen in erythrocyte membranes of organisms, irradiated in low doses and with low power due to the violation of protein-protein, protein-lipids and lipid-lipid interaction. It is known that, for the evolution of mobility changes in membrane structures of both lipids and proteins, an integrated indexas viscosity can be used [8]. The different ways of the radiation-induced effect were revealed in the investigations of chronic ionizing radiation influence in total doses of 0.3, 0.6 and 1.0 Gy (0.0072 Gy/day) on the structural properties of the apical and of the mitochondrial membranes of small intestine enterocytes. The modification of the physical properties of the membrane surface area, the decrease of the structural order of the lipid component and conformational changes of the proteins were shown to be specific for the apical membrane. The disturbance of the dynamic properties and topography of the internal mitochondria membrane was revealed in the investigation of the inductive-resonance energy transfer between the pairs of the fluorophores: tryptophan-pyrene, tryptophan-ANS, pyrene-ANS [22,23.].

The success, achieved in recent years in membranology allows us to consider the erythrocyte membrane not only as a structural component of the cells-specifically structured shell with regulated physico-chemical properties, but also as a coordinator of the cell's operation, depending on the nature of the incoming information signals of chemical and physical (radiation) nature. The main internal component of erythrocytes is hemoglobin, therefore radiation-induced structural-functional membrane disturbances are capable of reflecting on its characteristics. At the same time, changes in the hemoglobin molecule can affect the characteristics of the membrane by the feedback mechanism. Asrar M. Hawas carried out a large complex of biochemical and biophysical investigations of cells in animal organs (rat), induced to γ-irradiation of low intensity (137 Cs). The rate of alkaline elution of lymphocyte DNA and liver, neutral elution and adsorption on nitrocellulose filters of spleen DNA, structural characteristics (EPR method of spin probes) of nuclear, mitochondrial, synaptic, erythrocyte and leukocyte membranes have been studied [2]. During the investigations of functional cell activities have been studied the activity and isoforms of aldoses' and lacto dehydrogenase enzymes, activities of acetyl cholinesterase, superoxide dismutase, glutathione peroxidase, the formation rate of superoxide anion- radicals, composition and antioxidant activity of lipids listed above membranes, and also the sensitivity of cells, membrane, DNA, organism against the influence of additional injuring factors [9, 13, 24, 27]. In all studied indicators was found their bimodal dependence on doses, namely the effect increased at low doses, reaching a maximum (low-dose), then decreased (in some cases the sign of the effect was reversed) and further by growing dose again increased. The magnitude of the low-dose maximum of the effect and the dose, which it achieved, depends on the nature of bio object and dose rate [3, 20].

Differing from the structural characteristics of DNA (adsorption), the micro viscosity of both membrane phases on nitrocellulose filters significantly differs from the control at6-9,6sGy dose interval. Attention is drawn to the comparable scale of synchronous structural shifts, occurring in DNA and membranes under the influence of such low dose intensity irradiation. For the evolution of functional cell activity we used the data of kinetic parameters of membrane and cytosolic enzymes in cells of irradiated animals. The changes of these parameters were already observed at 1,2-2,4 s Gy. An important result of the studies was the establishment of a change in sensitivity of a separate macromolecule, cell and organism against the additional influence of injuring factors of the same and different natures. The explanations offered by the authors about the nature of the nonlinear bimodal effect dependence on doses are based on the representations, that there are gaps among the doses, causing damage in bio objects and initiating systems of their restoration [11].

Thereby, while the recovery (or adaptation) system doesn't work with whole intensity, the bio effect increases by increasing doses, and then has been as the intensity recovery processes or remains at the same level, or decreases till elimination, or can change its sign and again increases by increasing doses, while the damage in bio objects prevails over the restoration. All those data indicate that, there action of organism on the effect of low radiation doses has dose function, irradiation power and time elapsed since the beginning of irradiation [14].

So, for the influence of physical factors, namely low intensive ionizing irradiation is characterized with the same patterns, as in the USD case of the biological active substances: nonlinear, non-monotonic, bimodal effect dependence on doses, presence of "a dead-zone", the change of sensitivity against endogenous and exogenous factors, reverse dependence on the irradiation intensity. Close regularities were also obtained for non -ionizing radiation [25].

In radiobiological literature sometimes is found the determination of low dose radiations dose, beginning with which the sign of the effect changes e.g. the transition from inhibition of cellular growth to stimulation [21].

By recent investigations uniquely are proven that, the irradiation by low doses causes numerous structural rearrangements in cells, persisting long after the irradiation and leading to the change of functional cell activity. The aim of the present study was to examine of gamma radiation on bactericidal effect of levofloxacin [26]. All living organisms are exposed to different types of irradiation and therefore, the impact investigation of these radiations on the living organisms is of great interest. An essential role in the regulation of processes, occurring in membranes, is their micro viscosity of complex index, which reflects both structural, and functional (diffusion) aspects of lipid constituent membranes. The change of micro viscosity in membranes closely connected with the metabolic changes, occurring in cells [5,6, 16,18].

Materials and Methods

As the investigation object served yeast cells of *Candida* guilliermondii-916. Yeast cells were grown in the wort-agar in thermostat at 28^0C. The experiments were carried out with the suspension of 2-days culture (1×10^8cell/ml). The irradiation of yeast cells was carried out by $\gamma-$ gamma-quanta at a ^{60}Co setting. Irradiation doses are 5Gy-100Gy. As a control served non-irradiated suspension. For the estimation of structural state of membrane was determined the micro viscosity of lipid phase. The determination method based on the ability of a fluorescent pyrene probe to formexcimers in a nonpolar medium. The speed of lateral diffusion and pyrene excimerization in the lipid layer of membranes are inversely proportional to the viscosity of the medium. 1 ml suspension, aligned with the protein content, was placed on a magnetic stirrer and 10^{-3}M pyrene solution was added in ethanol: 0,001ml in cell suspension. In a minute (time of wholly solution pyrene excimerization in lipid phase of membrane)was measured the fluorescence of samples on a spectrophotometer-Varian Cary Eclipse 2007 at a maximum wave 334 nm excitation light for the evaluation of micro viscosity of lipid bilayer. The peak of fluorescence excime pyrene $F_Э$ was registered at an emission wavelength 470 nm, but the peak of fluorescence monomer F_m at an emission wavelength of 393 nm.

The pyrene excimerization coefficient Fe / Fm (334) reflecting the micro viscosity of lipid bilayer, expressed by the ratio of the maximum fluorescence value of pyrene excimers Fe (in relative fluorescence units at $\lambda_{emission}$= 470 nm) to the maximum of the fluorescence of monomers pyrene $F_м\lambda_{emission}$=393nm) at excitation λ 334 nm. The ratio of fluorescence intensity of excimers to monomers F_e/F_m is inversely proportional to the micro viscosity of lipid bilayer and is directly proportional to its fluidity. The determination of the polarity of the lipid phase and the zones of protein-lipid contacts of yeast cell membranes. The cell suspension containing 1mm ethanol pyrene solution (7 μmol/ml cell suspension) was fluorimetricated at an excitation light wavelength of 334 nm and at the emission wavelength 372 and 393 nm. The polarity of the membrane phase of membranes (F_{372} / F_{393} (334 nm)) was evaluated with respect to the fluorescence intensity of two monomeric forms of F_m pyrene at the excitation wavelength 334 nm and at the emission wavelength 372 and 393 nm. The polarity of the protein-lipid contact zones (F_{372} / F_{393} (282nm) was evaluated with respect to the fluorescence intensity of two monomeric forms of F_m in the thin pyrene spectrum at the excitation wavelength of 282 nm and at the emission wavelength 372nm and 393 nm [4,15].

At present work has been studied the influence of γ-irradiation on the development of LPO processes in *Candida guilliermondii* cells.The rate of peroxide photooxidation of lipids in membranes was judged by the accumulation of one of the oxidation products of malonic dialdehyde (MDA), the concentration which was determined by means of thiobarbituric acid (TBC "Siqma"), measuring the density of the MDA-TBA complex at the maximum of its absorption spectrum at 532 nm (ε =1,56·$10^5$$M^{-1}$$sm^{-1}$) [1,7]. The registration of the absorption spectra was conducted on a SF-46 spectrophotometer.

The wheat germ oil was used at a concentration of 20 ml per 10^8 cell / ml. The statistical results were processed using the t-test of the student.

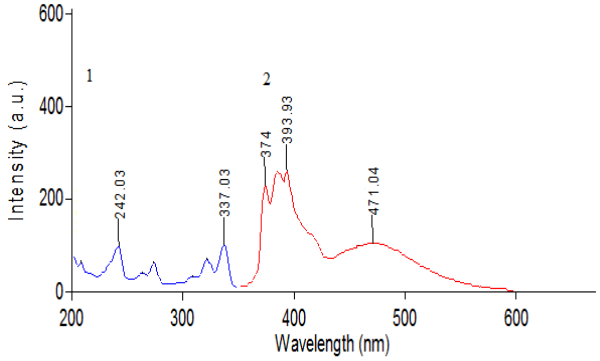

Fig 1.The excitement and radiation spectrums of pyrene zonde in yeast cells.

Results and discussion

The pyrene molecule moves to a state of excitement while absorbing light photon. This molecule can radiate photon at 390 nm wavelength and create an excimer combining other unexcited molecule itself. The excimer of pyrene radiates the photon at 470 nm wavelength. So, in the measurement of excimer formation its luminescence based on the wavelength difference of monomer's luminescence.

In figure 1, have been shown the excitement and radiation spectrums of control samples. At this time the wavelength of excitement was selected λ = 337 nm. The radiation wavelength was noted λ =470 nm while scanning the excitement spectrum. 470 nm wavelength corresponds to the fluorescence of the pyrene probe exymer. The pyrene's 393 nm wavelength emission corresponds to its monomer form. Similarly the radiation was scanned for the samples radiated at various doses (5-150 Gy). Depending on the impact doses of qamma rays on cells basing on the indications in those spectrums has been identified the ratio of fluorescence of the monomeric form to the fluorescence of the pyrene's exymer form. The results of investigations and discussions ofγ-irradiation in yeast cells at 5-50 Gy. Doses judging by the excimerization coefficient, led to an increase in micro viscosity (decrease of fluidity) of a common lipid bilayer membrane. Similar processes were also observed in the areas of annular (with whites) lipids (fig.2). After the irradiation at doses 50-150Gy. was observed the minor change in parameters, characterizing the physical state of the lipid bilayer and annular lipids of yeast cell membranes.

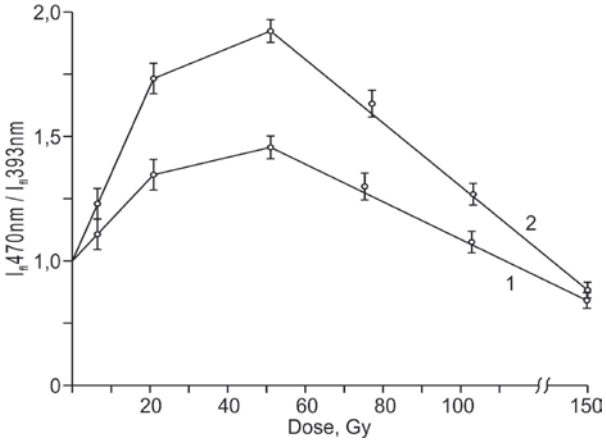

Fig.2. *Dose dependence of membrane microviscosity in yeast cells C. guilliermondii on γ-irradiation, measured with respect to the fluorescence intensity of the excimers and monomers of the pyrene probe (I_{fl}470nm / I_{fl}393nm). 1) λexci. 334 nm, 2) λexci. 282nm*

Data, obtained using a fluorescent pyrene probe indicate the changes in the studied parameters of the structural state of cell membranes. Based on the changed data in micro viscosity of yeast membranes after irradiation can be supposed, that the modification of the structure can lead to a change in the polarity of lipid bilayer permeability.

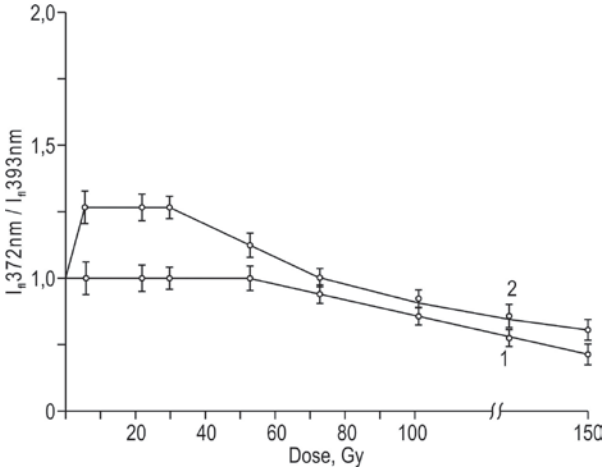

Fig.3.*Dose dependence of environmental polarity of pyrene probeon the lipid layer of membranesF_{372}/F_{393} and on the areas of annular lipids during γ-irradiation. 1) λexci. 282 nm. 2) λexci. 334 nm.*

The polarity of the environment of pyrene probe in the lipid layer of membranesF_{272}/F_{393}(334)increases while irradiating cells at doses of 5Gy-50Gy. While evaluating the polarity of the total membrane lipid bilayer, was determined that, during the irradiation at doses 75-150Gy. a slight increase has been observed in polarity of the lipid component of cell membranes (Fig. 3). The polarity of the environment of the pyrene probe in the area of annular lipids F_{272} / F_{393} (282) does not have significant differences from control at radiation doses of cells from 5 to 50Gy.The polarity dynamics of pyrene microenvironment in the membranes of yeast cells has only the decrease tendency in the areas of annular lipids after irradiation under doses of 75-150Gy (Fig. 4). In the lipid layer of membranes and in the zone of protein-lipid contacts, the polarity slightly increases, which agrees with the data on the accumulation of primary LPO products in cell membranes, rapidly metabolizing into hydrophilic hydro peroxides of fatty acids.

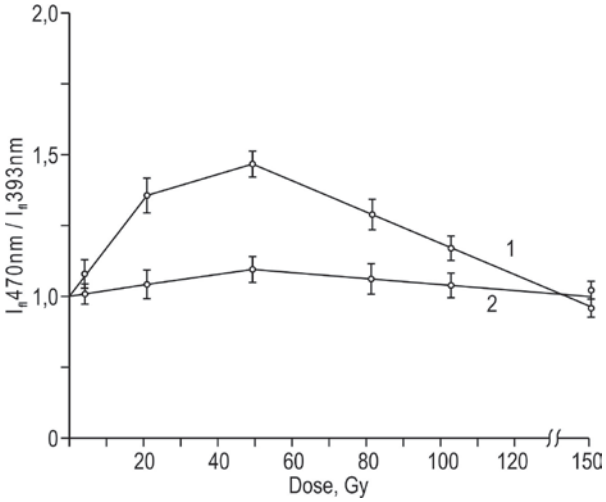

Fig.4. *Dose dependence of membrane micro viscosity in yeast cells C.guilliermondii onγ-irradiance measurability with respect to the fluorescence intensity of the excimers and monomers of pyrene probe (I_{fl}470 nm / I_{fl} 393 nm) λ ex. 282nm.*

The consequences of damage on membrane components caused byγ- irradiation are quite significant, which nowadays cause the necessity of much deeper investigation of γ-irradiation influence against LPO biomembrane processes.

Namely on the yeast cell level the issues related to the regulation of LPO, which is the least studied in comparison with other organisms, at that time as cellular regulating mechanisms in microorganisms play significantly greater role and are manifested than other biological system. The specific character of the LPO study is determined by that, compared from other intercellular system LPO processes is by itself, and components are very stable, and their violations connected with the changes of concentration connections regulating speed of these reactions in cells. In figure 3 was shown the dependence of MDA quantity formed in yeast cells on a dose γ-irradiation.

As seen in the figure by increasing γ-irradiation doses (5-150Gy) in cell membranes, the increase of MDA concentration occurs, which indicates the development of the LPO process. MDA concentration was the highest during cell irradiation at 75Gy. Dose which exceeded the control values 2 times. After γ-cell irradiation at 100-150 Gy doses MDA quantity is decreased to the control level and below (Fig. 5). During LPO stimulation in membranes the content of lipids decreased, and also changed the micro viscosity and electrostatic charge. During deeper oxidation of phospholipids,

the structure of lipid bilayer violate sand occurs in defective areas of cell membranes, and violates the functional activity [17].

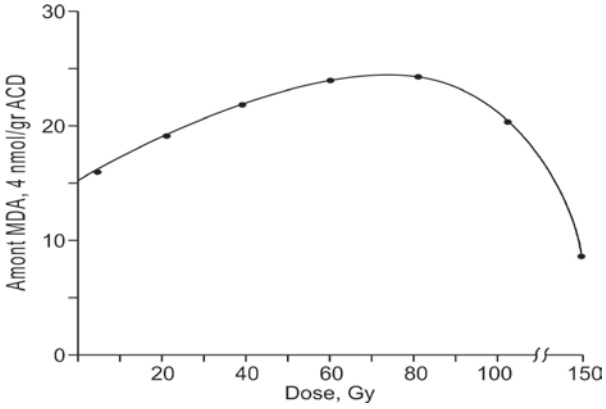

Fig.5. *The dependence of MDA amount formed in yeast cells on the dose of γ-irradiation. ASD-absolutely dry yeast.*

It is known that, the change in viscosity characteristics is a reflection of various modifications of intermolecular bonds, which is in fact determined by a combination of levels of mobile and stable interactions of membrane components, which follows from the notions of membrane structure, based on two hypothetical models :liquid-mosaic and solid-frame [10]. In one of them emphasizes the dynamic aspects of membrane organization, in another -the stability of its components and intermolecular bonds come to the fore. The importance of maintaining the relative stability of membrane structure is determined by the need to preserve those specific membrane functions, which caused by their tissue accessories, cellular specialization. Relative stability is associated with bilayer redness of lipid organization of membranes, the existing characteristics for each type of membrane of a chemical composition, with preservation of asymmetry in the distribution of proteins and lipids in internal and surface layers, the creation of aggregates of lipids with proteins, lipids with lipids, lipid rafts and protein complexes within the layer [19].

Thus, it can be supposed that, during the irradiation of yeast cells at doses 75-100Gy. The viscosity characteristics of membranes is slightly different from the control, which indicates the establishment of relative stability of the structure and function of membranes. After 5-50Gy. Irradiation doses the change in viscosity characteristics and the decrease of the lipid component fluidity are the reflections of adaptation structurally functional rearrangements. Basing on obtained data on the peculiarities of the influence of wheat germ oil duringγ-radiation the membrane modification in cells which induced to low doses is reversible and doesn't have difference from control as lipid bilayer and lipid phase in protein areas of membranes in yeast cells. So, afterγ-radiation influence at 5-50Gy. Doses the similar effects were noted during the irradiation in the presence of wheat germ oil, the viscosity of lipid bilayer and protein-lipid membrane contacts in yeast cells are in norm. The obtained data testify the radio protective impact of wheat germ oil. A deeper study of the effect of this oil is the object of further investigations by γ-radiation (^{60} Co).The totality of the obtained data suggests that, the adaptation processes at greater irradiation doses the yeast cells obviously are completed at an earlier time.

References

[1] Alam Zeb * and Fareed Ullah. A. J Anal Methods Chem. 2016: 9412767. (2016)
[2] Asrar M.Hawas. Journal of Radiation Research and Applied Sciences, Volume 6, Issue 2, , Pages 38-44 October (2013)
[3] Azzam EI, Jay-Gerin JP, PainD. *Cancer Lett*;327:48–60.(2012)
[4] Angelo Azzi . Quartaly Reviews of Biophysics. Volume 8, Issue 2, , pp. 237-316 .May (1975)
[5] Cook L. R., Stohs S. J., Angle C. R., Hickman T. I. and Maxell R. C.. British Journal of Industrial Medicine. Vol. 44, No. pp. 841-84, 12 Dec., (1987)
[6] Devynck MA J Kunes Kennek le Josef Zicha. 94(1):79-85 · January (1998)
[7] H.H.Draper, E.J.Squires, H.Mahmoodi,J.Wu, S.Agarwal, M.Hadley. Free Radical Biology and Medicine. Volume 15, Issue 4, Pages 353-363. October (1993)
[8] L.Kh Eidus. Biological Action of Low Doses of Radiation: A Novel View on the Problem.Nova Science Pub., 2001, pp. 80
[9] Adam W.Smith. Biochimica et Biophysica Acta (BBA) - Biomembranes. Volume 1818, Issue 2, Pages 172-177. February (2012)
[10] Fatmah M.Alshammari, Sonia M.Reda, Magdy M.Ghannam. Potential effects of gamma irradiation on the stability and therapeutic activity of anticancer drug, doxorubicin. Journal of Radiation Research and Applied Sciences, Volume 10, Issue 2, Pages 103-109. April (2017)
[11] Garth L.Nicolson. Biochimica et Biophysica Acta (BBA) - Biomembranes, Volume 1838, Issue 6, Pages 1451-1466. June (2014)

[12] Gerald Kendall, Pavel Chernyavskiy, J Don Appleton, Mark P Little. Modelling the bimodal distribution of indoor gamma-ray dose-rates in Great Britain. *in* Radiation and Environmental Biophysics · August 2018
[13] Giuseppina Barrera .Oxidative Stress and Lipid Peroxidation Products in Cancer Progression and Therapy. ISRN Oncol. 2012; 2012: 137289. Published online. Oct 17. (2012)
[14] M. Heidarieh, A.Borzouei, S. Rajabifar, F. Ziaie , Sh. Shafiei. Iran. J. Radiat. Res., 9(4): 245-249. (2012)
[15] Hurem S, Martín LM, Brede DA, Skjerve E[1], Nourizadeh-Lillabadi R, Lind OC, Christensen T, Berg V, Teien HC, Salbu B, Oughton DH, Aleström P, Lyche JL. Dose-dependent effects of gamma radiation on the early zebrafish development and gene expression. PLoS One. Jun 19 (2017)
[16] Ivan A. Boldyrev, Xiuhong Zhai, Maureen M. Momsen, Howard L. Brockman, Rhoderick E. Brown and Julian G. Molotkovsky. New BODIPY lipid probes for fluorescence studies of membranes. J Lipid Res.; 48(7): 1518–1532. Jul (2007)
[17] Jaiswal RK, Rama Sastry BV, Landon EJ. Changes in microsomal membrane microviscosity and phospholipid methyltransferases during rat liver regeneration. Pharmacology. 1982;24(6):355-65.
[18] Jeffrey M. Grim, Molly C. Semones, Donald E. Kuhn, Tamas Kriska, Agnes Keszler, and Elizabeth L. Crockett. Am J Physiol Regul Integr Comp Physiol.; 308(5): R439–R448. Mar 1 (2015)
[19] Josef Zicha, Jaroslav Kunes, and Marie-Aude Devynck. AJH;12:315–331. (1999)
[20] Kai Simons and Julio L. Sampaio.Membrane Organization and Lipid Rafts. Cold Spring Harb Perspect Biol. Oct; 3(10), (2011)
[21] Kasumi Kawamura, Fei Qi, Junya Kobayashi. Journal of Radiation Research., Volume 59, Issue suppl_2, 1, Pages 91. April (2018)
[22] Kaushala Prasad Mishra. Dilemma of low-dose radiation effects: Extensive research needed. EDITORIAL, , V.7, Is.1 p. 1. (2016)
[23] Khizhniak SV , Bublik AA , Kisil' EA, Voĭtsitskiĭ VM , Kucherenko NE. Effect ionizing irradiation on the structural and functional properties of the basolateral membrane of small intestine enterosytes. Radiatsionnaia biologiia, radioecologiia / Rossiĭskaia akademiia nauk, 39(6) pg 644-7., Nov-Dec (1999)
[24] Khizhniak S.V, Kisil E.A, Laposha E.A, Kudriavtseva A.G, Voĭtsitskiĭ V.M.. Radiats Biol Radioecol. 46(1), p.27-33. Jan-Feb, (2006)
[25] G. J. Köteles. Radiation and Environmental Biophysics March Volume 21, Issue 1, pp 1–18. (1982)
[26] Pelevina II, Aleshchenko AV, Antoshchina MM, Birjukov VA, Reva EV, Minaeva NG.Article in Russian Radiats Biol Radioecol. ;55(1):57-62. Jan-Feb, (2015)
[27] Raza S, Iqbal Y, Ullah I, Mubarak M.S, Hameed M.U, Raza M. Effects of gamma irradiation on the physico-chemical and biological properties of levofloxacin. Pak J Pharm Sci. ;31(1):181-186. Jan (2018)
[28] Sima Shahabi, Farhood Najafi, Abbas Majdabadi, Tabassom Hooshmand, Masoumeh Haghbin Nazarpak, Batool Karimi, and Seyyed Mostafa Fatemi. Effect of Gamma Irradiation on Structural and Biological Properties of a PLGA-PEG-Hydroxyapatite Composite. Scientific World Journal. 2014; (2014)
[29] Stark G. Biochimica et Biophysica Acta, 1071 103-122. (1991)
[30] Shadyro OI, Yurkova IL, Kisel MA. Radiation-induced peroxidation and fragmentation of lipids in a model membrane. Int J Radiat Biol. Mar 2002
[31] Veselova T.V, Veselovskii V.A. **Article** *in* Radiatsionnaia biologiia, radioecologiia / Rossiĭskaia akademiia nauk 52(4):428-30 **.** October (2012)